INFORMATION TO USERS

This manuscript has been reproduced from the microfilm master. UMI films the text directly from the original or copy submitted. Thus, some thesis and dissertation copies are in typewriter face, while others may be from any type of computer printer.

The quality of this reproduction is dependent upon the quality of the copy submitted. Broken or indistinct print, colored or poor quality illustrations and photographs, print bleedthrough, substandard margins, and improper alignment can adversely affect reproduction.

In the unlikely event that the author did not send UMI a complete manuscript and there are missing pages, these will be noted. Also, if unauthorized copyright material had to be removed, a note will indicate the deletion.

Oversize materials (e.g., maps, drawings, charts) are reproduced by sectioning the original, beginning at the upper left-hand corner and continuing from left to right in equal sections with small overlaps.

Photographs included in the original manuscript have been reproduced xerographically in this copy. Higher quality 6" x 9" black and white photographic prints are available for any photographs or illustrations appearing in this copy for an additional charge. Contact UMI directly to order.

Bell & Howell Information and Learning
300 North Zeeb Road, Ann Arbor, MI 48106-1346 USA
800-521-0600

Buffer Gas Cooling of Ions in a Radio Frequency Quadrupole Ion Guide:

A study of the cooling process and cooled beam properties

By

Taeman Kim

Department of Physics, McGill University

Montreal, Canada

August 1997

A thesis submitted to
the Faculty of Graduate Studies and Research
in partial fulfillment of the requirements for the degree of
Doctor of Philosophy

To My Parents and Wife

for Their Love and Patience

Contents

0.1 Abstract xiv

0.2 Résumé xv

0.3 Acknowledgement xvi

1 Introduction **1**

1.1 Ion trapping and cooling 2

1.1.1 Description of ion traps and their use 2

1.1.2 Ion cooling and its benefits 5

1.1.3 Ion phase space distribution and temperature 6

1.2 This study 8

1.2.1 The physics of buffer gas ion cooling 9

1.2.2 Application of the results 12

1.3 Contributions of this thesis 14

2 Theory of Trapping and Cooling **18**

2.1 Principles of ion trapping 19

2.2 The quadrupole mass filter — an ion trap 20

2.3 Introduction to phase space dynamics 29

2.3.1 Phase space properties of the ion motion 30

2.3.2 Emittance and acceptance 35

2.3.3 Time evolution of some simple ion collections 36
2.4 Phase space dynamics and cooling 44
2.4.1 Collisional cooling 44
2.4.2 Evaporative cooling 45
2.4.3 rf heating 45

3 The Phase Space Distribution and Temperature of Ions in a RF Quadrupole Field 48

3.1 Introduction 49
3.2 Temperature and phase space 51
3.2.1 The ellipse for simple harmonic motion 52
3.2.2 The action for rf motion 53
3.2.3 Action diagram for combined SHM and RF motions 55
3.3 The ion distribution at thermal equilibrium in an rf quadrupole field . 61
3.3.1 Ion distribution in simple harmonic motion 61
3.3.2 σ_x and σ_{v_x} as functions of the rf phase 65
3.4 Comparison with other temperature definitions 68
3.5 Testing the assumptions of the definition of T_{SHM}^{mod} 71

4 Experimental System 76

4.1 Design of the experimental setup 78
4.2 Optimal pressure - Mobility calculations 79
4.2.1 Definition of the mobility 81
4.2.2 The axial velocity and energy decay time constant 82
4.2.3 Macro-motion amplitude decay time constant 83
4.2.4 The macro-motion amplitude damping constant for under damping 84

4.2.5 A practical method to determine the optimal buffer gas pressure 85
4.3 Vacuum system 86
4.4 The ion source 87
4.4.1 The Beam Purity 90
4.4.2 The Current Stability 91
4.5 The Collisional Cell 91
4.6 Detector 94
4.6.1 Miniature quadrupole beam guide 96
4.6.2 Beam profiler 98
4.7 Simulation of the ion beam extraction from the quadrupole rods . . . 100
4.7.1 RF fringing field and DC extraction field implementation . . . 105
4.7.2 Ion beam envelope evolution in the extraction fields 107
4.8 Spatial Distribution of the ion beam 107

5 Simulations **110**

5.1 Trajectory calculation using a drag force model 111
5.2 The Monte Carlo simulation 112
5.2.1 The ion-neutral interaction potential models used in the Monte Carlo simulation 112
5.2.2 Implementation of the collisions 116

6 Results and Discussion **124**

6.1 Simulation of the cooling process 124
6.1.1 Trajectory calculations using mobility 124
6.1.2 Effect of buffer gas collisions in phase space 126
6.1.3 The cooling process 128
6.1.4 Interaction potential effect in the MC simulation 133

6.2 Beam profiles and temperatures in the equilibrium state 134
6.2.1 Temperature of the Simulated ion beam 137
6.2.2 Measured temperature of the cooled beam 140
6.2.3 Rescaling the temperature 143
6.2.4 Dependence of the temperature on the current 146
6.2.5 The effect of the axial field 146
6.2.6 q value dependence of the temperature 148
6.2.7 Discussion of the temperature measurements 149
6.3 Transmission 150
6.3.1 Pressure dependence of the transmission 152
6.3.2 q value dependence of the transmission 154
6.3.3 The axial field effect on the ion transmission 155
6.3.4 Optimal pressure by mobility calculation 158
6.3.5 The stable q value expansion 158
6.3.6 Dependence of transmission on the injection energy (with miniature quadrupole exit) 159
6.4 Kinetic energy of the exiting ions 160
6.5 Drift time (cooling time) 164
6.6 The emittance of the exiting ion beam 166

7 Conclusion **169**

List of Figures

1.1 (a) The quadrupole ion guide; (b) the Paul trap. 3

1.2 Schematic phase space diagram of the cooling process. 10

1.3 The model of thermal equilibrium in buffer gas cooling ion beam guide. 10

1.4 Schematics of (a) Atmospheric Pressure Ion(API) source mass spectrometer and of (b) Nuclear mass measurement system. *: related with this study. 13

2.1 (a) The electrode configuration and (b) the potential distribution of an quadrupole mass filter with circular electrodes. 23

2.2 The stability diagram for the mass filter. 24

2.3 Ion trajectories for several points in the stability diagram. 26

2.4 The trajectory and well model approximation for a=0, q=0.1. 30

2.5 Phase space evolution of the boundary C_1 into the boundary C_2 over the time interval between t_1 and t_2. 31

2.6 An ellipse with its critical values. 34

2.7 Emittance and acceptance diagram. 35

2.8 The evolution of phase space diagram for zero electric field region. . . 37

2.9 The evolution of a phase space diagram for a uniform electric field. . 38

2.10 The evolution of phase space diagram for an electric field which is proportional to the displacement from the origin of the coordinate system. 40

2.11 The periodic potential in a quadrupole mass filter can be approximated by piecewise constant approximation - for a short interval the potential can be considered as constant. 41

2.12 The action diagram in a quadrupole beam guide for for several rf phases. Zero phase is defined as the instant that the electric potential on the x rods is a positive maximum for positive ions. 43

3.1 (a) The phase space diagram for simple harmonic motion with an arbitrary scaling of x and p_x and (b) with the scale in which the ellipse becomes a circle. The advantage of such a scaling is that in such a diagram the points representing the particles all rotate at the same uniform angular velocity; that of the simple harmonic oscillation itself. 52

3.2 Phase space diagram for the rf motion in a quadrupole mass filter. The amplitude of the oscillation is proportional to the displacement of the ion from the central axis of the mass filter. The phase of the rf displacement is 180 degree relative to the rf phase. 54

3.3 Points obtained by calculating the momentum-displacement coordinates for an ion in a quadrupole beam guide for a particular operating parameter q and plotting the results at the instants of 270 degree rf phase. The ion started at a positive displacement in x with zero momentum (point zero). The subsequent points are labeled 1 to 8. The simple harmonic oscillation is seen to take approximately 7.8 rf cycles. 57

3.4 The rf distorted ellipse and and its associated SHM ellipse with their critical values. 58

3.5 The equi-density ellipses (1σ) of simple harmonic potential with rf distorted ellipses at 0, 90, 180 and 270 rf phase angles for various q. The drawings with different q values are for a temperature of 0.025 eV. 62

3.6 The distribution of particles in a simple harmonic potential in thermal equilibrium at temperature T. 65
3.7 The sigma x as function of rf phase for various q. 66
3.8 The sigma p as function of rf phase for various q. 67
3.9 The differently defined temperatures vs q for a temperature 1 in T_{SHM}^{mod}. 71
3.10 The phase space evolution of a simulated ion beam. Cesium ion beam reached thermal equilibrium by nitrogen molecular collisions in an axial field quadrupole at $\Omega/2\pi$ =700 kHz, q=0.4 and 8 Pa buffer gas pressure. 73
3.11 The spatial and momentum distributions at a specific rf phase (0 degree) with a Gaussian with same standard deviation. 74
3.12 The standard deviations x and p of simulated beams in a thermal equilibrium as functions of rf phase (empty circle:1.3 Pa, filled circle: 8 Pa, solid line: prediction by the assumption). 75

4.1 The schematics of the experimental setup. 77
4.2 A graphical method to determine the optimal buffer gas pressure for cesium ions in nitrogen buffer gas. The hatched region shows a sufficient pressure range for buffer gas cooling. 85
4.3 Cross-sectional diagram of the surface ionization ion sourc. 88
4.4 The mass spectrum of the ion source. The higher value of U/V corresponds to the higher resolutio. 90
4.5 The axial field radio frequency quadrupole (AXF_RFQ) ion beam guide and its driving circuit. 92
4.6 The contour plot of the DC potential in x-z plane. 93
4.7 The miniature quadrupole ion beam guide ($r_o^{'}$ = 1.75 mm, L = 40 mm) interfaces the collisional cell and the high vacuum chamber. It extends the quadrupole field to the high vacuum chamber. 97

4.8 Detector assembly consisting of a miniature quadrupole ion beam guide and a rotating beam profiler. 99

4.9 A typical result of the RFQ_EXT simulation. Each trajectory represents the evolution of the maximum position of the ellipse for each phase, starting within the full quadrupole field. The hatched objects represent one rod and the detector. 103

4.10 Outline of the determination of temperature. 104

4.11 The electric fields implemented in the simulation of the ion beam extraction from the quadrupole rods (RFQ_EXT): (a) the rf fringing field and (b) the axial potential and its derivative. The hatched objects represent the position of the electrodes. 106

4.12 (a) The spatial distribution of the ion beam for a few specific rf phases, (b) the time averaged distribution , and (c) the x or y axial distribution in differential form and (d) in integral form 108

5.1 The interaction potentials and the scattering angles as functions of the impact parameter. 117

5.2 The calculated mobilities with the realistic potential model and the experimentally determined data. 120

5.3 The pressure and electric potential implementation in the Monte Carlo simulation. 122

6.1 The calculated trajectories of cesium ions in nitrogen buffer gas using mobility. The operation condition was f = 0.7 MHz V=300 V. 125

6.2 The amplitude decay time constant of the macro-motion as a function of the pressure. 127

6.3 The effect of buffer gas collissions in phase space. (a) at ideal vacuum, and (b) at 8 Pa nitrogen buffer gas pressure. The ellipses represent the acceptance of the ion guide. White: originally outside the acceptance, black: originally inside the acceptance. 129
6.4 The evolution of the ion beam in the AXF_RFQ. 131
6.5 The evolution of the ion beam in the AXF_RFQ. 132
6.6 Trajectories calculated by the MC simulations (a) with the real potential model and (b) with the hard sphere model. 135
6.7 The axial energy vs cooling time for the MC simulation (a) with the RP model and (b) with the HS model. 136
6.8 A MC simulated distribution in the miniature quadrupole and temperature fitted curves by least square fitting program (Temp-Fit) with two extra curves at different temperatures to give an idea of the sensitivity of the measurement. The operating conditions are 0.7 MHz rf frequency and q=0.47. The figure shows that the beam size is about 2 mm in diameter. 138
6.9 The temperature of the ion beam (from the MC simulation). The temperature from the distribution at the detector was calculated from the sigmas at the detector using RFQ_EXT. 139
6.10 Typical experimental data at the detector and their corresponding temperature fit for cesium ions at 700 kHz, 300V rf amplitude, 25 V extraction potential and 8 Pa nitrogen pressure. 141
6.11 kT as a function of I for various extraction potential. The functions were assumed to be linear and were extrapolated to zero current. . . . 142
6.12 Comparison of the temperatures from the experiment and from the MC simulation. 144
6.13 The corrected temperature from the MC simulation and the experiment. 145

6.14 The beam size of experimental and MC simulation data. 146
6.15 The beam temperature dependence on the axial field. The result of the MC simulation for the AXF_RFQ operating at .7 MHz, q=0.47 and 8 Pa nitrogen buffer gas pressure. 147
6.16 The rf amplitude (q value) dependence of temperature. 148
6.17 The skimmer type lens and the rf field attenuation near the lens. . . . 152
6.18 The experimental ion transmission for different nitrogen buffer gas pressures with $f = 250\ kHz$. 153
6.19 The acceptance ellipse of the AXF_RFQ for various values of q. The area is proportional to the acceptance. 156
6.20 Acceptance as a function of q. 157
6.21 The stable maximum q value as function of pressure. 159
6.22 The transmission as a function of the rf amplitude for various injection energies ($f = 0.7\ MHz$, 8 Pa nitrogen buffer gas). 161
6.23 Transmission as a function of the injection energy for various q values. 162
6.24 The Ion current vs retarding potential and the the energy spread (FWHM). 163
6.25 The drift time (cooling time) of the ions in the AXF_RFQ for various currents and axial fields. 165
6.26 Drift time found using the MC simulation is compared with the experimental data. 167

List of Tables

3.1 The temperature definitions for the ions in a trap. 70

4.1 The method of temperature measurement of trapped ions 95

5.1 The collisional interaction potential used in the Monte Carlo simulation 113

6.1 The cooling process 133

6.2 The bias potentials used in the transmission measurement experiment with the skimmer type exit 151

6.3 The trap parameters sa a function of q 155

6.4 The bias potentials used in the transmission measurement experiment with the miniature quadrupole exit 160

0.1 Abstract

The buffer gas cooling process and the properties of the cooled beam in a novel rf quadrupole ion beam guide with axial field was studied. The operation principle of the axial field quadrupole ion beam guide is similar to the quadrupole mass filter operating in AC only mode but the rods were segmented and differential DC biases were applied to produce the axial field. It was operated in buffer gas.

A Monte Carlo simulation was developed and the simulation results were compared with the experimental results. The beam distribution in a thermal equilibrium was assumed as the thermal equilibrium distribution in a simple harmonic motion with rf distortion and the assumption was confirmed by the Monte Carlo simulation.

The temperature of the cooled beam was measured with a beam profile measurement system which consists of a miniature quadrupole ion beam guide and a rotating semi-circular Faraday plate. The temperature of the cooled beam was measured to be $0.0424 \pm 0.0026\ eV$ in the experiment while that of the simulated beam was $0.0372 \pm 0.0009\ eV$. The variation of beam temperature with beam current was $0.0153 \pm 0.0026\ eV/nA$. The maximum achieved ion transmission was 80 %. The transmitted ion beam's energy spread was measured with a retarding potential energy analyzer to be less than $0.1\ eV$. The cooling time was $0.7\ ms$ with $1V/cm$ axial field and was was observed to be very dependent on the ion current when there was no axial field.

0.2 Résumé

Dans la présente étude, nous avons étudié le refroidissement d'un faisceau d'ions par l'intermédiaire d'un gas tampon, à l'intérieur d'un guide à ions à champ électrique quadrupolaire auquel a été ajouté un champ axial statique. Le principe d'opération d'un guide quadrupolaire à champ axial est assez semblable à celui d'un spectromètre de masse quadrupolaire qui fonctionnerait en mode alternatif seulement, et auquel on aurait segmenté les tiges en plusieurs morceaux, chacun à un potentiel différent de sorte à former un champ continu en étages dans la direction axiale, et que l'on aurait opéré au sein d'un gaz tampon.

Nous avons développé une simulation Monte Carlo, dont nous avons comparé les résultats avec nos donnés expérimentales. Nous avons supposé que la distribution des ions dans le faisceau en équilibre thermique était celle que l'on aurait trouvé dans un potentiel harmonique simple, que l'on aurait transformé linéairement pour l'ajuster à l'état actuel du champ RF (radio-fréquence). Cette supposition à été confirmée par la simulation.

La température du faisceau refroidi à été mesurée grâce à un système composé d'un guide quadrupolaire miniature et d'une plaque de Faraday semi-circulaire tournante. De cette manière, nous avons mesuré une température expérimentale de $0.0424 \pm 0.0026\ eV$, tandis que celle de la simulation était de $0.0372 \pm 0.0009\ eV$. La température variait en fonction du courant ionique à un rythme de 0.0153 ± 0.0026 eV/nA. La transmission maximale des ions, que nous avons obtenue, était d'environ 80 % . L'étendue de l'énergie cinétique du faisceau ionique à été mesurée à l'aide d'un analyseur d'énergie à potentiel décélérateur, et nous avons trouvé qu'elle était contenue dans un intervalle de 0.1 eV. Le temps de refroidissement était de 7 ms (pour un champ axial de 1 V/cm), et nous avons observé que ce temps dépendait fortement du courant ionique lorsqu'il n'y avait pas de champ axial appliqué.

0.3 Acknowledgement

I wish to express my sincere gratitude to Dr. R. B. Moore for his patience and continuous support in helping me complete this work, even during unproductive periods, and for his help to finish this thesis writing. Without his software (RFQ-EXT simulation), my hardware (beam profiler) would not have been meaningful.

Much of my research was done with Van Fong's help. When we started developing a Monte Carlo simulation, we did not expect that it would take more than one month but it took us half a year to fix all the bugs. We had results, which were turned out to be incorrect, several times, but despite that, we continued and now we believe that the simulation works properly. I would like to express a special thanks to him.

I wish to thank Dr. Mohammed for sharing his laboratory know-how, such as the secret of ion source filling to produce right ion current without burning the heater; and Peter for helping me with his computer simulation and Macintosh computer maintenance. Jordi, as a summer student, helped me to make this thesis readable and Sherry helped me with drawings last summer. Alban, Nick, Anders and Thomas have all shared the laboratory and equipment with us as well as our successes. I would like to thank all of them.

Special thanks are due to the professors and staffs of the Foster Radiation Laboratory whose encouragement and help made me comfortable conducting my research here.

Lastly, I would like to thank my wife, Mija, who sacrificed herself to support my study without complaining; Hyunmo, my son, and Hyuna, my daughter, who give me great joy. I thanks to them all.

Chapter 1

Introduction

The subject of this thesis is the buffer gas cooling of ions, and the properties of the resultant cooled ion beams, in a quadrupole ion guide. It is part of the more general subject of ion-molecule interactions in radio frequency electric fields which, itself, is part of the subject of the cooling of charged particles in electromagnetic containment devices.

The cooling of particles contained in electromagnetic devices has recently become of very great interest. In physics this is because of the spectacular results that have been achieved by such cooling. Perhaps the most widely known are the Nobel Prize winning work of Dehmelt on cooled electrons, which resulted in a thousand fold enhancement of the measured accuracy of the electron g-factor [Dyc78], the laser fluorescence of single cooled ions in a trap [Deh88], which may lead to atomic clocks of significantly greater accuracy than the present cesium clocks, and most recently the production of a new form of matter, the Bose-Einstein condensate [Bra95, Dav95], by laser cooling of atoms in an combined magneto-optical trap.

By comparison, the subject of this thesis may appear mundane. It deals merely with the cooling of ions, contained by radio frequency electric fields, so as to improve

the performance of instruments that are used to detect and observe those ions. Yet this subject is of great practical importance, ranging from the identification of trace molecules in biological systems to the measurement of the nuclear mass of accelerator-produced radionuclides that exist in nature only in the interior of exploding stars, if indeed this can be regarded as of "practical" importance. For these purposes, the cooling of ions can be regarded as a means to observe the ions of interest by greatly increasing the signal to noise ratio of the observations. Essentially, this is accomplished by reducing the phase space volume of the ions, i.e. the six-dimensional volume of the ion excursions in space and momentum.

The subject of particle densities in phase space is therefore central to this thesis. Of particular importance is the phase space density of charged particles contained by electromagnetic fields. In general, devices that contain particles by using such fields are called "electromagnetic traps". The traps of interest in this thesis are those that use only electric fields, in particular those that use the simplest possible form of electric trapping field: an oscillating electric quadrupole field. The basic principles of such traps will therefore be introduced.

1.1 Ion trapping and cooling

1.1.1 Description of ion traps and their use

An ion trap is an electrode structure which, by the application of AC and/or DC potentials and possibly the addition of a magnetic field, confines the motions of charged particles to a small region of space. The two dimensional trapping action of an oscillating azimuthal quadrupole electric field, achieved by using four hyperbolic cylinders mounted symmetrically about a central axis as shown schematically in Figure 1.1(a), was discovered independently by Paul and his colleagues [Pau53] and by Post [Pos53]

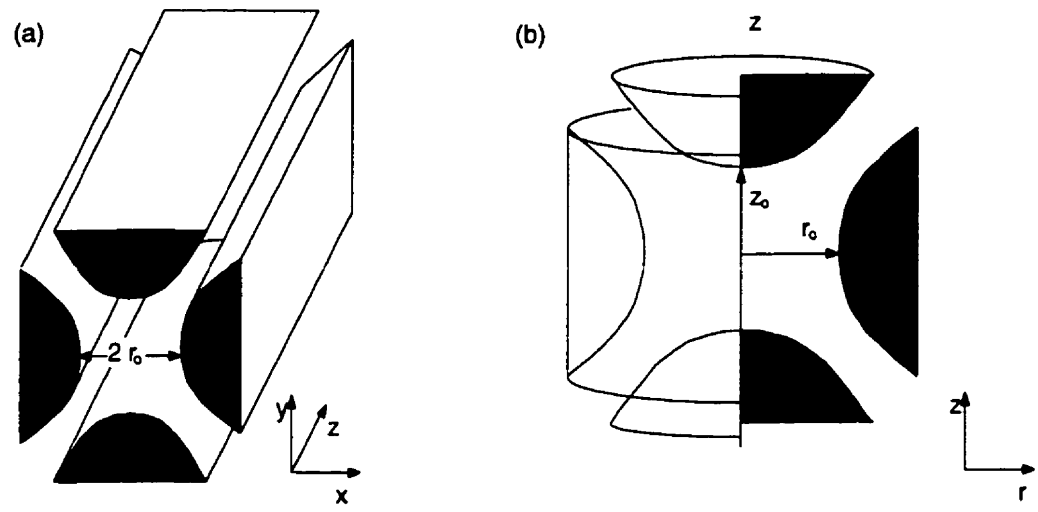

Figure 1.1: (a) The quadrupole ion guide; (b) the Paul trap.

in 1953.

The axial motion of the ions in such a device remains free. It is therefore commonly referred to as a "radio frequency quadrupole (RFQ) ion guide". However, by application of the proper amount of non-alternating (DC) quadrupole field, the radial confinement can be made to be dependent on the mass of the ion. In this mode of operation, the device is commonly referred to as an "RFQ mass filter".

In 1953, Paul extended this concept to form a full three dimensional trap using the azimuthally uniform electric quadrupole field achieved by electrodes that form hyperboloids of revolution, as shown schematically in Figure 1.1(b).

This device is now commonly referred to as the "Paul trap". Its operating features have many similarities to those of a two dimensional rod structure and its operational principle is the same.

In an alternating inhomogeneous field, the net force on the ions, averaged over one cycle, and the over all motion of the ions can be described roughly by introducing

a "pseudo-potential" which is independent of time.

Unlike the real potential, the pseudo-potential can have a minimum at the same position in space for both the negative and the positive ions, thus trapping both types at once.

The formation of such a pseudo-potential well by an oscillating non-uniform driving force has been known since the 19th century from the study of planetary motions. The mathematical description of the resultant motions is due to Mathieu, and is presented in the next chapter of this thesis. Here, as an introduction, only a qualitative description will be given.

The argument is quite simple. Consider the total effect of an oscillating inhomogeneous electric field over one cycle. Over exactly one-half of the cycle the ion is being pushed toward the stronger electric field region (away from trap center) while over the other half it is being pushed toward the weaker region (toward trap center). However, the push toward the stronger field, which occurs while the ion is in the weaker field, will be weaker than the push toward the weaker field region. Hence the ion will progress toward the weaker field. Since the weakest field of a quadrupole is at its center, where it is in fact zero, the ions will be driven to collect about that point.

This ion trap, along with another ion trap invented by Penning and using a high magnetic field, is regarded as a great discovery in science. For their development of ion-trap spectroscopy and for their use of it to study the properties of single electrons and ions, Paul and Dehmelt shared the Nobel prize with Ramsay in 1989. For an increasingly wide range of experiments, the ion trap is the best device to use and in many cases it is the only device with which the experiment can be performed. It already has many applications and it remains to be studied for possibly many more. It's attraction lies in its confinement of charged atoms or molecules in three dimensional space for long periods of time without any interaction with material walls that would disturb the exhibition of the ions' atomic or molecular properties.

Furthermore the confinement can be made mass selective so that even contaminate ions in the collection itself that could interfere with sensitive observations, can usually be removed. Trapping techniques have been used in atomic and molecular physics as well as in the study of chemical reactions. The mass selective confining properties of ion traps lead to practical uses in the analysis of chemical and bio-molecular structures by mass spectrometry as well as in nuclear physics where one can determine nuclear binding energies by precise mass measurements.

The physical properties of the collections of ions in a trap are themselves the subject of a new field of physics and chemistry. Ion clusters in a trap are an example of the formation of nano-structures in an artificial environment. Artificial atom formation in traps is already an important field of ion trap physics. Also, the artificial melting of crystals by cooling in a trap is an example of new phenomena in physics [Blu95].

1.1.2 Ion cooling and its benefits

The cooling of the ions in traps is an important method related to the trapping technique. The cooling process extracts kinetic energy from the ions, resulting in many benefits, the most important perhaps being that it reduces the loss of ions due to their boiling out of the trap, therefore it increases the trapping time.

Another important benefit is that ion cooling drives the ions to the center of the trap [Daw77, Hem92] and increases their cloud density. It therefore increases the precision of experiments such as the measurement of their masses [Sta84], magnetic moments, and optical spectra. In spectroscopy, cooling reduces the Doppler broadening and Doppler shift of the spectral lines. Cooling reduces the line broadening caused by first and second order Doppler shifts and additionally, second order Doppler shifts can only be reduced by cooling. Cooling leads ions into a smaller spatial extent where

the electric field is more ideal and this results in a more precise measurement of the masses and g-factors [Dyc85, Bro86, Cor89, Sto90].

Also some phenomena, such as the formation of ions into crystalline structures mentioned above, can be induced only at low temperatures. When the Coulomb interaction potentials involved become larger than their kinetic energies, they can form ordered structures [Wue59, Win87, Die87, Gil88, Hof88, Sau88, Rai92, Wal94].

Finally, in some experiments, ions cannot be produced in a trap designed for observation but must be introduced from an external source. In such cases, the ions produced by the source may not be suitable for delivery to the observation trap, the possibility of trapping external ions being related to their energy and to their phase space volume. If these are too great, they can be reduced by cooling before the ions are delivered to the observation trap, possibly in an external trap designed specifically for that purpose.

1.1.3 Ion phase space distribution and temperature

As indicated above, the phase space volume of a collection of ions is a very important parameter for any experiment on those ions. More specifically, to extract measured values for ion properties such as their masses, from observed signals, the ion density at any point in that 6-D phase space is very important.

In general, the phase density of a collection of particles in a trapping field will depend on the volume and momentum distribution with which they were introduced into that field. The subsequent evolution of that distribution will be influenced by the interactions of the ions with the field, gas molecules in the trap and with themselves. If the ions have been in the field long enough, then the interaction processes will cause the initial phase space distribution to evolve into that which is statistically most probable. The completion of this evolution is, of course, what is commonly

referred to as reaching "thermal equilibrium".

Thermal equilibrium for the distribution of phase space density of an ion collection in a field region leads to the concept of the temperature which characterizes that distribution. A simple interpretation of this temperature is that it is related to the mean kinetic energy of the ions in the collection. Thus the higher the temperature is, the greater are the momentum excursions of the ions, and consequently the greater the spatial excursions of the ions and the larger the phase space volume of the ion collection. Thus the cooling of an ion collection, in association with the reduction of its spatial and momentum extents, can indeed be related to a lowering of the temperature of the collection.

The relationship of the temperature of an ion collection in a radio frequency quadrupole field to the mean kinetic energy of the ions in the collection will be discussed more fully in Chapter 3. What we want to emphasize here is that the temperature of the ion distribution, together with the parameters of the confining field, completely determine the phase space density of the ions within the field. This, of course, implies that thermal equilibrium has been reached. Of course, no temperature can be defined unless thermal equilibrium has been reached.

Thus, establishing the temperature of an ion collection, together of course with the ion number, establishes the ion density distribution in phase space. From this distribution, many parameters of interest in experiments can be deduced. Examples are the line broadening in spectroscopic studies due to Doppler shifts, the reaction rates in chemical reactions that are energy dependent, the resolution of a mass filter, the signal intensity in atomic spectroscopy, and the transport efficiency of quadrupole ion guides.

Thus, the temperature of an ion collection can describe not only the rms velocity, mean velocity and mean spatial width of the collection, but also the whole momentum and spatial distribution.

1.2 This study

The subject of thesis is the study of ion beams cooled by buffer gas in the two dimensional electric quadrupole field of an axial field rf quadrupole (AXF-RFQ) ion beam guide. The work was inspired by the results achieved by Douglas [Dou92] at SCIEX, a major mass spectrometer company in Toronto, who first used such a structure in guiding ions into a mass spectrometer using buffer gas cooling quadrupole. The AXF-RFQ ion beam guide is essentially an RFQ mass filter running in AC only mode, sometimes referred to as "total transmission mode", but with an electric field along its quadrupole axis to lead the ions along the guide. The dynamics of the confined ions with the axial field are very similar to those without the axial field.

The axial field was applied to improve the transmission at high pressures and to shorten the time that the ions remained in the guide. Douglas, who did not have such a field in his system, reported that the transmission with the buffer gas cooling ion beam guide increased with the buffer gas pressure up to a certain pressure and then decreased. The decrease in the transmission at the high pressures appeared to come from the axial energy decay and the stopping of the ions within the ion guide. By applying an axial field, it is possible to maintain a high transmission at higher buffer gas pressures, making short cooling times possible.

There are several cooling techniques that have been applied to trapped ions, the most common of them being laser cooling, cooling by passive reaction of the ions with the currents they induce in the external circuit, active cooling using electrodes that sense the ion motion and feed back signals of the right polarity to damp that motion, and collisional cooling by interaction with light buffer gas molecules. For the applications related to this study, specifically the containment and cooling of ions from an Atmospheric Pressure Ion source for Mass Spectrometry(API/MS) and also radioactive nuclide mass measurements, the cooling system should cool a large

number of ions in a very short time, and be applicable to wide variety of ions. For these application, only buffer gas collisional cooling is feasible. The only drawback of this method is that the final ion temperature is much higher than that which can be achieved, in principle, by the other methods, since the ions cannot be cooled to a temperature that is lower than the temperature of the buffer gas itself. However, since that temperature for non-refrigrated buffer gas is essentially room temperature, or $k_B T = 25\ meV$, this limitation is acceptable for the intended applications.

Previous studies on the buffer gas cooling of trapped particles have been reported only for the three dimensional Paul trap. For the quadrupole mass filter or the quadrupole beam guide, the cooling effect has only recently been recognized by Douglas [Dou92]. Therefore the references of the buffer gas cooling are of the buffer gas cooling in the Paul traps.

The main purpose of this study is to understand the processes behind buffer gas cooling so that it can be applied more effectively to other experiments that could benefit from this technique.

1.2.1 The physics of buffer gas ion cooling

One purpose of this thesis is to study the ion buffer gas cooling process in a quadrupole field. This includes the study of the cooling process and of the statistical properties of the cooled collection. The conceptual diagrams of the subject of the study are shown in Figure 1.2 and Figure 1.3. The study will result in a better understanding of buffer gas cooling and of cooled beam dynamics in an ion guide and this will lead to the understanding of the optimal design of a beam cooling system, including the operating pressure, the physical dimensions of the system and the operating conditions.

As mentioned above, temperature is an important statistical parameter in describing a cooled ion beam. However, different definitions of temperature have been used

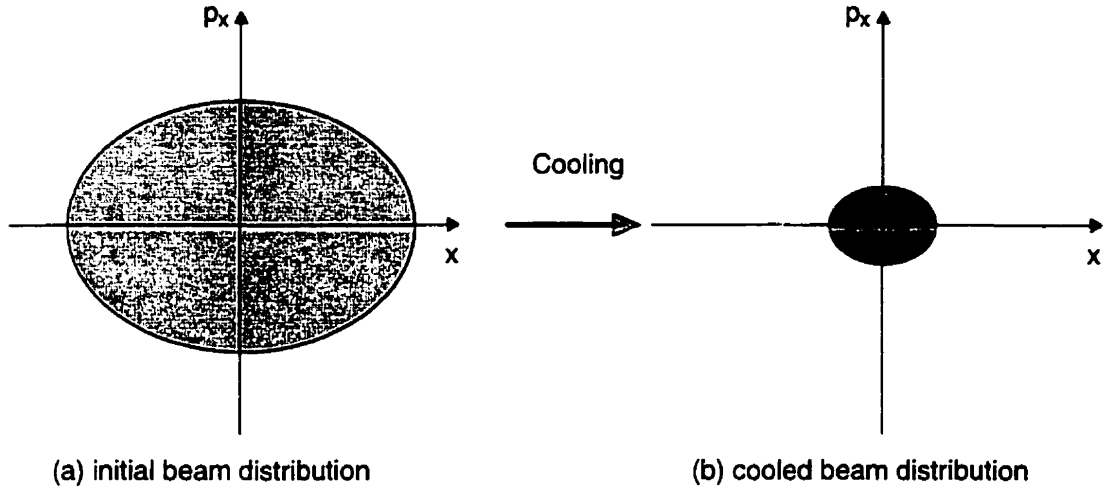

Figure 1.2: Schematic phase space diagram of the cooling process.

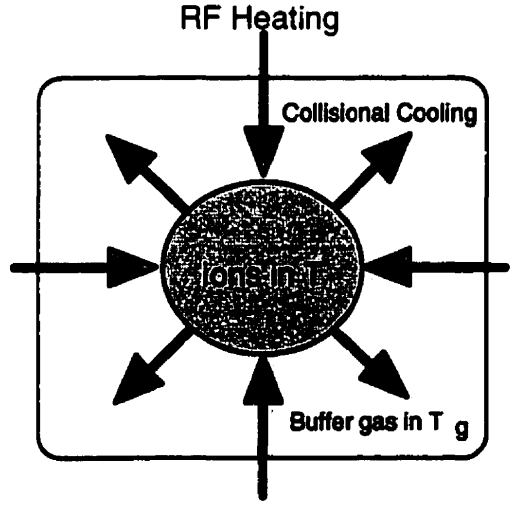

Figure 1.3: The model of thermal equilibrium in buffer gas cooling ion beam guide.

to describe cooled ion collections. The temperatures were reported without definition and the measured temperatures were compared with other measurements with different definitions.

In the present work, these different temperatures have been compared and their relationships studied with respect to the temperature definition that was used by us. The other temperatures as well as the average and rms velocities of the beam distribution can be calculated from that temperature.

The cooling process was studied experimentally and the results were compared to numerical simulations. To understand the cooling process, mathematical models were developed and used in the simulation. A Monte Carlo simulation based on realistic collision potentials with dynamic neutral gas movement was developed and used to study the cooling process. The cooling process of initially energetic external ion beam was classified as three stages by the major processes. The stable q value expansion by buffer gas collision at high buffer gas pressure were measured and compared with the simulation results.

To study the dynamics of the cooled beam, the beam was extracted from the quadrupole system by an electric field and was directed to a detector that measured its profile. A phase space simulation was developed to deduce the original beam profile in the quadrupole beam guide from the distribution at the detector and the temperature was calculated from this beam profile. The cooled beam profile at the detector was measured and compared with simulations.

The simulation results are in good agreement with the experimental results for the cooling times, the resultant beam temperature as well as the enhancement of the trapping properties of the quadrupole field by the buffer gas (see Chapter 4). This is the first time that measured temperatures of ions in a radio frequency quadrupole field have been compared to the temperatures deduced from a Monte-Carlo simulation.

1.2.2 Application of the results

Atmospheric Pressure Ion (API) sources are very popular in analytical chemistry and in the study of bio-molecules using mass spectrometry methods. There are various ionization techniques used in API sources, including inductively coupled plasmas, corona discharges, lasers, electrospray and ion spray ion sources. To analyze the masses of the ions, the ions created in atmosphere are introduced into a mass analyzer at high vacuum. A differential pumping system involving several stages is commonly used to achieve high transmission efficiencies. If the ion beam can be cooled and confined to the orifice separating vacuum stages the transmission and the sensitivity can both be improved. A schematic diagram of a commercial system is shown in Figure 1.4(a). The research reported here should help to determine the optimal pressure range for buffer gas cooling, the cooled beam distributions and their temperatures. These results could then be used to improve performance.

In another important application, experiments such as the nuclear mass measurements at the ISOLTRAP facility at CERN [Bec89, Klu92], use the beam of radionuclides delivered by the ISOLDE facility. This facility delivers a wide variety of radionuclides, produced by high energy proton bombardment of heavy metal targets. These radionuclides are extracted from the targets by evaporation at very high temperatures and delivered as high velocity ions, typically at 60 keV. To inject these energetic ions into a mass measurement trap, they must be slowed down. Several methods have been implemented to achieve this. The most widely used has been that of bringing the ions to rest by implantation into a thin foil. The added atoms in the foil matrix are then evaporated by heat and reionized by interaction with the hot foil surface as they leave. However, this technique is limited to alkali metals and alkali earths that can be so ionized.

A Paul trap mounted on a voltage pedestal so that the incoming ions are slowed

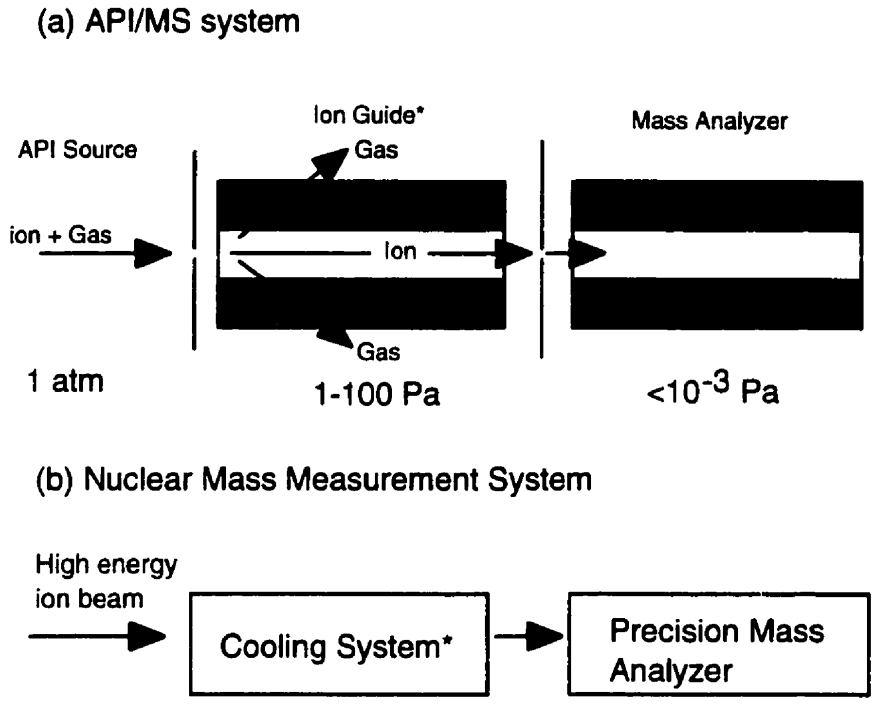

Figure 1.4: Schematics of (a) Atmospheric Pressure Ion(API) source mass spectrometer and of (b) Nuclear mass measurement system. *: related with this study.

electrically before their entry into the trap, and using buffer gas to capture and cool these incoming ions was proposed by Gullick and Moore [Gul86] as a means of collecting and cooling ions without having them neutralized in the process. A prototype system was developed by Rouleau [Rou92] and installed on the 60 keV beam line of the ISOLDE II facility. A capture efficiency of 0.2 % was demonstrated even for this relatively small trap, indicating that a larger trap with a larger phase space volume could have a higher capture efficiency.

Inspired by the results of Rouleau's work, a very large Paul trap (VLTRAP) was developed and has been installed at the new ISOLDE facility [Moh96]. In off-line

measurements with cesium ions this trap did indeed capture ions with a considerably higher efficiency than the trap used by Rouleau—specifically about 4 %.

However, from on-line measurements at ISOLDE it appears that this high efficiency depends on having an incoming ion beam of very low phase space volume. The phase space volume of the ISOLDE beam is about 100 times that of the off-line ion beam used for testing the VLTRAP. There would therefore be a considerable advantage to cooling the ISOLDE beam before attempting to collect it in a trap.

Furthermore, it appears that an ion beam such as that of ISOLDE could be captured and cooled with 100 % efficiency in a quadrupole ion guide. This is because of the much greater buffer gas pressure that can be used in such a collection device, and the much greater axial path length that can be used to bring the ions to rest. By having the axial field of the guide form a potential well at the position where the ions have come to rest, the guide itself can be made into a 3-dimensional trapping system. While the small size of such a trap would allow only very small numbers of ions to be collected, the collections would form very quickly and could be ejected as pulses into the VLTRAP system. Since pulsed injection into a Paul trap has been demonstrated with close to 100 % efficiency [Cra93], the resulting system would achieve close to 100 % overall efficiency of collection of the ISOLDE beam.

1.3 Contributions of this thesis

- A new ion beam cooling system was developed and tested.

  Buffer gas cooling within a quadrupole mass filter was discovered by Douglas and French [Dou92] and the axial field quadrupole concept was conceived at SCIEX [Jol95] and at McGill [Kim95]. The cooling system accepts a continuous beam and has a high capture efficiency (80% with a 50 eV injection energy). It

also has a short cooling time (1 ms) and small cooled beam emittance.

- A Monte Carlo simulation program was developed to understand the cooling process as well as the statistical properties of the cooled ion beam.

  The simulation uses a scattering model based on a realistic ion-neutral molecular interaction potential and includes the thermal motion of the buffer gas. This is the first simulation of ions in buffer gas with electric fields to use a realistic collisional interaction potential and it will surely give better predictions of the cooling process and of the statistical properties of the cooled beams, than the approximate hard sphere potential models that have been used in previous studies of ion mobility in gases. It should also provide a new standard for testing the approximate commonly used potential models.

  The simulation agrees well with the experimental results for temperature, transmission, maximum stable q value expansions for high buffer gas pressures and cooling times.

- The relations between the different definitions of temperature for the ions in a trap were established and the rms and mean velocities of the ions were expressed in terms of these temperatures.

  A temperature based on the pseudo-potential model with rf distortion is suggested here as a standard temperature definition and the relationship with the other temperature has been established by numerical methods.

- A new model of the profiles of cooled ion beams in quadrupole beam guides was developed, based on the Boltzmann distribution.

  A mathematical model was developed for this work which uses Boltzmann distributions within the pseudo-potential well and includes the rf distortion in phase space. The distribution has been converted to a spatial distribution. The

distribution changes periodically with time and the time averaged distribution was calculated by taking the average of distributions for 20 different rf phases.

- A new method of temperature measurement of an ion beam was developed.

  The measurement system consists of a miniature quadrupole ion guide, a beam profiler and an analysis program. The miniature ion guide was necessary as a transition device from the relatively high buffer gas pressure of the main quadrupole ion guide to the necessarily low pressure region of the detector. Essentially, the problem is that of accelerating the ions to adequate energy for the beam to be profiled by the detector without introducing disturbances by gas scattering in the acceleration region. The miniature quadrupole ion beam guide was designed to keep the ions under buffer gas cooling as the buffer gas pressure itself dropped to insignificance in the high vacuum region.

  A beam profiler, i.e. a semi-circular Faraday plate which rotates off axis with respect to the miniature quadrupole beam guide, was developed to measure the profile of the ion beam extracted from the quadrupole field. This beam profiler presents an integration of the beam current density as it sweeps across the beam.

  The beam profile at the detector is different from that in the quadrupole ion guide because the ion beam experiences the non-uniform quadrupole fringing field at the ends of the rod structure and the DC extraction fields. To deduce the beam profile in the quadrupole field from the profile at the detector, a computer simulation was developed. The program uses matrix methods to calculate the beam envelop evolution by using phase space ellipses running from the miniature quadrupole for 20 different starting rf phases, all the way to the detector. With this program, the profile of an ion beam in the guide can be calculated from the beam profile at the detector. From this profile the temperature of the ion

beam in the ion guide can be deduced.

The distribution and temperature of the ion beams have been measured. These temperature measurements represent the first such measurements of temperature for an ion beam in a quadrupole beam guide. The measurements were compared to that of the Monte Carlo simulation, with excellent agreement, demonstrating that the cooling process is well understood.

Chapter 2

Theory of Trapping and Cooling

This chapter presents the theoretical models necessary to understand the buffer gas cooling of the ions trapped in an oscillating quadrupole field as well as the resulting equilibrium state of the collection. The theory will be presented in the context of ions in a quadrupole ion guide. The principles covered are those of the operation of the ion guide itself, of the phase space dynamics of the ions in the quadrupole field and of the cooling process.

Most studies of ion dynamics, especially those involving quadrupole electric fields, have been carried out on ion motion in a vacuum. This thesis is concerned with motion in the presence of a buffer gas. However, since the effect of the buffer gas can be treated as a modification of the motion in a vacuum, the theories related to motion in a vacuum will be treated first and those pertinent to the effect of buffer gas will be discussed later.

2.1 Principles of ion trapping

Any charged particle tends to move to a lower or higher electric potential depending on the sign of its charge. Thus positively charged particles will tend to collect at a potential minimum while negative particles will collect at a potential maximum. Three dimensional confinement of a charged particle therefore requires an electric field which has a potential minimum (for positive ions or maximum for negatives) in all three coordinates.

The only field configuration that has a potential minimum in all directions from a point is that produced by an electric charge at that point. This is, of course, the trap provided by the atomic nucleus for its surrounding electrons. Traps have been built using the electric fields surrounding electrical wires but such traps can only contain particles that have sufficient kinetic energy for them to orbit the wires. Traps that must contain particles that have the lowest possible kinetic energies must have a vacuum at the trapping center.

However, because electric field lines are conserved in the absence of a charge, it is impossible to create a potential minimum, or maximum, in all three directions for a static electric field in a vacuum. Field lines that are directed from both sides toward a potential minimum in one direction must diverge in at least one of the two perpendicular direction from this center as they continue their progress through space. Thus a trapping field which has a potential minimum at a particular point in any one coordinate will necessarily have potential maxima at the same point in at least one of the two orthogonal coordinates. Similarly a potential maximum, which would trap negative ions, must have result in a potential minimum in at least one of the other coordinates.

The impossibility of confining charged particles in a vacuum by a static electric field led to the consideration of the effects of oscillating electric fields. This was in-

spired by the beam confinement achieved in high-energy particle accelerators using alternating magnetic forces along a particle's path [Cou52]. This led to the concept that alternating electric fields could achieve similar confinement. Since such an oscillating field would provide alternatively both potential maxima and potential minima, then it does not matter that the potential in one coordinate is a maximum when it is a minimum in another. Thus such a field would provide not only three dimensional confinement but also confinement of both positive and negative particles at the same time. The simplest electric field that provides a minimum, or maximum, is the electric quadrupole. For such a field the electric potential is purely parabolic, providing a potential well that results in purely simple harmonic motion within that well. This is the basic principle of the radio frequency quadrupole trap. (It is called radio frequency because the frequencies that must be employed for useful stable confinement of ions are in the radio frequency range.)

2.2 The quadrupole mass filter — an ion trap

Any arbitrary oscillating field with a local minimum or maximum potential in space can be used to confine ions. However, as pointed out above, the quadrupole field is the simplest and provides the simplest and most easily understood motion: the simple harmonic motion. It also has the advantage of being the easiest to construct and provides the strongest confinement for small excursions from the trapping center. This is because the higher order multipoles have potentials that are flat in the central region, rising sharply only at greater distances from the center, the higher the order of the multipole, the greater the distance at which this occurs. This is sometimes advantageous if a large region of gentle confinement is needed and ion guide devices have been built based on sextupole and octopole fields, which have potential that rise with the third and fourth powers respectively of the distance from the potential

minimum. However, for close confinement to the trapping center the quadrupole field is superior. This is why most of the trapping systems that have been studied use a quadrupole field and why that is the system used in this work. A not insignificant advantage of such a field is that the mathematics of the resultant ion motion can be relatively easily understood.

The electric quadrupole field is an electric field associated to an electric potential which has quadratic dependence to the position coordinates:

$$\Phi = \Phi_o(\lambda x^2 + \sigma y^2 + \gamma z^2). \tag{2.1}$$

where λ, σ, and γ are weighting constants and Φ_o is a coefficient that is independent of position and which may be a function of time. The associated quadrupole field has linear dependence on the position coordinate. In Cartesian coordinates,

$$\begin{aligned} \mathbf{E} &= -\nabla\Phi \\ &= -2\Phi_o(\lambda x\mathbf{i} + \sigma y\mathbf{j} + \gamma z\mathbf{k}) \end{aligned} \tag{2.2}$$

The equation is uncoupled in each coordinate, and the Laplace condition imposes a restriction on the constants (assuming no space charge within the quadrupole field).

$$\nabla \cdot \mathbf{E} = 0 \tag{2.3}$$

so that

$$\lambda + \sigma + \gamma = 0 \tag{2.4}$$

A quadrupole mass filter or ion guide also uses the conditions

$$\lambda = -\sigma;\ \gamma = 0 \tag{2.5}$$

The corresponding potential Φ can be expressed as

$$\Phi = \Phi_o \lambda (x^2 - y^2). \tag{2.6}$$

Such a potential can be generated by a set of four hyperbolic cylinders in which each pair of neighboring electrodes is oppositely biased. Because of difficulties in construction, most quadrupole mass filters employ circular rods with a radius

$$r = 1.148 r_o \tag{2.7}$$

where r_o is the distance from the axis to the rod. This approximation may cause field aberrations, but the field equipotential contours show good agreement [Day54][Den71] with the ideal quadrupole field in the central region. The quadrupole mass filter with circular rods is shown in Figure 2.1(a) and the equipotential lines are shown in Figure 2.1(b). If the distance between opposite electrode is $2r_o$ and the potential difference between neighboring electrodes is φ_o, then the potential function becomes

$$\Phi = \frac{\varphi_o}{2r_o^2}(x^2 - y^2). \tag{2.8}$$

The RFQ mass filter operates simultaneously with both a DC and an AC electric field:

$$\varphi_o = U - V \cos \Omega t \tag{2.9}$$

that is, a DC voltage U and a sinusoidal AC voltage with a zero to peak amplitude V and angular frequency $\Omega (= 2\pi f)$.

In vacuum, the equation of motion of the ions are of the form $m\ \ddot{x} = eE_x$. That is:

$$\begin{bmatrix} \ddot{x} \\ \ddot{y} \end{bmatrix} + \frac{e}{mr_o^2}(U - V \cos \Omega t) \begin{bmatrix} x \\ -y \end{bmatrix} = 0 \tag{2.10}$$

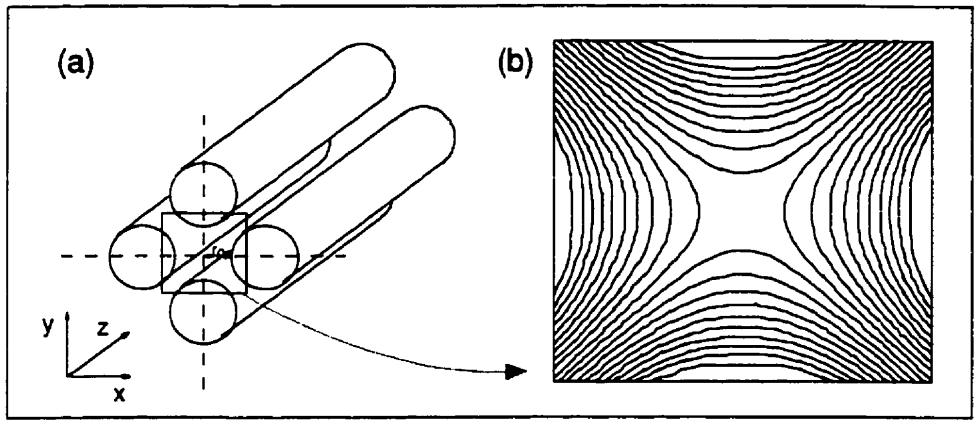

Figure 2.1: (a) The electrode configuration and (b) the potential distribution of an quadrupole mass filter with circular electrodes.

By defining two dimensionless parameters,

$$a_u = a_x = -a_y = \frac{4eU}{m\Omega^2 r_o^2} \tag{2.11}$$

$$q_u = q_x = -q_y = \frac{2eV}{m\Omega^2 r_o^2}, \tag{2.12}$$

and expressing time in terms of a parameter ξ where $\xi = \Omega t/2$, both equations of motion have the form

$$\frac{d^2u}{d\xi^2} + (a_u - 2q_u \cos 2\xi)u = 0 \tag{2.13}$$

where u represents either x or y.

Equation 2.10 is the Mathieu equation and Eq. 2.13 is its canonical form. The properties of the Mathieu equation are well-established and documented. Solutions

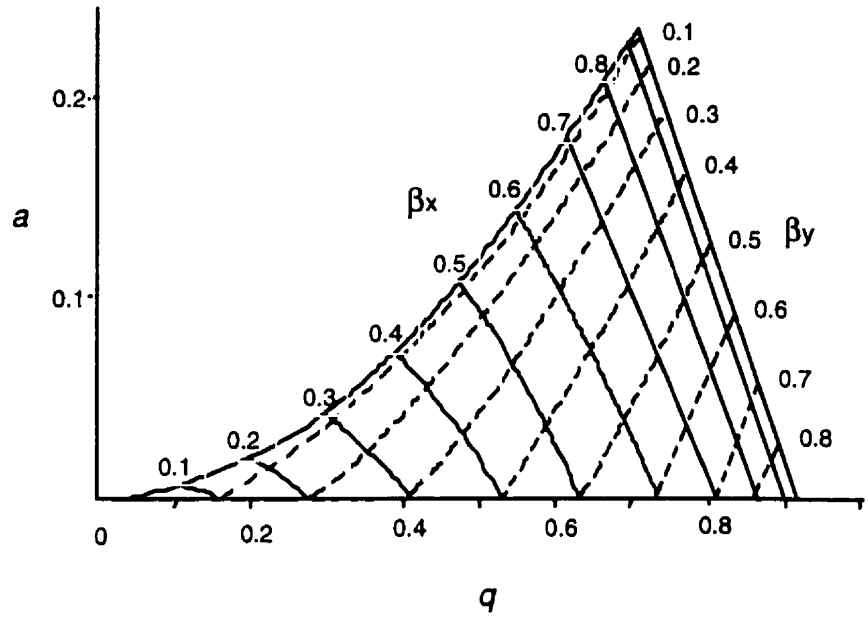

Figure 2.2: The stability diagram for the mass filter.

to this equation can be expressed as

$$u(\xi) = \alpha' e^{\mu\xi} \sum_{n=-\infty}^{\infty} C_{2n} e^{2in\xi} + \alpha'' e^{-\mu\xi} \sum_{n=-\infty}^{\infty} C_{2n} e^{-2in\xi} \tag{2.14}$$

where α' and α'' are integration constants that depend on the initial conditions: u_o, $\dot{u}_o$, and ξ_o. The constants C_{2n} and μ depend on the values of a and q and not on the initial conditions. The solutions are of two types, stable and unstable, depending upon the nature of μ, which may be real, imaginary or complex. When $\mu = i\beta$ and β is not a whole number, the solutions are periodic and stable. Since μ only depends on a and q, the conditions for stability can be represented in an $a - q$ diagram (stability diagram) as shown in Figure 2.2.

In the stable region, the general form of solutions can be written as

$$u(\xi) = \alpha' \sum_{n=-\infty}^{\infty} C_{2n} e^{(2n+\beta)i\xi} + \alpha'' \sum_{n=-\infty}^{\infty} C_{2n} e^{-(2n+\beta)i\xi}. \tag{2.15}$$

With the use of the trigonometric identity

$$e^{i\theta} = \cos\theta + i\sin\theta, \tag{2.16}$$

the expression for stable solutions becomes

$$u(\xi) = A \sum_{n=-\infty}^{\infty} C_{2n} \cos(2n+\beta)\xi + B \sum_{n=-\infty}^{\infty} C_{2n} \sin(2n+\beta)\xi \tag{2.17}$$

where

$$A = (\alpha' + \alpha''); \; B = i(\alpha' - \alpha''). \tag{2.18}$$

This shows that the stable solution is a superposition of oscillations of frequencies ω_n given by

$$\omega_n = (2n+\beta)\frac{\Omega}{2}, n = 0, 1, 2, ... \tag{2.19}$$

For low values of β (for 0 to $\simeq 0.4$), the terms with the first two lowest frequencies play a major role, and the typical ion trajectory takes the form depicted in Figure 2.3. The lowest frequency component is called the macro- (or secular-, or β-) oscillation, and its frequency is

$$\omega_0 = \beta\frac{\Omega}{2} \simeq \frac{q}{2\sqrt{2}}\Omega \quad \text{(for } \beta \leq 0.4 \text{ or q } \leq 0.5). \tag{2.20}$$

The macro-oscillation can be understood in terms of a pseudo-potential arising from the trapping effect. Disregarding the trajectory ripples arising from higher-order oscillations, it is just simple harmonic motion in this pseudo-potential well.

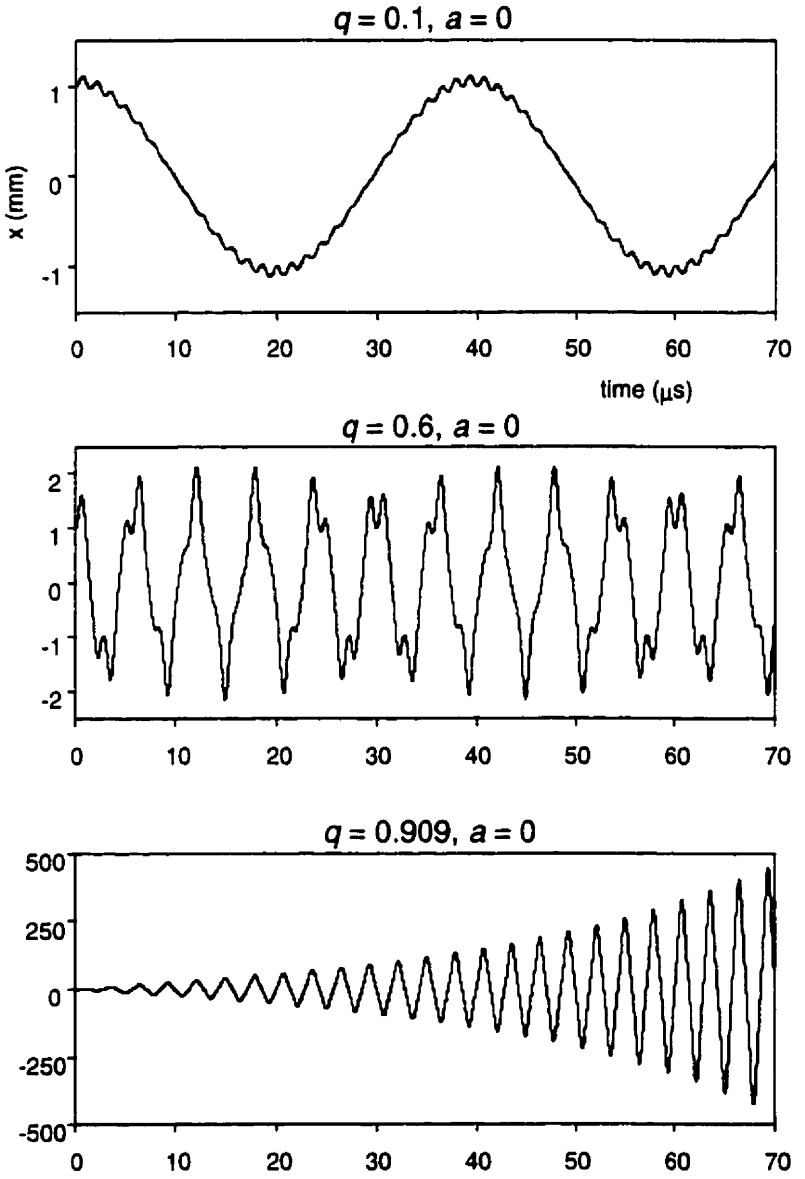

Figure 2.3: Ion trajectories for several points in the stability diagram.

This elegant approach was derived by Wuerker et al. [Wue59], Dehmelt [Deh67] and Major [Maj68] and was developed by Dawson et al.[Daw76].

We can thus consider the full motion in u (either x or y) to be composed of two components: a small displacement δ due to the micro-motion resulting from the high-frequency field oscillations, and a large macromotion displacement U which describes the extent of the motion, averaged over one period of the rf driving potential. Then,

$$u = \delta + U \tag{2.21}$$

If we assume that the driving force, which is related to the value of q, is small, we can then write $\delta \ll U$ while $d\delta/dt \gg dU/dt$. We can substitute these approximations into Eq. 2.13 to get

$$\frac{d^2\delta}{d\xi^2} = -(a_u - 2q_u \cos 2\xi)U \tag{2.22}$$

which, assuming $a_u \ll q_u$ and U to be constant, integrates to

$$\delta = -\frac{q_u U}{2} \cos 2\xi \tag{2.23}$$

Equation 2.23 indicates that the displacement due to the micro-motion is out of phase with the rf potential by half a cycle and also that it increases linearly with the secular displacement U. The approximate value for δ from Eq. 2.23 can now be substituted into Eq. 2.21 to give

$$u = U - \frac{q_u U}{2} \cos 2\xi \tag{2.24}$$

whence the original Mathieu equation, Eq.2.13, becomes

$$\frac{d^2u}{d\xi^2} = -a_u U + \frac{a_u q_u U}{2} \cos 2\xi + 2q_u U \cos 2\xi - 2q_u^2 U \cos^2 2\xi \tag{2.25}$$

Since the acceleration due to the rf drive $d^2\delta/d\xi^2$ averaged over one period of the rf drive is equal to zero, we have that the acceleration of the macro-motion averaged over the same period is given by

$$\left\langle \frac{d^2U}{d\xi^2} \right\rangle_{av} = \frac{1}{\pi} \int_0^{\pi} \frac{d^2u}{d\xi^2} d\xi \tag{2.26}$$

so that the integral of Eq. 2.25 taken between these limits is

$$\frac{d^2U}{d\xi^2} = -\left(a_u + \frac{q_u^2}{2}\right) U \tag{2.27}$$

which, written in terms of time, becomes

$$\frac{d^2U}{dt^2} = -\left(a_u + \frac{q_u^2}{2}\right) \frac{\Omega^2}{4} U \tag{2.28}$$

This equation corresponds to the simple harmonic macro-motion component U and is equivalent to

$$\frac{d^2U}{dt^2} = -\omega_0^2 U \tag{2.29}$$

in which ω_{ou} is the macro-oscillation frequency.

If we now consider the case of $a_u = 0$ and substitute for q_u in Eq. 2.28, we get

$$\frac{d^2U}{dt^2} = -\left(\frac{e^2V^2}{2m^2\Omega^2 r_o^4}\right) U \tag{2.30}$$

which, by a mechanical analogy, corresponds to motion in a pseudo-potential well of depth

$$\overline{D_u} = \frac{eV^2}{4m\Omega^2 r_o^2} = \frac{qV}{8} \tag{2.31}$$

Therefore we arrive at the pseudo-potential well model which suggests that when q is small and when the micro-oscillation is disregarded, the ion motion can be considered to be an oscillation in a parabolic potential well with a depth $\overline{D_u}$ [Deh67].

A similar technique is that of the smoothed general solution described by Bonner [Bon74], which includes the assumption that for lower value of β, the higher harmonics may be ignored and only the fundamental secular motion of the ion makes a significant contribution to the energy.

Figure 2.4 shows a typical ion trajectory at stable working conditions with the trajectory found by the well model.

Ironically, in most of the references [Tod80, March89-1, Daw76-1], the trajectory of ions with the Dehmelt model were drawn with a larger amplitude than is appropriate and the phase ellipses were also regarded as larger than they should be. The original Dehmelt's well model therefore appears to have been misunderstood. Therefore many of the results of using the well model are wrong. However, they still can contain some useful information.

2.3 Introduction to phase space dynamics

In this thesis, two different regimes were used in the study of phase dynamics: with and without buffer gas. Phase space dynamics will be introduced within the context of motion in the absence of buffer gas. This not only forms a basis for understanding ion motion in the absence of buffer gas but also provides a basis for understanding modifications to the motion caused by buffer gas.

In the absence of particle-particle interactions, i.e. for a sparse collection of particles in a high vacuum, the particle trajectories in an electromagnetic field can be determined by solving the Lorentz equation for that field. In order to obtain the solutions of this second order differential equation, it is necessary to know the particle's

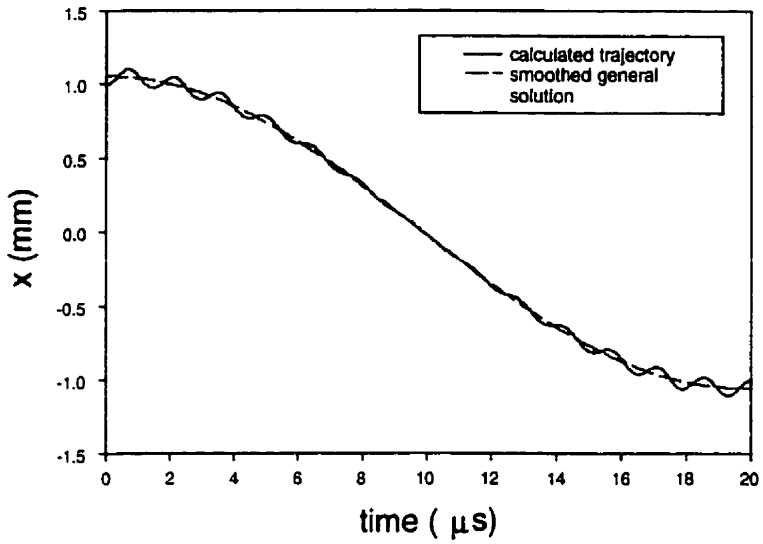

Figure 2.4: The trajectory and well model approximation for a=0, q=0.1.

position (x, y, z) as well as its momentum (p_x, p_y, p_z) at the starting time. Knowing the initial position of the particle in the six-dimensional "phase space", we can, in principle, then calculate the time evolution of the particle. More important to the present work, we can calculate the time evolution of a collection of particles. To describe such an evolution it is most convenient to use the concept of phase space.

2.3.1 Phase space properties of the ion motion

It can be shown that in force fields which can be derived from a Hamiltonian, the phase space volume that encloses a collection of particles is constant with time ([Ame57] section 101). Liouville's theorem generalizes this to the local density of the collection and may be expressed in the following way [Hua63].

> *"If we follow the motion of a representative point in phase space, we find that the density of representative points in its neighborhood is constant.*

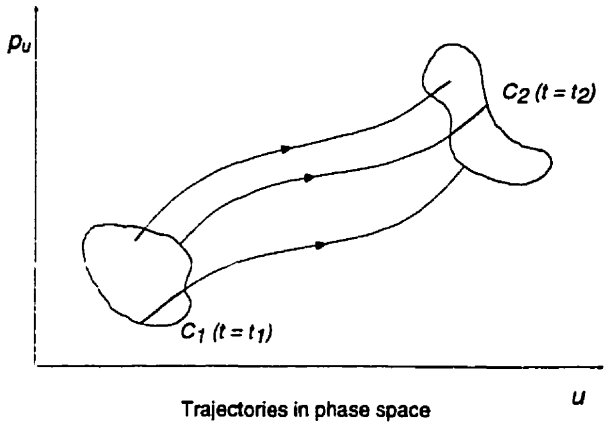

Figure 2.5: Phase space evolution of the boundary C_1 into the boundary C_2 over the time interval between t_1 and t_2.

> *Hence the distribution of representative points moves in phase space like an incompressible fluid."*

Thus, according to Liouville's theorem, a cloud of particles that fills a certain volume in phase space at a time t_1 may have a different shape at time t_2 but its phase space volume will remain the same so that the density does not change (see Figure 2.5). The theorem was originally derived for a non-interacting particle system but, in the statistical mechanics of interacting particles many of its features can be preserved. Essentially, while particle interactions can cause individual particles to move in and out of local regions of phase space, at thermal equilibrium the local density, on the average will still be preserved. This is because from statistical mechanics the local density at any point in phase space is determined by the overall properties of the force field and the temperature of the particle collection (See Introduction and Chapter 3.).

When the motions can be uncoupled as three independent components, Liouville's theorem can be applied to the projection of the phase space volume into each of the action diagrams (momentum versus displacement) associated with each coordinate. Expressing the area of this projection as the action S_u for the u coordinate:

$$S_u = \int dp_u du = const. \tag{2.32}$$

Thus the invariance of phase volume now transforms into a more easily understood concept: the individual invariance of the action of all three coordinates of the particle collection. The description of phase space volume can then be broken into a description of the individual action diagrams. This is very important in visualizing the evolution of a collection of particles in a trap, since the conceptually simple spatial view of the motion combines all three coordinates into a tangled web of trajectories, which have often no discernible pattern. This is particularly true for motion in rf quadrupole fields.

There are two important microscopic properties of the ion trajectories in phase space. The first is that the trajectories in phase space do not intersect at any given time. This is because the initial conditions uniquely determine the subsequent motion. If at a given time two particles are at the same point in phase space, the particles will then move with the exact same trajectory and this implies that the particles are identical. The second property is a result of the first. If a group of particles at a certain time t_1 is bounded in phase space by a boundary C_1, then at a time t_2, C_1 will have changed into C_2 which will enclose the exact same particles (see Figure 2.5).

These properties are extremely useful in analyzing large numbers of particles. If we can discover how a boundary evolves with time in an action diagram, then we will have accounted for the evolution all of the particles with values of u and p_u inside that boundary.

The evolution of an action diagram boundary can be expressed by a state transition matrix M defined by:

$$\begin{pmatrix} u \\ p_u \end{pmatrix}_{t_2} = M(t_2,t_1) \begin{pmatrix} u \\ p_u \end{pmatrix}_{t_1} \tag{2.33}$$

where u and p_u are a displacement and the associated momentum. This is a powerful method if the elements of M can be calculated easily. Essentially, all that has to be calculated is the evolution of the particle boundary, not the evolution of each individual particle within that boundary.

An action boundary of particular importance in ion motion is the ellipse. This is because the action trajectory of any particle undergoing simple harmonic motion is an ellipse. Also, many particle collections tend to have elliptical action diagrams, particularly those being delivered as beams through circular beam pipes, or being created from sources with a circular aperture.

Of greatest importance in the present work, the action diagrams for charged particle motions in rf quadrupole fields are elliptical, the details of which will be presented later. For now the general properties of elliptical boundaries in action diagrams will be discussed.

Elliptic boundaries in Phase space

The behavior of elliptical boundaries in action diagrams has been well studied [Lic69]. The equation of an ellipse can be written as

$$Cu^2 + 2Aup + Bp^2 = \epsilon \tag{2.34}$$

where ϵ is given by

$$\epsilon = \frac{\text{area of ellipse}}{\pi} \tag{2.35}$$

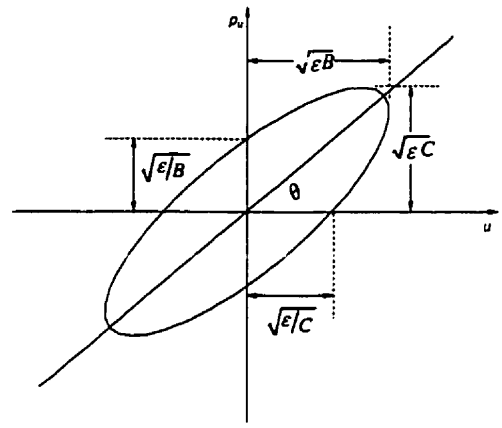

Figure 2.6: An ellipse with its critical values.

and

$$BC - A^2 = 1. \tag{2.36}$$

The angle θ, which the major axis of the ellipse makes with the u axis is given by [Smi10]

$$\tan 2\theta = \frac{-2A}{B - C}. \tag{2.37}$$

There are two interpretations of such an elliptical boundary [Lic69]. It may be thought of as the set of limiting values of u and p for which a particle-focusing system will transmit so that particles with values of u and p outside this boundary will be rejected. In this case it is called the *acceptance ellipse* of the system, whose area, proportional to the acceptance ϵ, represents the range of the initial conditions which the system will accept. An alternative interpretation is that the focusing system will transmit a beam of particles whose value of u and p are bounded by the ellipse, in which case ϵ is representative of the emergent beam and is called the emittance of

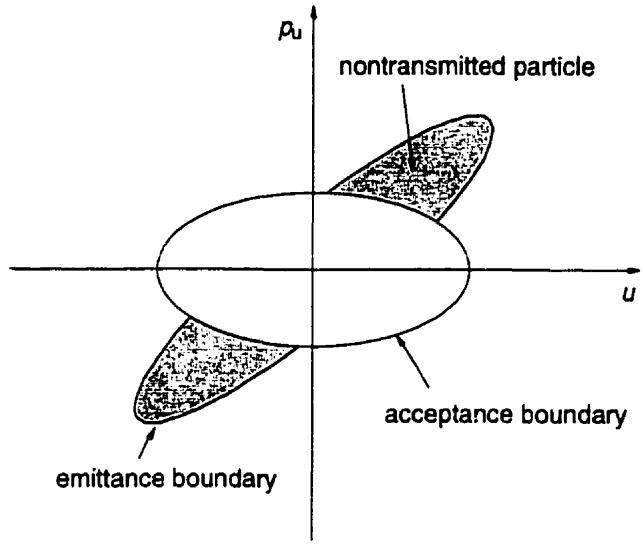

Figure 2.7: Emittance and acceptance diagram.

the *beam ellipse.*

2.3.2 Emittance and acceptance

One of the important applications of phase space dynamics is its use in determining the paths of particles through a focusing system so as to optimize these paths. For example, in this thesis we are concerned with the transmission of particles from an ion source to an RF quadrupole beam guide, and also of particles from an RF quadrupole beam guide to an analyzing or a collecting device.

The optimal transmission between two particle focusing systems will obviously occur if the emittance ellipse of the first coincides with the acceptance ellipse of the second. If the emittance ellipse of the first system has regions non-intersecting with the acceptance ellipse of the second system, the ions in the non-intersecting regions will be lost.

2.3.3 Time evolution of some simple ion collections

As mentioned above, we can simplify the representation of the ion beam evolution by using phase space dynamics, since we only need to calculate the evolution of the beam's boundary. To illustrate this the action diagram of some simple ion collections will be described.

Zero electric field region

The simplest example of an action diagram evolution is that of a collection of identical particles moving in a field free space. Since the motions for the three spatial coordinates are independent, the evolutions of the three action diagrams corresponding to the three spatial coordinates are independent and any one of these action diagrams will be representative of all the other evolutions. Consider then the x action diagram and, as a further simplification, suppose that it is as shown in Figure 2.8, where initially, the collection of particles occupies a rectangle of width Δx and height Δp_x centered about the origin of the coordinate axes. At a later time, all the particles will have retained their original momentum but their horizontal positions will have changed by an amount which is simply the product of their velocities with time, which is expressed in terms of p_x and the particle mass m by

$$dx = \frac{p_x}{m} dt \tag{2.38}$$

Since x is proportional to p_x, the points filling the original rectangle in the action diagram will move so as to fill the parallelogram shown in the Figure 2.8. It can easily be seen that the area of this parallelogram is the same as that of the original rectangle. Thus, while the spatial extent in x occupied by the particles actually expands due to the particle motion, the action is conserved. Similarly, the action areas are conserved for the y and z components of the motion. The six dimensional phase space volume

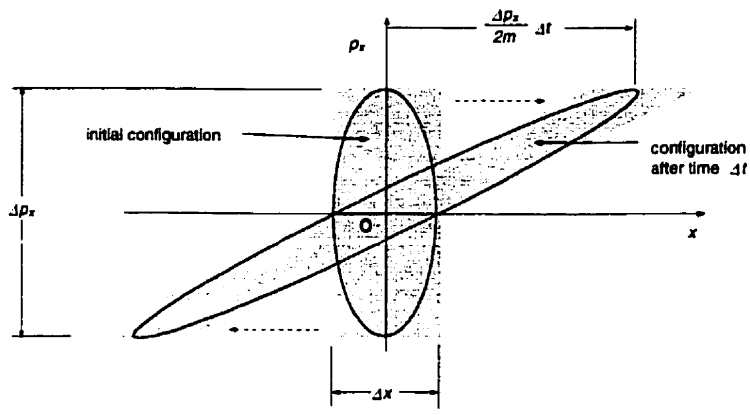

Figure 2.8: The evolution of phase space diagram for zero electric field region.

occupied by the particle collection will therefore also remain constant during the motion, this phase space volume being simply the product of the three action areas.

An important example of an action diagram for a collection of free particles is that of a beam of charged particles centered about a finite momentum in a given direction, in this case along the x axis. The only difference from Figure 2.8 is that the parallelogram for the x action diagram would move to the right by an amount equal to the central velocity multiplied by the time interval, while the transverse action diagrams for y and z would remain the same as the one for x.

The transformation matrix for this evolution in a zero field region is simply

$$\begin{pmatrix} x \\ p_x \end{pmatrix}_{t_0+\Delta t} = \begin{pmatrix} 1 & \frac{\Delta t}{m} \\ 0 & 1 \end{pmatrix} \begin{pmatrix} x \\ p_x \end{pmatrix}_{t_0} . \tag{2.39}$$

Uniform electric field

In this work, during the propagation of the ions between the miniature quadrupole and the Faraday detector, the ions experience axial and radial electric fields due to the

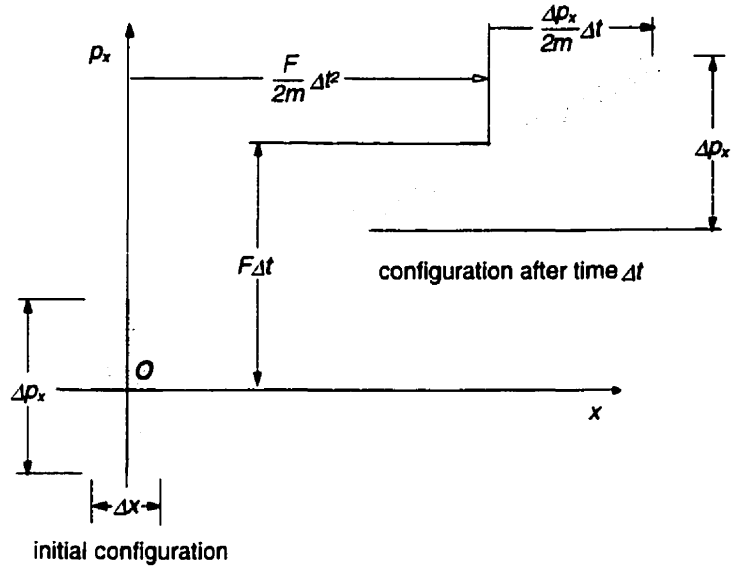

Figure 2.9: The evolution of a phase space diagram for a uniform electric field.

extraction potential and the rf fringing field. The axial component of the extraction field can be approximated by a sequence of narrow steps, the field being constant along each step. The changes in position and momentum for each time step are

$$\Delta x = \frac{p_x}{m}\Delta t + \frac{1}{2}\frac{F}{m}\Delta t^2; \quad \Delta p = F\Delta t, \tag{2.40}$$

which can be expressed as:

$$\begin{pmatrix} x \\ p_x \end{pmatrix}_{t_0+\Delta t} = \begin{pmatrix} \frac{1}{2}\frac{eE}{mx}(\Delta t)^2 \\ \frac{eE}{x}\Delta t \end{pmatrix} + \begin{pmatrix} 1 & \frac{\Delta t}{m} \\ 0 & 1 \end{pmatrix} \begin{pmatrix} x \\ p_x \end{pmatrix}_{t_0}. \tag{2.41}$$

The action diagram after the transformation is the same parallelogram as in Figure 2.8, except that it is now moved upward and farther to the right by the constant term in Eq. 2.40. Again, the action area of the collection is conserved (see Figure 2.9).

Electric field proportional to a displacement

In ion beam optics, the electric field of the quadrupole lens is an example of an electric field that is proportional to a displacement. In this case the electric field is transverse to the ion beam. Since it is a convention to use the z coordinate to represent the direction of an ion beam, the electric field of the quadrupole is in the x and y directions. Considering the x component of the field,

$$E_x = -\partial V/\partial x = ax \tag{2.42}$$

For particles of mass m and charge e, the Lorentz equations of motion simply becomes

$$m\,\ddot{x} = eax, \quad m\,\ddot{y} = eay. \tag{2.43}$$

These may be rewritten as

$$\frac{d^2x}{dt^2} - K^2x = 0 \tag{2.44}$$

where

$$K^2 = \frac{ea}{m}. \tag{2.45}$$

For a negative value of a, K^2 will also be negative, resulting in a simple harmonic motion with the solution:

$$\begin{pmatrix} x \\ p_x \end{pmatrix}_{t_0+\Delta t} = \begin{pmatrix} \cos K\Delta t & \frac{\sin K\Delta t}{mK} \\ -mK\sin K\Delta t & \cos K\Delta t \end{pmatrix} \begin{pmatrix} x \\ p_x \end{pmatrix}_{t_0}, \tag{2.46}$$

For a positive value of a, K^2 is positive resulting in

$$\begin{pmatrix} x \\ p_x \end{pmatrix}_{t_0+\Delta t} = \begin{pmatrix} \cosh K\Delta t & \frac{\sinh K\Delta t}{mK} \\ +mK\sinh K\Delta t & \cosh K\Delta t \end{pmatrix} \begin{pmatrix} x \\ p_x \end{pmatrix}_{t_0}. \tag{2.47}$$

In an infinitesimal time interval dt, the changes in momentum and position for such a force can be expressed as

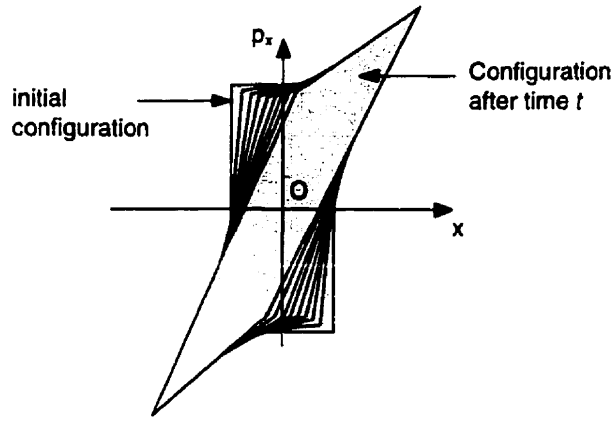

Figure 2.10: The evolution of phase space diagram for an electric field which is proportional to the displacement from the origin of the coordinate system.

$$dp_x = axdt \tag{2.48}$$

$$dx = \frac{p_x}{m}dt \tag{2.49}$$

Because of the linear dependence of dp_x on x and of dx on p_x, the transformation will change an initial rectangular action diagram into a parallelogram of the same area (Figure 2.10). Similarly, an elliptical action diagram will remain elliptical, although its tilt and its eccentricity will be changed.

This is the highest order force field that results in such a linear transformation. Forces that depend on higher powers of the displacement coordinate will distort straight lines in an action diagram into curves and will distort elliptical action diagrams into higher order shapes. Also, although the overall phase space volume of the ion collection will be preserved, the area of the action diagrams will not.

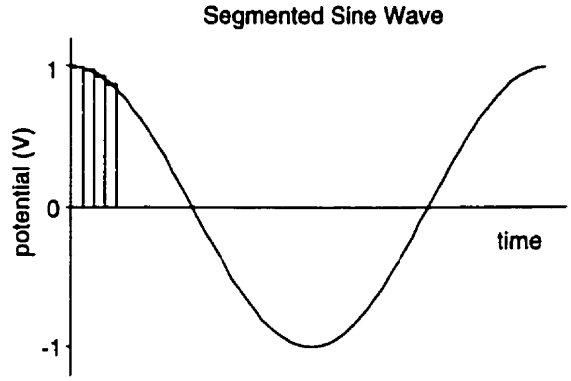

Figure 2.11: The periodic potential in a quadrupole mass filter can be approximated by piecewise constant approximation - for a short interval the potential can be considered as constant.

Action diagram for a quadrupole beam guide

For an electric quadrupole beam guide, the fields in the interior region are given by

$$E_x = -\partial V/\partial x = -ax, \tag{2.50}$$

$$E_y = -\partial V/\partial y = ay, \tag{2.51}$$

$$E_z = 0, \tag{2.52}$$

which yields constant field strength gradients in the transverse x and y directions.

As mentioned above, the stable boundary of the ions in phase space for a quadrupole trap can be expressed by an acceptance ellipse. The evolution of the ellipse can be found by applying successive transformation matrices. For the quadrupole beam guide, the electric field is not a constant but a periodic function of time. To find the transformation we can use a staircase approximation using appropriate short time intervals in which the potential can be considered constant (Figure 2.11). The transformation matrix can then be calculated for a specific time interval with a constant

electric field as shown above (see the subsection *Electric field proportional to a displacement*). The transformation matrix for longer time intervals can be calculated as a product of many such matrices over sub-intervals within that period. For example,

$$\begin{pmatrix} x \\ p_x \end{pmatrix}_{t_2} = M(t_2, t_1) \begin{pmatrix} x \\ p_x \end{pmatrix}_{t_1}, \tag{2.53}$$

and

$$\begin{pmatrix} x \\ p_x \end{pmatrix}_{t_3} = M(t_3, t_2) \begin{pmatrix} x \\ p_x \end{pmatrix}_{t2}, \tag{2.54}$$

result in

$$\begin{pmatrix} x \\ p_x \end{pmatrix}_{t_3} = M(t_3, t_1) \begin{pmatrix} x \\ p_x \end{pmatrix}_{t1}. \tag{2.55}$$

where

$$M(t_3, t_1) = M(t_3, t_2) \cdot M(t_2, t_1). \tag{2.56}$$

For a time interval at a specific rf phase the ellipse will be transformed into another ellipse with a common center, and over a complete rf cycle the transformations will change the eccentricity and orientation of the ellipse while keeping its area constant.

The electric field's x and y components have the same in magnitude but differ in sign. Therefore the phase space evolutions in $x - p_x$ space and in $y - p_y$ space are out of phase by 180°.

Circular symmetric lens

For a cylindrically symmetric system, the field can be divided into radial and axial components. The axial component pushes the ions along the axial direction and the radial component either confines or repels in the radial direction.

For a paraxial ion beam, the radial component of the electric field near the beam axis can be calculated from the field along the z axis. If the electric field along the

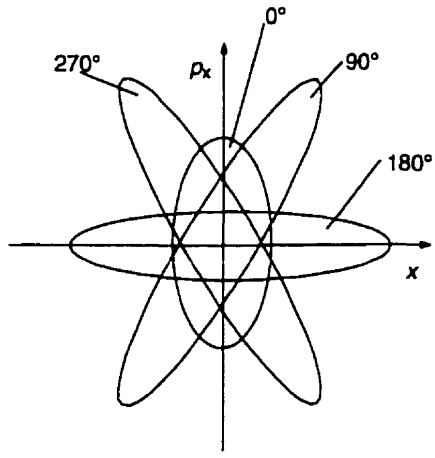

Figure 2.12: The action diagram in a quadrupole beam guide for for several rf phases. Zero phase is defined as the instant that the electric potential on the x rods is a positive maximum for positive ions.

axis is $E(z)$, there will be a radial component of the field near the axis given by the divergence equation as

$$E_r(r,z) \simeq -\frac{1}{2}r\frac{\partial E(z)}{\partial z} = -\frac{1}{2}r\frac{\partial^2\phi(z)}{\partial z^2} \tag{2.57}$$

Therefore

$$\frac{\partial^2\phi}{\partial x^2} = \frac{\partial^2\phi}{\partial y^2} = -\frac{1}{2}\frac{\partial^2\phi(z)}{\partial z^2} \tag{2.58}$$

From this the transformation matrix can be derived just as for the case of the quadrupole field, except that here the transformations for the $x - p_x$ and $y - p_y$ actions are the same.

2.4 Phase space dynamics and cooling

The above phase space considerations have been for ions in a perfect trapping field, that experience no collisions with background gas, electrode surfaces, or each other and that experience no disturbances from interactions with the electric potentials induced on the trap electrodes due to their own movements. Ions in a real trap experience all of these and no matter what their phase space distribution is upon their entry into the trapping field, they will finally reach a thermal equilibrium in which the heating and cooling effects of these interactions are balanced. The resultant phase space distribution, as pointed out above, is characterized by temperature.

The temperature of the final phase space distribution depends on the relative importance of the heating and cooling factors. In the sort of quadrupole ion guide under investigation in this work, the principle factors will be cooling due to collisions with the buffer gas molecules, evaporative cooling due to loss of ions from the trap and a process described as "rf heating", which is related to the space charge forces of the ion collection. These will each be briefly described here.

2.4.1 Collisional cooling

Major and Dehmelt [Maj68] have analyzed the ion-neutral particle interactions in a Paul trap by assuming that they were elastic collisions of ions of a mass (m) with neutral particles of mass (m_r) at rest. In reality, the buffer gas molecules are not at rest but have a thermal motion. However, the results of their analysis agree quite well with experiments that have been performed in traps, and so are generally accepted.

Major and Dehmelt considered that the effect of the ion-neutral collision may be considered to be one of three distinct cases. For $m \ll m_r$, they showed that the elastic scattering of the ions from the almost fixed centers of the neutrals due to the rf micro-motion results in the ion, on the average, gaining kinetic energy. Thus there

is collisional heating rather than collisional cooling. For the case when $m = m_r$, they argue that the mean kinetic energy of the ion will remain unchanged. For the third case, $m \gg m_r$, the neutral particles cause a viscous drag on the ions and thus reduce the average energy with time. This energy reduction process, which only occurs for ions which are heavier than the neutrals they interact with, is known as collisional cooling.

Major and Dehmelt showed that such collision should damp the secular motion. However, for a trap with a low density of neutrals the micro-motion is not very disturbed, remaining in proportion to the distance of the ion from the trap center. It therefore only decreases because the secular motion decreases due to the cooling [Maj68].

2.4.2 Evaporative cooling

The extent of the distribution of the ions in equilibrium, or in the process of reaching equilibrium, can reach the physical limits of the trap and some ions will hit its electrode. These ions will generally be lost from the trap. The ions removed by the collision with the electrodes are among the most energetic of the whole ion collection. Therefore the average energy of the ions in the collection is reduced by this process. This process is called "evaporative cooling". The evaporative cooling continues until the extent of the distribution that is beyond the physical extent of the trap is no longer significant.

2.4.3 rf heating

In Major and Dehmelt's model of the cooling of ions by collisions with neutrals in a Paul trap, the ions end up with zero velocity. This is because the neutrals are assumed to have zero velocity themselves. In such a case a collection of ions would

form a cold pool in which their space charge just balances the restraining forces of the psuedo-potential well. They showed that in such a case the ion density within this pool is uniform.

However, for a real cooling system using buffer gas, the ions must have at least the temperature of the buffer gas molecules. By how much their actual temperature will exceed the buffer gas temperature is a complicated matter of how the rf motions of the ions are dissipated. If the ions were at the same temperature as the buffer gas, then they would occupy a certain physical volume associated with the phase space volume of a collection at that temperature. However, in addition to the velocity associated with this thermal motion there would be the rf motion associated with the positions of the individual ions in space. This rf motion increases the kinetic energy of the ions, thereby causing them to be continuously exchanging this extra energy with the cooler buffer gas molecules. This process is called "rf heating" and always results in the ions having a higher temperature than that of the buffer gas.

With large collections of ions, the problem becomes more severe. For such collections, the space charge repulsion causes the ions to occupy a larger space, thereby increasing the rf motion of the ions in the outer regions. These hotter ions will transfer their energies to the cooler interior ions, resulting in an overall heating of the collection.

This aspect of the temperature achieved by buffer gas cooling in rf quadrupole fields was studies extensively by Lunney [Lun92]. who showed that the amount by which the temperature of an ion collection in a typical Paul trap exceeded that of the buffer gas grew with the 2/3rds power of the number of ions in the trap. It was speculated that this was due to physical size of the ion cloud growing in proportion to the cube root of the number of ions, in accordance with the Major and Dehmelt model of uniform collection density. Since the rf velocity of an ion is proportional to its distance from the trap center, the kinetic energy associated with this motion

will be proportional to the square of this distance. Thus the rf heating results in a temperature rise which is proportional to the average energy of the rf motion.

However, the exact relationship between the ion temperature and the average kinetic energy of the rf motion is difficult to determine analytically and experimental results are necessary to establish it. That relationship for the ions in a Paul trap was the primary purpose of the work of Lunney. The primary goal of the present thesis is to establish the same sort of relationship for an rf quadrupole ion guide.

Chapter 3

The Phase Space Distribution and Temperature of Ions in a RF Quadrupole Field

In the previous chapter, it was stated that the temperature of an ensemble of interacting particles in thermal equilibrium, together with the specifications of an applied force field and, of course, the total ion number, completely defines the particle density in phase space throughout the phase space volume of the collection. This ignores the possibility of chaotic phenomena, which can cause deviations from the statistical mechanics from which the statement is derived, but it should be noted that the statement does refer to an ensemble in thermal equilibrium and so such phenomena should be ignored. Whether chaotic phenomena can be ignored in an experimental system is usually best determined by comparing the results of a model based on thermal equilibrium with the actual behavior of the system. That is the aim of the present work, where the behavior of ions in a rf quadrupole ion guide is compared to that which can be predicted from a model based on thermal equilibrium.

The statement then immediately leads to the question of how, explicitly, the temperature determines the local phase space density.

3.1 Introduction

The relationship of the local phase space density to temperature is not obvious from the statistical definition of temperature due to Boltzmann, where it is defined in terms of the energy distribution of the particles. Specifically, in a system of N_o interacting particles sharing a total energy at temperature T, the number of particles dN that have energies in the interval dE is related to the particle energy E at which that interval is considered as follows;

$$\frac{dN}{dE} = \frac{N_o}{kT} e^{-\frac{E}{kT}} \tag{3.1}$$

where k is commonly referred to as "the Boltzmann constant".

Setting aside considerations of phase space for the moment, it is this form of the energy distribution that led to the concept that one could define a temperature for a collection of ions in a Paul trap. This is because a typical collection of such ions exhibited a gaussian distribution in space and velocity [Kni79][Hem92]. Such a distribution is expected for a collection of interacting particles in a simple harmonic potential well (see later in this chapter), and the widths of the distributions were used to derive temperatures.

However, this poses a conceptual problem for the motion of ions in an rf quadrupole field. This is because the motion, as shown in Chapter 2, has two distinct components; a macromotion which can be considered to be due to a simple harmonic pseudo potential well and is statistically distributed in amplitude and phase, and an rf motion which is coherent in that all particles move in phase with the rf and have a definite amplitude of motion related to their position in the trap. The energy associated with

the rf motion is therefore not statistically distributed and therefore should not be included in the definition of the temperature.

This problem can be probably best illustrated by considering the simple case of a collection of molecules moving at some central average velocity. As an illustration example consider the motion of a drink in a high-speed jet-liner. The whiskey molecules have a kinetic energy which is enhanced by the motion of the jet-liner so as to have a mean kinetic energy that would clearly allow them to melt the ice in the drink. This clearly does not happen because the ice is moving along with the drink. The "problem" is clearly resolved by considering only the velocities of the whiskey molecules relative to the centre of mass of the system.

However, it is important for what follows to note that it is the coherent center of mass velocity which is removed from the consideration of the motion before defining a temperature. Because kinetic energy is related to the square of this velocity, this is not equivalent to subtracting the kinetic energy associated with this velocity from the overall kinetic energies of the individual molecules.

While the removal of the coherent motion in the drink-in-jetliner case is very straightforward, it is not so for the coherent rf motion of ions in an rf quadrupole field. The analogy for the jet-liner drink would be that the whiskey is oscillating through the ice at a speed such that the increased kinetic energy of the whiskey molecules relative to the ice molecules would cause the ice to melt. This indeed happens in a Paul trap where the rf motion heats the buffer gas. It is only the very large heat capacity of the buffer gas relative to that of the ions that keeps the buffer gas at the temperature at which the trap is operated. It would seem therefore that the kinetic energy associated with the rf motion should be included in any definition of the temperature.

Yet the rf motion is coherent and therefore has no statistical distribution and therefore cannot be included in a definition of the temperature, temperature being a

purely statistical parameter.

3.2 Temperature and phase space

The conceptual problem involving temperature and energy distribution of ions in an rf quadrupole field is resolved by defining the temperature in terms of phase space, due to Gibb's and sometimes referred to as the Gibb's distribution. In this definition, temperature enters in the particle density distribution in the 6-dimensional phase space volume S according to

$$\frac{\partial^6 N}{\partial S} = Ae^{-\frac{E}{kT}} \tag{3.2}$$

where E is now the energy that particles have at the particular point in phase space under consideration and which is due to the energy that is statistically distributed throughout that phase space. The coefficient A is a normalization constant which results in the integration over the 6-dimensional phase space being simply the total number of particles.

In a system in which the motions in the three coordinates are independent, Gibb's relationship can be reduced to

$$\frac{\partial^2 N}{\partial S_\xi} = A_2 e^{-\frac{E}{kT}} \tag{3.3}$$

For a collection of particles in a pure simple harmonic potential well, the results are the same as that which can be deduced from the Boltzmann equation. However, for the case of motion in an rf quadrupole field, the phase space picture indicates clearly why the rf motion should be excluded, and indeed how to exclude it. This can be seen by considering the ion trajectories in phase space due to the rf motion compared to that for the statistically distributed macromotion within the simple

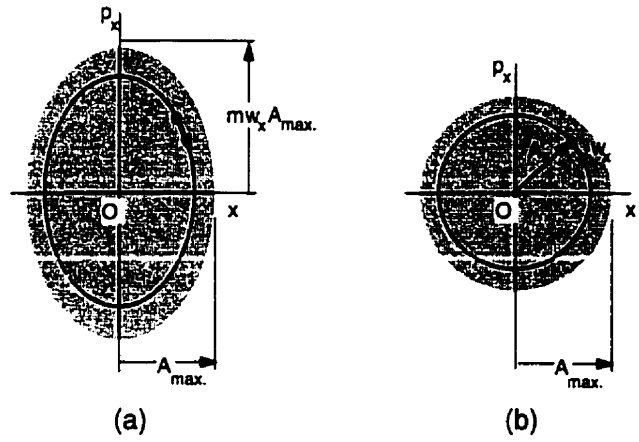

Figure 3.1: (a) The phase space diagram for simple harmonic motion with an arbitrary scaling of x and p_x and (b) with the scale in which the ellipse becomes a circle. The advantage of such a scaling is that in such a diagram the points representing the particles all rotate at the same uniform angular velocity; that of the simple harmonic oscillation itself.

harmonic pseudo-potential well. For this comparison first consider the action diagram for the macromotion.

3.2.1 The ellipse for simple harmonic motion

The action diagram trajectories of particles undergoing simple harmonic motion are ellipses centered at the origin, and whose axes are aligned with the momentum and displacement axes (Figure 3.1). A given collection of particles, all of the same mass, and all experiencing the same field, will all oscillate with the same frequency.

For the quadrupole beam guide, the macro-motion frequency is related with the trap operating conditions, a, q and Ω. To a good approximation within the stable range, the frequencies can be obtained from the expression

$$\omega_0 = \frac{\Omega}{2}\left[a - \frac{(a-1)q^2}{2(a-1)^2 - q^2} - \frac{(5a+7)q^4}{32(a-1)^3(a-4)} - \frac{(9a^2+58a+29)q^6}{64(a-1)^5(a-4)(a-9)}\right]^{\frac{1}{2}}. \tag{3.4}$$

(See ref. [Daw76] and references contained therein). For $a = 0$ and small q value, this equation converges to Eq.(2-19) of Chapter 2.

3.2.2 The action for rf motion

The rf motions, being essentially sinusoidal oscillations, will also result in ellipse-like trajectories in phase space. However, unlike the motions due to the simple harmonic pseudo-potential well, which at thermal equilibrium are assumed to be uniformly distributed over all phases, the rf motions of all the ions are in phase. Furthermore, as pointed out above the amplitude of the motion is proportional to the displacement from the trap center. The phase of the rf displacement differs by π to the phase of the rf itself, the maximum displacement occurring when the electric field is the most negative. The resulting trajectories in an action diagram are shown in Figure 3.2.

If the ions are distributed through all the possible displacements from the center, then the points representing all of these ions at the particular instant in time taken for Figure 3.2 form the solid line shown. Throughout an rf cycle this solid line will wobble about the displacement axis once every rf cycle but the action diagram of the whole collection at any instant in time remains a line. Therefore the rf motion has never any area to the action diagram.

Incidentally, the maximum momentum of the rf motion is related to the electric field at the center of this motion by

$$p_{\max} = \frac{eE}{\Omega} \tag{3.5}$$

where Ω is the rf oscillation frequency.

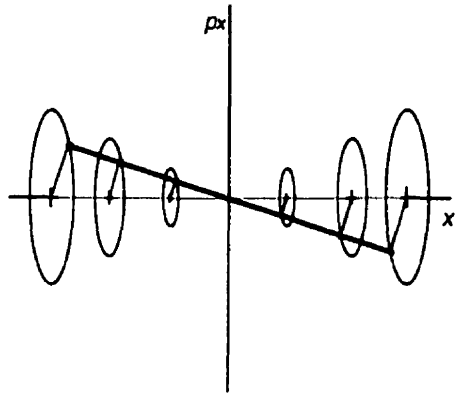

Figure 3.2: Phase space diagram for the rf motion in a quadrupole mass filter. The amplitude of the oscillation is proportional to the displacement of the ion from the central axis of the mass filter. The phase of the rf displacement is 180 degree relative to the rf phase.

Thus, higher electric fields result in taller ellipses while higher frequencies of oscillation result in shorter ellipses. On the other hand, the maximum displacement is related to the maximum momentum through

$$p_{\max} = m\Omega x_{\max}. \tag{3.6}$$

Thus the eccentricity of the ellipse, i.e. the ratio of maximum momentum to maximum displacement, is greater for higher masses and higher rf frequencies.

The fact that the action diagram of rf motion in an rf quadrupole field has no area means that the motions cannot be defined to have a density in phase space. It therefore cannot enter into the definition of temperature due to Gibb's. It therefore must be removed from the overall ion motion, just as a coherent movement in the center of mass of a collection must be removed, before a purely statistical definition

of the temperature can be achieved. The full action diagram of combined rf- and macro- motion must therefore be considered so as to discern how the rf motion can be removed.

3.2.3 Action diagram for combined SHM and RF motions

As shown in Chapter 2, the action diagram of the full motion of ions in an rf quadrupole field is an ellipse which is not generally aligned with the action diagram axis but which has a shape rotation. This can obviously be considered as a distortion of the right ellipse associated with the macromotion only. This distortion is also obviously due to the rf motion.

A consequence of the fact that the electric field producing this distortion is quadrupolar, and therefore does not couple the different coordinates of the motion, is that the distortion is merely a combined action of twisting and squeezing the old ellipse into a new ellipse of the same area. This area invariance is connected to the fact that the rf action diagram shown in Figure 3.2 is a straight line, and therefore has no area.

The actual degree of twist and squeeze both depend on the rf phase and q value. A method for determining this will now be presented.

RF distortion of the simple harmonic right ellipse

The rf distortion of the right ellipse of the action diagram of the macromotion can be expressed by a transformation matrix which has a determinant of unity:

$$\begin{pmatrix} x \\ p_x \end{pmatrix}_{Full} = M \begin{pmatrix} x \\ p_x \end{pmatrix}_{SHM} \tag{3.7}$$

The transformation matrix M will, of course, be different for each phase of the rf

for which the transformation is to be made. To determine the actual transformation from which this matrix can be extracted a procedure described by Dawson ([Daw76] p.28) can be used.

As an example of the procedure, the case when there is only an AC component to the field (i.e. $a = 0$) will be considered. This is the case most relevant to the rf quadrupole ion guide. The first step is to find the actual shape of the action ellipse at the particular phase of the rf that has been chosen. This can be obtained by using numerical integration to calculate the motion of an ion, with arbitrary initial displacement and momentum, in the actual field of the trap and plotting its displacement-momentum coordinates at that particular phase of the rf each time it recurs. The result, as the ion undergoes its precession due to the simple harmonic macromotion, is that the points will fall on different locations on the distorted simple harmonic ellipse associated with that particular phase. (See figure 3.3.) By continuing the calculation for long enough, the plotted points will eventually draw out the full ellipse.

The success of this procedure will depend on the simple harmonic motion not being an exact sub-multiple of the rf motion. Under these conditions, the plotted points will all fall on each other, the number of points on the diagram being just the number of rf oscillations that occur in one simple harmonic oscillation. If this situation occurs, then one can take the two values of q bracketing the offending value and interpolate the results.

The upright ellipse of the macromotion that corresponds to the action diagram calculated by the above procedure can be obtained by noting that its eccentricity is given by

$$\frac{p_{x_{\max SHM}}}{x_{\max SHM}} = m\omega_x \tag{3.8}$$

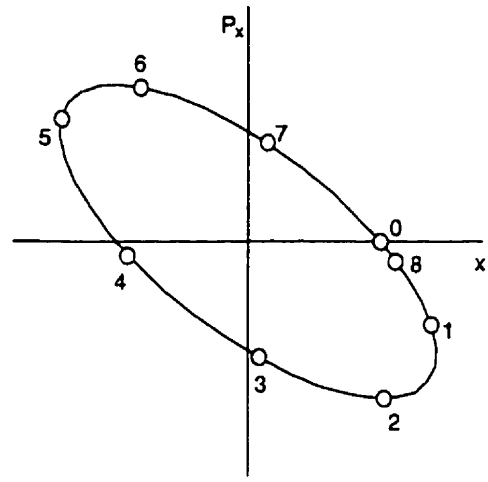

Figure 3.3: Points obtained by calculating the momentum-displacement coordinates for an ion in a quadrupole beam guide for a particular operating parameter q and plotting the results at the instants of 270 degree rf phase. The ion started at a positive displacement in x with zero momentum (point zero). The subsequent points are labeled 1 to 8. The simple harmonic oscillation is seen to take approximately 7.8 rf cycles.

and that its area is equal to that of the computed phase space ellipse;

$$\pi(p_{x_{\max SHM}} \times x_{\max SHM}) = Area\ of\ ellipse. \tag{3.9}$$

The simple harmonic frequency can be determined, with sufficient accuracy for the purpose of determining the phase space density distributions, from Eq. 3.4. Alternately, it could be obtained by noting the periodicity of the orbit of the particle points on the action ellipse plotted in Figure 3.3.

The area of the action ellipse can be obtained from its maxima and its intercepts with the axes (see Figure 3.4). Specifically, the area is given by

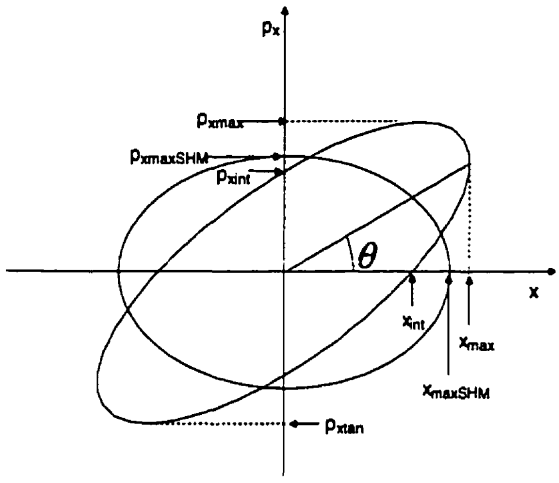

Figure 3.4: The rf distorted ellipse and and its associated SHM ellipse with their critical values.

$$Area = \pi(p_{x_{\max}} \times x_{int}) = \pi(x_{\max} \times p_{x_{int}}) \tag{3.10}$$

where the maxima and intercepts are defined in Figure 3.4. With Eqs. 3.8 and 3.9, this yields

$$x_{\max SHM} = \sqrt{\frac{p_{x_{\max}} x_{int}}{m\omega_x}} = \sqrt{\frac{p_{x_{int}} x_{\max}}{m\omega_x}} \tag{3.11}$$

whereupon $p_{x_{\max SHM}}$ can be obtained directly from 3.8.

In general, the transformation of the right ellipse of the macromotion into the actual ellipse of the full ion motion can be regarded as having two parts; an elongation of the ellipse along the displacement axis (accompanied by a squeeze along the momentum axis) and a twisting of the resulting ellipse to the proper inclination. The elongation is produced by a matrix of the form

$$\mathbf{M}_{elong} = \begin{pmatrix} \gamma & 0 \\ 0 & \frac{1}{\gamma} \end{pmatrix} \tag{3.12}$$

where γ is the factor by which the displacement axis is elongated. The twist is produced by a matrix of the form

$$\mathbf{M}_{twist} = \begin{pmatrix} 1 & 0 \\ \tan\theta & 1 \end{pmatrix} \tag{3.13}$$

where θ is the angle of the vector of the x extremum relative to the x axis. (In the example for the x motion shown in Figure 3.4 θ is positive.) The overall transformation from the simple harmonic motion ellipse to the actual action ellipse is then

$$\mathbf{M} = \mathbf{M}_{twist}\mathbf{M}_{elong} = \begin{pmatrix} \gamma & 0 \\ \gamma\tan\theta & \frac{1}{\gamma} \end{pmatrix}. \tag{3.14}$$

The factor γ is given by

$$\gamma = \frac{x_{\max}}{x_{\max SHM}} = \sqrt{m\omega_x \frac{x_{\max}}{p_{x_{int}}}}. \tag{3.15}$$

The twist angle is given by

$$\tan\theta = \frac{p_{x_{\tan}}}{x_{\max}}. \tag{3.16}$$

The value of $p_{x_{\tan}}$ could be determined directly from the plot of the action ellipse. However, it may be more accurate to calculate it from the more easily determined maxima and intercepts through the relationship, which may be derived from the fundamental properties of an ellipse;

$$p_{x_{int}} = \sqrt{\frac{x_{\max}}{x_{int}}\frac{p_{x_{\max}}}{p_{x_{int}}} - 1}. \tag{3.17}$$

The actual twist angle θ in the displayed action ellipse depends on the relative scaling of the momentum and displacement coordinates. To remove this dependence, and to achieve a twist angle factor that is dimensionless and relatively independent of the q value of the trapping field, it is convenient to define a twist parameter δ as

$$\delta = \frac{\tan\theta}{qm\Omega}. \tag{3.18}$$

Calculations were carried out to determine the action diagrams for a range of q values from 0.05 to 0.8. From these action diagrams the parameters γ and δ were determined as outlined above. The result showed that, to an accuracy of better than 1%, over this range of q values they could be approximated by the empirical equations (at 90° rf phase)

$$\gamma = 1 + 0.0033e^{\frac{q}{0.175}} \tag{3.19}$$

$$\delta = (0.5 + 0.33q^{2.5}) \tag{3.20}$$

With these parameters, the rf distorted ellipse at 90° rf phase can be calculated by means of a matrix transformation. The ellipse at different rf phases can be obtained by applying the transformation matrix, M(rf phase 1 →rf phase 2). The calculation of the transformation matrix M(rf phase 1 →rf phase 2) was discussed in Chapter 2.

The relations of γ and δ with q are found empirically. In fact, the transformation matrix from the simple harmonic motion to the rf distorted ellipse at a specific rf phase can be found for any arbitrary rf phase (in the above it was for 90° rf phase). The transformation to the 0° rf phase is simpler in that in involves only an elongation, but the elongation factor was found to be a complex function of q. Therefore the transformation to 90° rf phase was used in the present work.

A sample result of the general transformations are shown in Figure 3.5. This figure shows that the maximum x values of the rf distorted ellipses at 90° is close to

that of the simple harmonic ellipses for all q values and therefore, the transformation matrix from the simple harmonic distribution to a specific rf distorted distribution (M(SHM$\rightarrow$ 90° rf phase)) was formulated for the 90° rf phase.

The action ellipse of the macromotion has been named the "ellipse of the well model". Ironically, in most of the literature, that ellipse has been drawn larger than it should, in comparison with the rf distorted ellipses, [Mar89] and so the trajectory of Dehmelt's approximation was drawn with a larger amplitude than what is appropriate. Dehmelt's original suggestion was that the pseudo-potential well model can explain the macro-motion and its associated frequency but it was misunderstood by confusing the trap size and the maximum possible amplitude of the macromotion.

To establish the density distribution in the action diagram for the full motion of ions at thermal equilibrium in an rf quadrupole field, all that now remains is to determine the distribution in the macromotion ellipse. This distribution can then be deformed into the distribution for the full motion by simply applying the transformation matrices derived above for the shape distortions of the ellipses.

3.3 The ion distribution at thermal equilibrium in an rf quadrupole field

3.3.1 Ion distribution in simple harmonic motion

The ion density in the action diagram for a simple harmonic pseudo-potential well, which from the above is a right ellipse, can be expressed in the Gibb's formulation as:

$$\frac{\partial^2 N(x_\xi, p_\xi)}{\partial S_\xi} = A_2 \exp\left(-\frac{E(x_\xi, p_\xi)}{kT}\right), \tag{3.21}$$

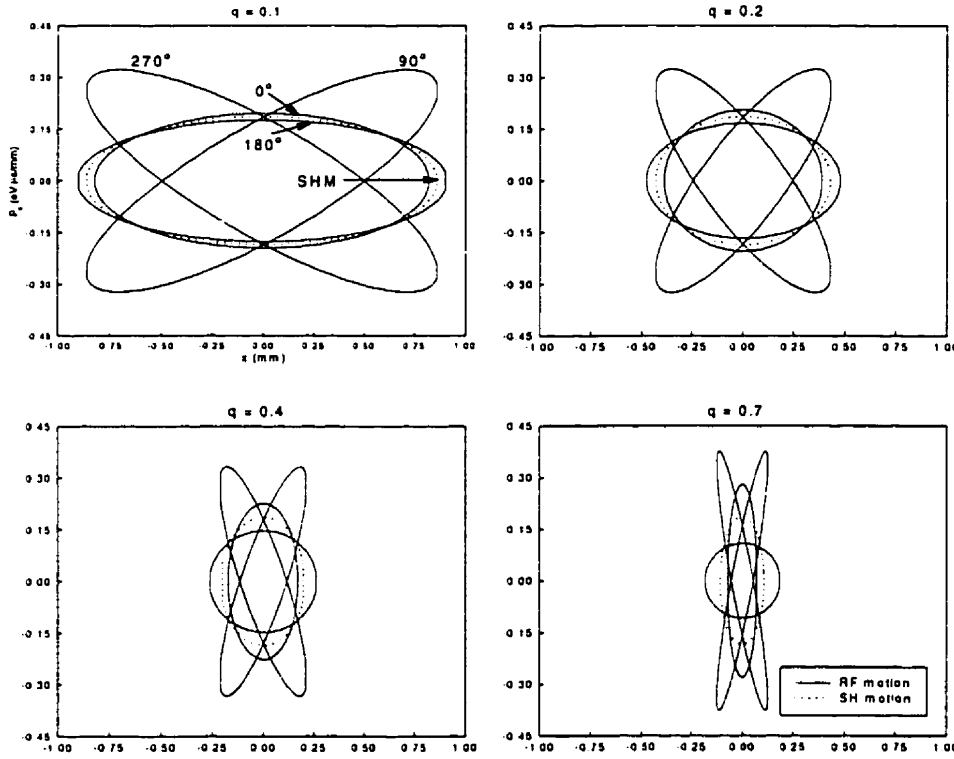

Figure 3.5: The equi-density ellipses (1σ) of simple harmonic potential with rf distorted ellipses at 0, 90, 180 and 270 rf phase angles for various q. The drawings with different q values are for a temperature of 0.025 eV.

where, as before, E is the total energy of an ion having the particular values of x_ξ and p_ξ, and T is the statistically defined temperature. For simple harmonic oscillations in the particular coordinate x, this is

$$E = \frac{p_x^2}{2m} + \frac{1}{2}m(\omega x)^2. \tag{3.22}$$

Then

$$\frac{\partial^2 N(x,p)}{\partial x \partial p_x} = A_2 \exp\left(-\frac{p_x^2}{2mkT} - \frac{m(\omega x)^2}{2kT}\right). \tag{3.23}$$

Integrating this distribution function over dx, gives the distribution in momentum which is

$$\frac{\partial N(x,p)}{\partial p_x} = A_2\sqrt{2\pi\frac{kT}{m}}\omega \exp\left(-\frac{p_x^2}{2mkT}\right). \tag{3.24}$$

Integrating the same distribution function over dp, gives the spatial distribution:

$$\frac{\partial N(x,p)}{\partial x} = A_2\sqrt{2\pi mkT} \exp\left(-\frac{m(\omega x)^2}{2kT}\right). \tag{3.25}$$

Doing a final integration of either of these distributions over the remaining coordinate gives

$$N_o = 2\pi\omega kT A_2. \tag{3.26}$$

The extent of these distributions can be characterized by the standard deviation σ. About 40% of the ion beam will be inside such an ellipse. The σ's for the SHM are related to temperature by

$$\sigma_x = \frac{1}{\omega}\sqrt{\frac{kT}{m}} \tag{3.27}$$

and

$$\sigma_{p_x} = \sqrt{mkT}. \tag{3.28}$$

The physical significance of these parameters is that they correspond to an amplitude of oscillation at which the energy is $(1/2)kT$.

The significance of evaporative cooling introduced in Chapter 2 can now be seen. In principle, the extent of the particle points in an action diagram with a Gaussian density distribution is limitless. In a real trap, the motion will extend to the physical limits of the trap. Ions that have energies such that their motions can lead to collisions with the trap electrodes will generally be lost from the trap. The random collisions between ions that lead to thermal equilibrium will always result in some ions reaching this high energy. The continuous removal of such high energy ions from the trap therefore leads to a lowering of the temperature of the ion collection. However, if there is continuous heating of the ions so that they continue to have the same temperature at equilibrium, then more ions will be pumped up to where they will intersect with the electrodes. Thus the evaporative cooling becomes a continuous evaporative loss, the rate of which this happens depends on the number of ions in the trap, the fraction of those ions that have energies sufficient to leave the trap and diffusion process associated with the progress to thermal equilibrium.

In estimating the effective size of an ion beam, it is useful to note the fraction of the collection that is within a particular values of displacement or momentum expressed in units of σ. Thus an ellipse corresponding to one sigma would encompass about 40% of the particles, an ellipse of two sigma about 87% and an ellipse of three sigma about 99% (Figure 3.6).

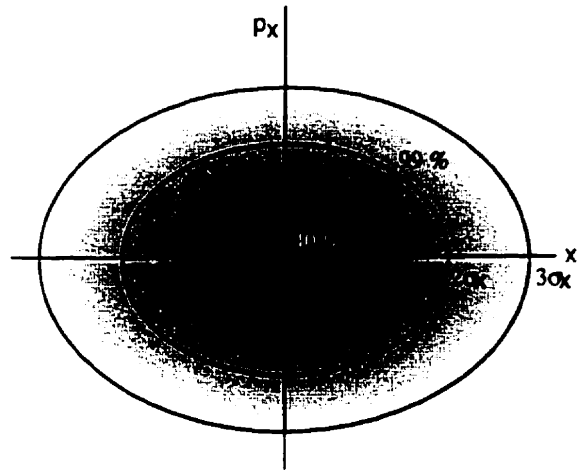

Figure 3.6: The distribution of particles in a simple harmonic potential in thermal equilibrium at temperature T.

3.3.2 σ_x and σ_{v_x} as functions of the rf phase

The transformations M(SHM→ 90° rf phase) and M(rf phase 1 →rf phase 2) are linear for both the displacement and momentum axes. Therefore the transformations conserve the Gaussian shape, but change the spread of the distributions in both space and momentum. For the Gaussian distribution, the standard deviation contains all of the necessary information needed to describe the distribution. The standard deviation in the simple harmonic potential at a given temperature can be calculated from the relations Eqs. 3.27 and 3.28.

The rf distorted equi-density ellipses for various values of q were shown in Figure 3.5. The sizes of ellipses were determined from the temperature of ions and from the pseudo-potential well depth. From the diagrams, the standard deviation of the gaussians for space and momentum can be deduced for the full motion including the rf motion. The results, in units of the standard deviations for the macromotion alone

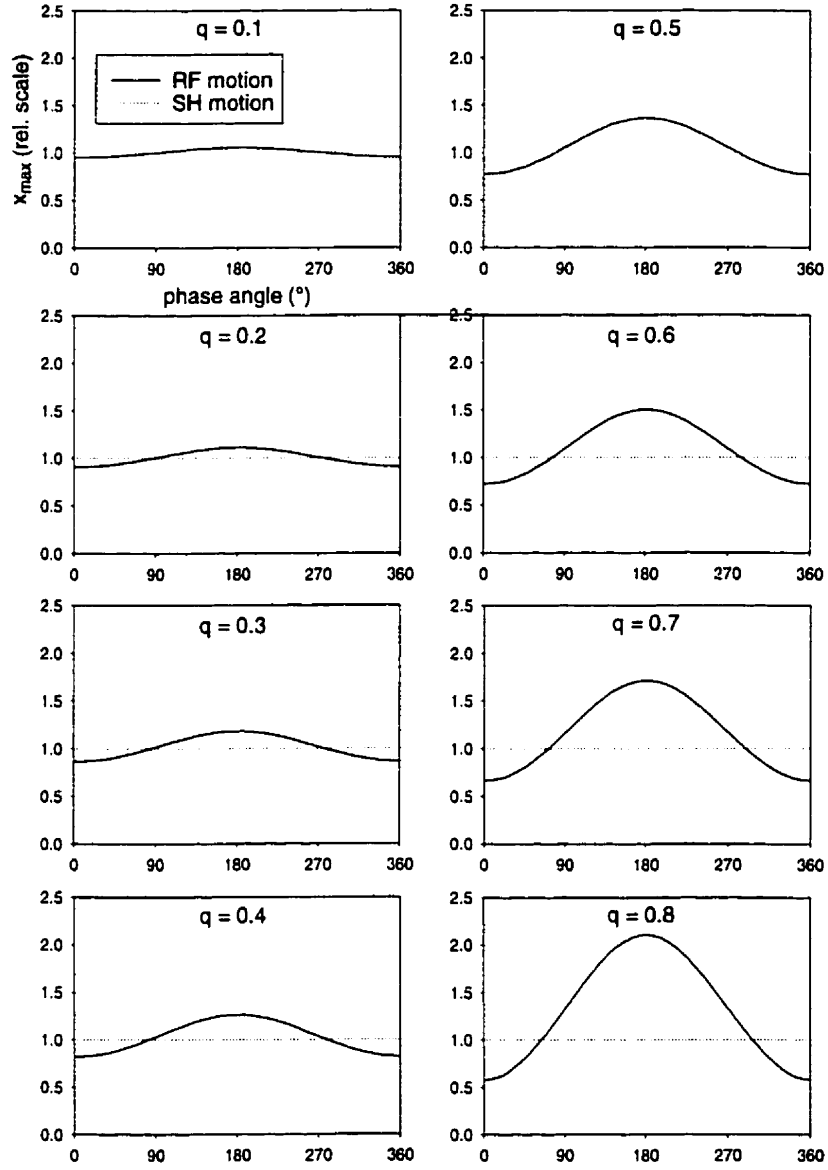

Figure 3.7: The sigma x as function of rf phase for various q.

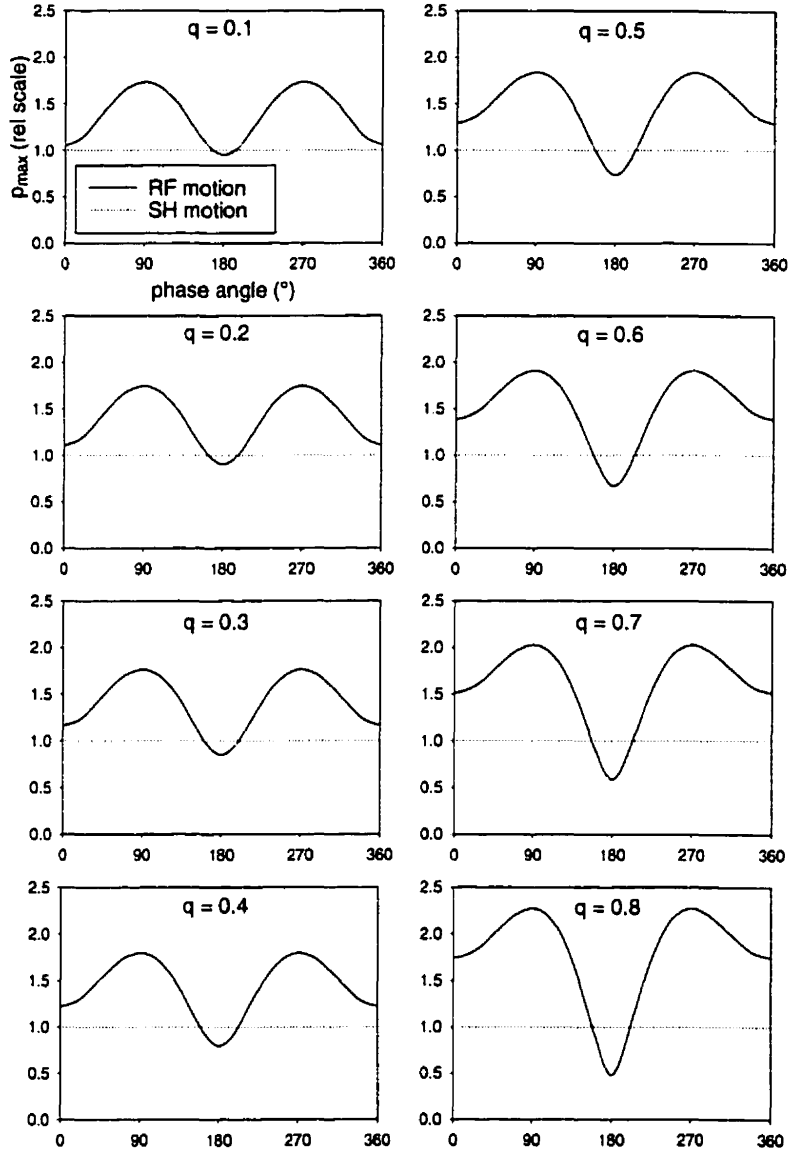

Figure 3.8: The sigma p as function of rf phase for various q.

are shown in Figures 3.7 and 3.8 as functions of the rf phase angle for various q values ranging from 0.1 to 0.8. From these figures the velocity and spatial distributions in the actual trap can be calculated for any ion temperature.

3.4 Comparison with other temperature definitions

As pointed out in the introduction to this chapter, the observation of gaussian distributions in space and momentum for the ions a Paul trap led to the description of this distribution by a temperature. However, other than in the work of Lunney on ions extracted from a Paul trap[Lun92], these temperatures were not defined as in the present work.

A temperature based on the Boltzmann distribution in a pseudo-potential well (T_{SHM}) was used by Knight [Kni79]. He determined a temperature, which will be referred to here as T_{SHM}, from the observed spatial distribution. It can be seen in Figure 3.7 that, due to the micromotion, this temperature will be different than that defined in the present work, which will be referred to as T_{SHM}^{mod} .

Vedel et al [Ved83, Ved95] used what they referred to as a temporal invariance model that took into account the periodic variations in the distributions due to the rf motion. They defined what they called a pseudo-temperature (T_{pseudo}) based on the experimental observation of the Gaussian distribution of the ions in a trap [Sch79] and taking into account these periodic variations. That temperature was based on the standard deviation of the velocity. For an ion cloud in a Paul trap, they defined temperature as

$$3k_bT/m = \sigma_{vx}^2 + \sigma_{vy}^2 + \sigma_{vz}^2 \tag{3.29}$$

where the $\sigma_v's$ are the rf averaged standard deviations of the instantaneous velocity components which are oscillating at the rf frequency. However, they started from a

gaussian distribution function described by

$$f_{xx'} = K \exp\left[-\left(\frac{(x_0^2+y_0^2)}{2\sigma_{sx0}^2} + \frac{(\dot{x}_0^2+\dot{y}_0^2)}{2\sigma_{vx0}^2} + \frac{z_0^2}{\sigma_{sz0}^2} + \frac{\dot{z}_0^2}{\sigma_{vz0}^2}\right)\right] \tag{3.30}$$

where K is a normalization factor and $\sigma_{sx0}, \sigma_{sz0}, \sigma_{vx0}, \sigma_{vz0}$ are the spatial and velocity dispersions. The distribution function was defined not from a specific statistical distribution at a given temperature, but from the experimentally observed gaussian distribution. The original paper mentioned that the ion cloud has a gaussian distribution, but it gave no data or information to support the accuracy of that statement.

A chemical thermometer using the reaction rate of a specific ion/molecule has also been used to determine the temperature of trapped ions ($T_{chem.}$) [Law76, Bas90, Nou90]. The measured reaction rate in the trap was compared to known rates for different thermal conditions outside the trap and the temperature was determined. The reaction rate is a function of the relative velocities of the ions with respect to the neutral molecules. Again the velocity distribution of the ions was assumed to be gaussian for a given temperature and thus $T_{chem.}$ becomes equivalent to T_{pseudo}.

It can be seen that these alternative definitions of temperature will give different temperature values for the same ion motion distribution. The three, including the one used in the present work, are presented in Table 3.1.

A comparison of calculated values of temperatures T_{SHM} and T_{pseudo} for various values of q from the phase space distributions that can be derived from the T_{SHM}^{mod} of this work is shown in Figure 3.9. This shows that at low values of q, T_{SHM} is similar to T_{SHM}^{mod} but T_{pseudo} is twice T_{SHM}^{mod}. This is indicated in Figure 3.5, which shows that the spatial spread is almost the same as that of the simple harmonic ellipse for all phases, but that the momentum spread is noticeably higher than that of the simple harmonic ellipses at some rf phases.

The divergence of the other temperatures from that of this work is even greater for

Temp.	Definition (Assumptions)	Reference
T_{SHM}	Ions in a pseudo-potential	[Kni79]
T_{pseudo}	Ions are in Gaussian distribution and the distribution changes with rf oscillation	[Ved83, Ved95, Law76] [Bas90, Nou90]
T_{SHM}^{mod}	Ions in thermal equilibrium in pseudopotential and the distribution is deformed by rf motion	[Lun92, Moh96] this study

Table 3.1: The temperature definitions for the ions in a trap.

higher values of q, where the rf motion becomes more significant. Thus it is clear that if temperatures are estimated without correcting for the rf distortion, the temperature deduced from the spatial distribution will be different from the temperature deduced from momentum distribution, and both will be different from that which is based directly on statistical mechanics.

This is not to say that the temperature T_{SHM}^{mod} is more useful than the others in interpreting the result of experiments such as those involving ion-molecular collisions or those involving ion interactions with lasers. What is often needed is, in fact, the actual spatial distribution of the ions or their energy distributions included the rf motion and in such experiments the non-statistical definitions of temperatures may indeed be of more immediate use.

However, the point that should be emphasized here is that, because these other temperature definitions are not completely statistical, they do not lead to an accurate description of the local phase space density of the ion collection. Therefore they cannot be used to simulate the results of a given experiment by integrating the contributions of the ions over the phase space that they occupy.

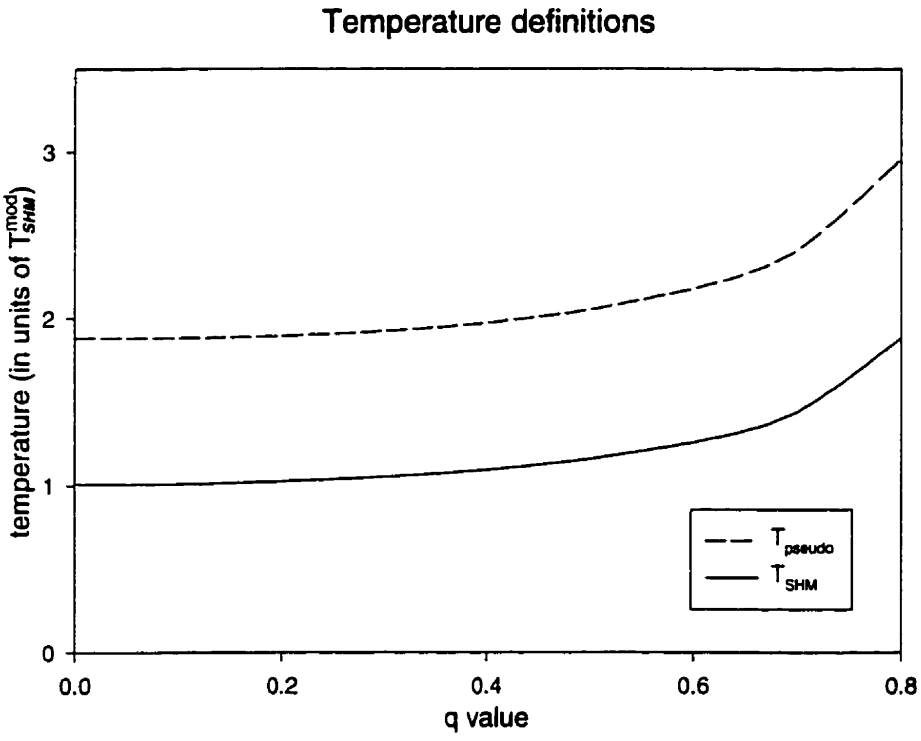

Figure 3.9: The differently defined temperatures vs q for a temperature 1 in T^{mod}_{SHM}.

3.5 Testing the assumptions of the definition of T^{mod}_{SHM}

The basic assumption used to define the temperature T^{mod}_{SHM} is:

If there are no disturbances by the cooling mechanism, the thermal equilibrium distribution of the ions in a quadrupole trap is that of a simple harmonic motion in the pseudo-potential with an added rf distortion.

This assumption was checked by a Monte Carlo simulation (see Chapter 5). A

collection of ions representing an ion beam was introduced into an rf quadrupole ion guide and its interactions with the buffer gas molecules was simulated from the known ion-molecule cross sections. After these collisions had resulted in thermal equilibrium, the action diagrams of the collection at various rf phases were extracted. Figure 3.10 shows the equilibrium distributions of 4,000 ions at different rf phases. The equi-density lines of the 4000 ions are not smooth enough to compare their evolution with the evolution of the ellipses predicted by the assumption. Thus the evolution of the standard deviation of the position and momentum (σ_x and σ_{p_x}) were compared with the evolutions of those predicted by the assumption. It was also verified that the x and p distributions were gaussian for 20 different rf phases. Figures 3.11 and 3.12 show that the evolution of the configuration of the ions calculated by the simulation agrees well with that predicted by the assumption and the agreement is best for low q values and low buffer gas pressures. From this it is concluded that at thermal equilibrium the ion distribution in a trap can be represented as a thermal equilibrium distribution in the simple harmonic pseudo-potential well with added rf distortion.

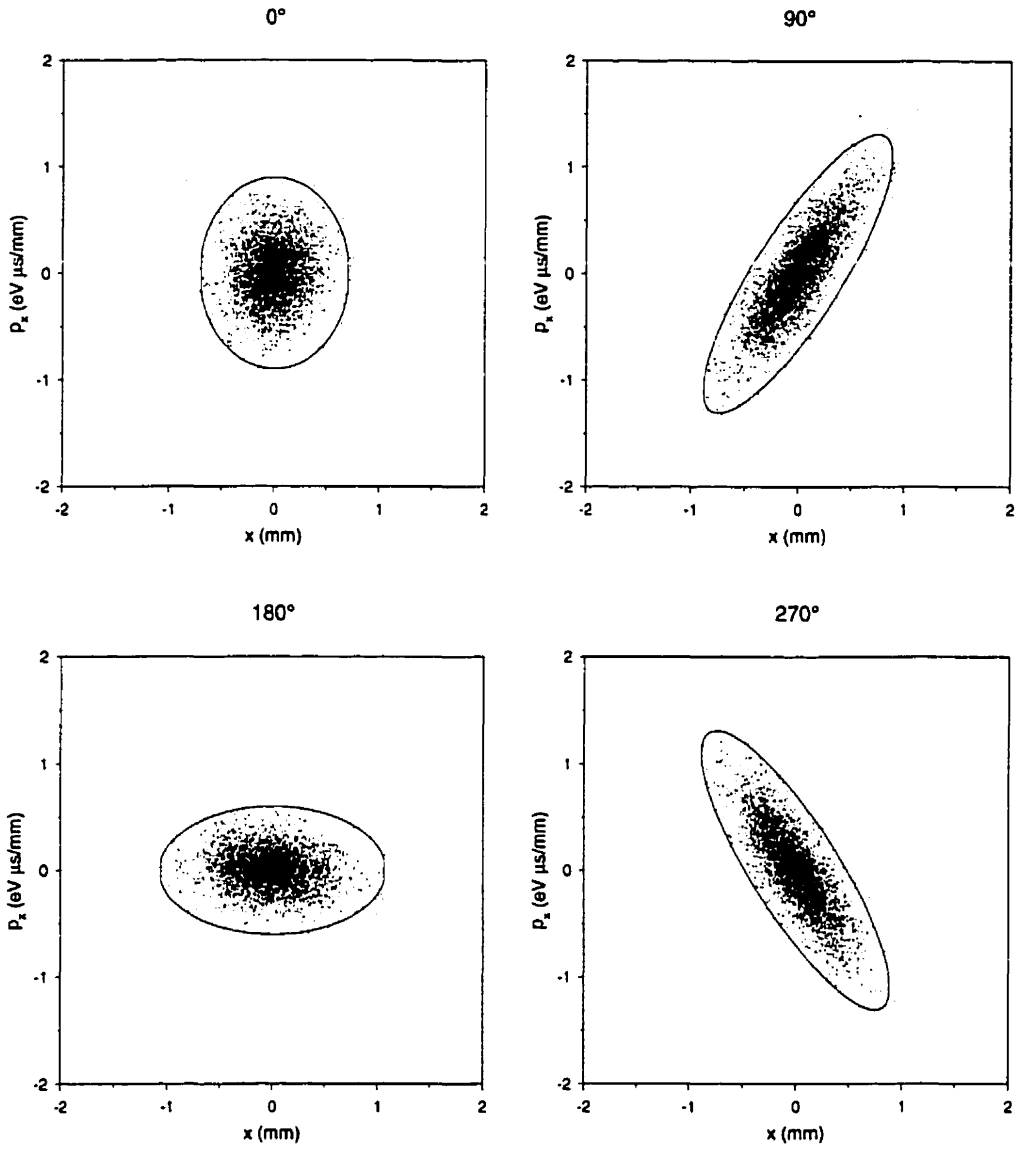

Figure 3.10: The phase space evolution of a simulated ion beam. Cesium ion beam reached thermal equilibrium by nitrogen molecular collisions in an axial field quadrupole at $\Omega/2\pi$ =700 kHz, q=0.4 and 8 Pa buffer gas pressure.

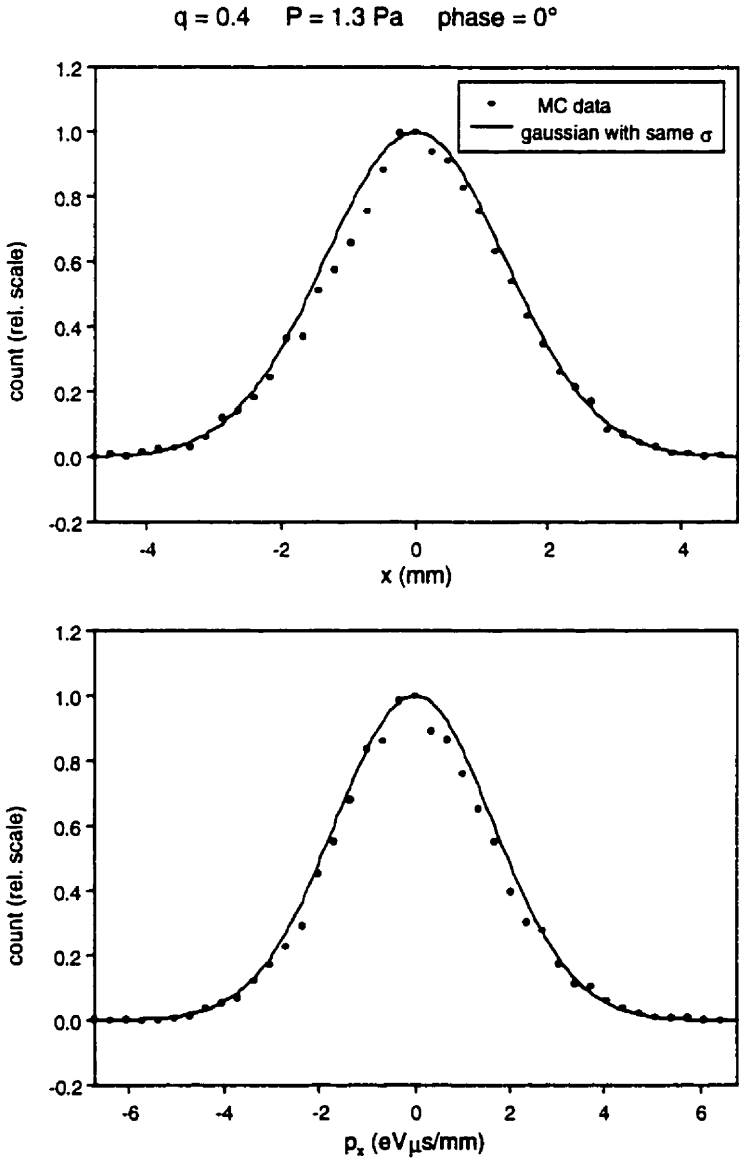

Figure 3.11: The spatial and momentum distributions at a specific rf phase (0 degree) with a Gaussian with same standard deviation.

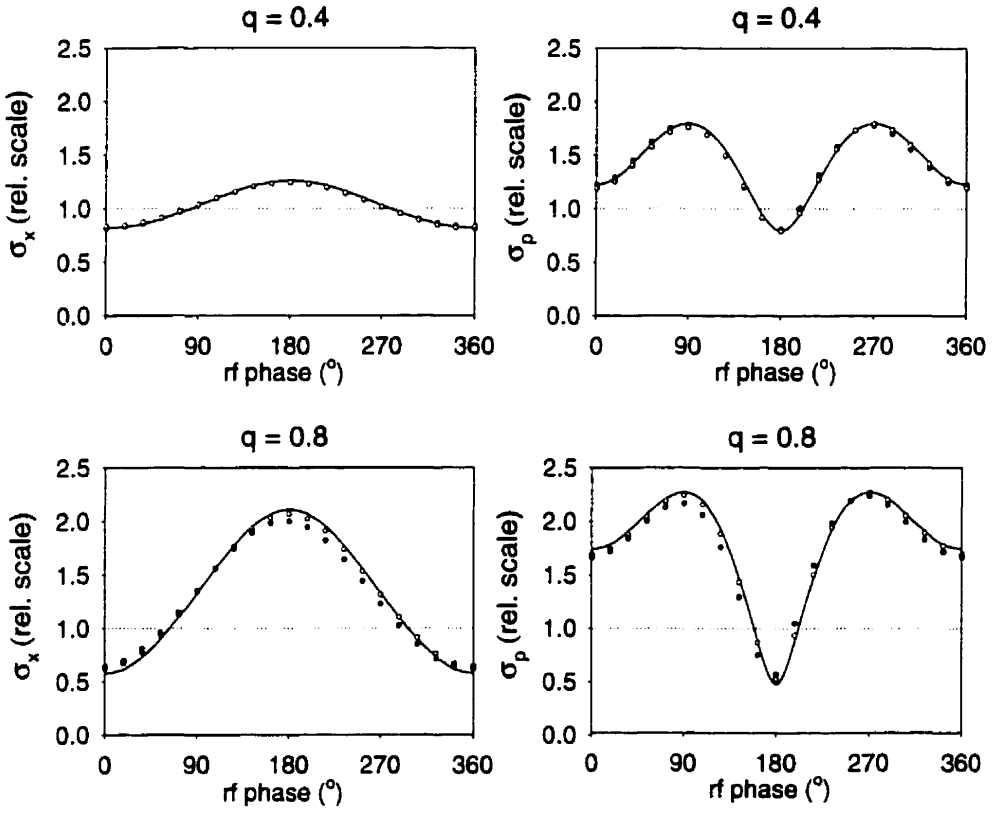

Figure 3.12: The standard deviations x and p of simulated beams in a thermal equilibrium as functions of rf phase (empty circle:1.3 Pa, filled circle: 8 Pa, solid line: prediction by the assumption).

Chapter 4

Experimental System

The experimental system consists of an ion source which injects ions into an rf quadrupole ion guide with buffer gas and an axial electric field, and a detector which observes the ion beam which is extracted from the ion guide (Figure 4.1). The rf quadrupole ion guide is mounted in its own chamber containing the buffer gas and is connected to the ion source through an orifice, and the detector through a miniature quadrupole ion guide. Since the ion source and the detector must be at a higher vacuum than the ion guide, the ion guide chamber is mounted inside a large vacuum chamber so that the buffer gas which bleeds out through the orifice and through the miniature quadrupole can be pumped away.

The ions from the ion source enter the ion guide and experience cooling as well as a guiding force toward the detector. The transmission as well as the ion distribution of the cooled beam, the temperature and the drift time were all measured as functions of the pressure, the quadrupole driving conditions, the rf frequency, the rf amplitude and the axial field strength.

To measure the ion distribution of the cooled beam in the quadrupole field of the miniature quadrupole, the ions were extracted from it by means of a DC electric field.

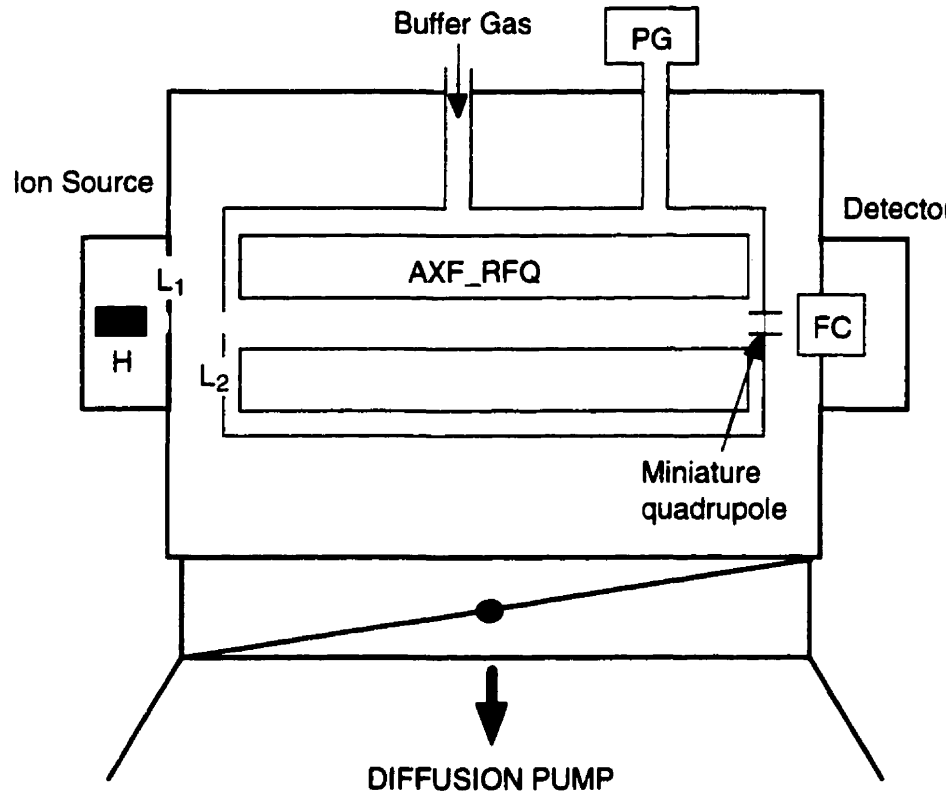

Figure 4.1: The schematics of the experimental setup.

The ions experience a fringing field and a DC extraction field during the extraction such that the detected distribution was deformed and the original distribution at the quadrupole had to be determined by deconvoluting this deformation from the beam distribution at the detector. A computer program (RFQ_EXT) was developed to accomplish this.

As described in the previous chapter, the ion distribution in the ion guide can be understood as a Boltzmann distribution in a pseudo-potential well with an rf distortion. The ion spatial distribution was measured for a much longer time interval than the period of the rf oscillation so that the measured distribution is an average over many rf cycles. The distribution for each rf phase is a gaussian with a different standard deviation for that phase and the time averaged distribution is the average of all of these gaussians. To determine the ion beam temperature, the different spatial distributions for 20 different rf phases were superimposed and the results compared with experimental data. A least square fitting program (Temp_Fit) was used to compare the constructed distributions with the data. The ion beam temperature was established by adjusting the assumed ion temperature until a good agreement was achieved.

4.1 Design of the experimental setup

To design the ion guide with buffer gas cooling, the following factors were considered.

1. *Breakdown voltage.* The breakdown voltage at the buffer gas pressure used is much lower than that for high vacuum. This had to be taken into account in order to achieve the maximum possible potential on the rods forming the ion guide.

2. *Injection energy should be less than a few tenths of an eV.* To prevent secondary ionization, the injection energy that will bring the ions to the buffer gas region should be less than the second ionization energy. To use the buffer gas cooling system, the relatively high energy ion beams from the source should be decelerated using a DC electric field, but the study of this deceleration process is not included in this thesis. (If the system described here were to be used with high-mass bio-molecules, the injection energy should be less than 10 eV to prevent dissociation.)

3. *Optimal buffer gas pressure.* Finding the optimal buffer gas pressure is a subject in itself. The mobility calculation mentioned in the next subsection can be used as a first approach to solving this problem. The optimal pressure is related to the ion mobility, the injection energy, and the choice of rod length. These relationships were investigated by simulation as well as by experiment. The optimal buffer gas pressure is also related with the breakdown voltage and the pumping requirements for various pressures.

4. *Pumping requirements.* The pumping system must be designed by taking into account the gas flow conductivity of the vacuum separation and the buffer gas pressure that must be achieved for satisfactory performance of the ion guide.

The technical considerations determining the optimal buffer gas pressure will now be presented.

4.2 Optimal pressure - Mobility calculations

It is possible to gain much insight into the motion of ions which are involved in collisions with buffer gas molecules by considering these interactions as forming a

viscous drag, as it is in the case of ion mobility studies. Even though such a treatment cannot account for stochastic effects which affect the transmission efficiency and the cooled beam size, the mobility approximation of the collisions as a viscous drag makes it possible to carry out many analytical studies. For example, the expansion of the stability diagram for motion in an rf quadrupole field [Whe74] and the axial velocity and axial energy decay constants [Moh96] have been studied. By analogy with damped simple harmonic motion, the decay time constant of the macro-motion amplitude was also calculated in the present work.

Of most importance here, the trajectories calculated from treating the effect of ion-buffer gas collisions as a simple viscous drag give some indication of the optimal cooling pressure and of the increase in the value of q for which the ion motion is stable in the ion guide structure. Before considering the subject of viscous drag associated with ion mobility, the effect of a viscous drag on the Mathieu equations will be presented.

The Mathieu equation of motion including a viscous drag term is

$$\frac{d^2u}{d\xi^2} + 2k\frac{du}{d\xi} + (a_u - 2q_u \cos 2\xi)u = 0, \tag{4.1}$$

where u represents either x or y, $\xi = \Omega t/2$, $k = \frac{K}{m\omega}$ (the mobility K is defined below) and the parameters a and q have the same definitions as in Chapter 2. The second term of the equation is the drag term caused by the buffer gas. By making the substitution $u = u_1 e^{-k\xi}$, the equation becomes

$$\frac{d^2u_1}{d\xi^2} + (\overline{a_u} - 2q_u \cos 2\xi)u_1 \tag{4.2}$$

where $\overline{a_u} = a - k^2$. Thus one returns to the Mathieu equation but now with a solution that involves the term $e^{(\mu-k)}$. Practically, u approaches $e^{(\mu-k)}$ as ξ goes to infinity. So the stable region is expanded all the way to $\mu = k$.

4.2.1 Definition of the mobility

If the number density of ions is low enough to ignore the Coulomb force of repulsion, then we need to consider only two kinds of ion motion: diffusion and drift. The diffusion disperses the ions through the gas. It creates a net flow of ions along the gradient of their relative concentration. If a weak uniform electric field is applied through the gas, a steady flow of ions along the electric field lines will also develop, superimposed on the much faster random motion that leads to diffusion. The velocity of the center of mass of the ion cloud is called the drift velocity $\mathbf{v}_d$, and this velocity is directly proportional to the electric field intensity $\mathbf{E}$, provided that the field is kept weak. Thus

$$\mathbf{v}_d = K\mathbf{E}, \tag{4.3}$$

where the constant of proportionality K is called the *mobility of the ions*; K is a joint property of the ions and the gas through which the motion occurs. This relationship is valid only when the electric field is so weak that the ions are close to being in thermal equilibrium with the gas molecules, that is to say, when "low-field" conditions prevail. Under these conditions the ionic distribution is almost Maxwellian. The ionic motion is a result of its random walk through the gas, resulting in a slow drift in the direction of the applied field.

The mobility of a given ion species in a given gas is inversely proportional to the number density of the gas molecules and is relatively insensitive to small changes in the gas temperature (e.g. of a few degrees Celsius), if the number density is held constant. To facilitate the comparison and the use of the data, a measured mobility K is usually converted to a "standard", or "reduced " mobility (mobility at room temperature and atmospheric pressure) K_o, defined by the equation

$$K_o = \frac{p}{760}\frac{273.15}{T}K = \frac{p_o}{760}K, \tag{4.4}$$

where p is the gas pressure in torr and T is the gas temperature in Kelvin at which the mobility K was obtained, and p_o is the "standard pressure", normalized to $0°C$ and defined by the equation

$$p_o = \frac{273.15}{T}p. \tag{4.5}$$

4.2.2 The axial velocity and energy decay time constant

When an ion is released in a weak electric field, it will accelerate and finally reach a uniform drift velocity. Its motion will be similar to that of an object projected through a resistive medium. From the mechanical analogy, we can derive the decay constants of its motion. When the electric force and the frictional force which originates from the collisions with the buffer gas molecule, are balanced, the ions will have a drift velocity and thus

$$Frictional\ force = eE{=}e\frac{v_d}{K}. \tag{4.6}$$

This frictional force is always present, even in the absence of an electric field. It results from only the ion motion. In the absence of an electric field it therefore damps the ion motion according to

$$\frac{dv}{dt} = -\frac{e}{mK}v. \tag{4.7}$$

so, the time constant for the velocity decay is

$$\tau_v = \frac{mK}{e}, \tag{4.8}$$

and the associated time constant of the energy decay is

$$\tau_E = \frac{mK}{2e}. \tag{4.9}$$

Considering a particle projected in a resistive medium with an initial velocity v_0. The equation of motion is

$$m\frac{d^2u}{dt^2} + b\frac{du}{dt} = 0, \tag{4.10}$$

The velocity is

$$v = v_0 e^{-\frac{b}{m}t}, \tag{4.11}$$

and the velocity decay time constant is

$$\tau_v = \frac{m}{b}. \tag{4.12}$$

Comparing Eqs. 4.8 and 4.12, the relationship of the mobility K to the drag force constant b can be obtained;

$$b = \frac{e}{K}. \tag{4.13}$$

4.2.3 Macro-motion amplitude decay time constant

If the micro-motion is neglected, the ion motion in an rf quadrupole field can be expressed as a SHM in a pseudo-potential well. When the buffer gas is present, the macro-motion decreases. If the rf motion is neglected, the equation of motion with the damping term becomes

$$m\frac{d^2u}{dt^2} + b\frac{du}{dt} + ku = 0 \tag{4.14}$$

which can be written as

$$\frac{d^2u}{dt^2} + 2\beta\frac{du}{dt} + \omega_o^2 u = 0, \tag{4.15}$$

where $\beta \equiv b/2m$ is the damping parameter and ω_o is the angular frequency of the macro motion. From Chapter 2, ω_0 is

$$\omega_o \simeq \frac{q}{2\sqrt{2}}\Omega \quad (\text{for } q \leq 0.5). \tag{4.16}$$

The mobility K is related to β by (from 4.13)

$$\beta = \frac{b}{2m} = \frac{e}{2mK}. \tag{4.17}$$

The critical damping condition is $\beta^2 = \omega_o^2$, which results in

$$K = \frac{\Omega r_o^2}{\sqrt{2}V} \tag{4.18}$$

$$= \frac{\sqrt{2}e}{mq\Omega}. \tag{4.19}$$

4.2.4 The macro-motion amplitude damping constant for under damping

For the underdamped case ($\beta^2 < \omega_o^2$), the solution of the equation of motion is

$$u(t) = Ae^{-\beta t}\cos(\omega_1 t - \delta). \tag{4.20}$$

The damping time constant is

$$\tau_A = \frac{1}{\beta} = \frac{2mK}{e} \tag{4.21}$$

which is proportional to the mobility, and therefore inversely proportional to pressure. These analytically derived damping constants agree well with the values derived from trajectory calculations using mobility with the real trap potential and buffer gas (c.f. Chapter 6)

The amplitude decay constant τ_A is twice the velocity decay time constant τ_v. For the axial field quadrupole cooling system, the amplitude decay constant is related to the radial macro-motion amplitude and the velocity decay time constant is related to the axial motion. The optimal cooling condition of the AXF_RFQ cooling system should satisfy the radial and the axial cooling conditions.

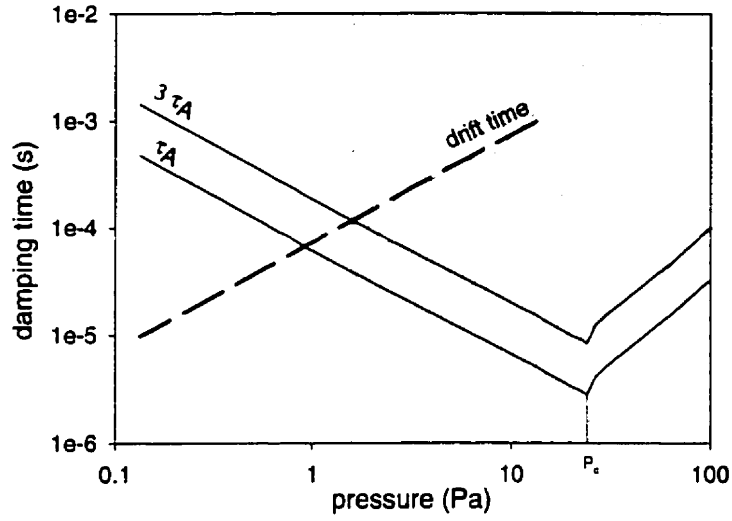

Figure 4.2: A graphical method to determine the optimal buffer gas pressure for cesium ions in nitrogen buffer gas. The hatched region shows a sufficient pressure range for buffer gas cooling.

4.2.5 A practical method to determine the optimal buffer gas pressure

Consider a simple case in which the particles' initial axial velocities are small, so that only the decay of the radial motion is important. The decay time constant is proportional to the mobility and it is inversely proportional to the pressure. The drift time (or cooling time) is

$$\begin{aligned} \Delta t &= \frac{L}{v} \\ &= \frac{L}{KE_{ax}} \end{aligned} \tag{4.22}$$

where L is the AXF_RFQ length and E_{ax} is the axial field strength in the AXF_RFQ. The drift time is inversely proportional to the mobility and is proportional to the pres-

sure. If the pressure is not sufficiently high, the ions will emerge from the quadrupole ion guide without sufficient cooling. If the intended cooled macro-motion amplitude (A_{cooled}) is related with the initial amplitude of the ions' macro-motion (A_0) by

$$A_{cooled} = A_0 e^{-a\tau_A} , \tag{4.23}$$

then the time needed for that amplitude decay will be $a\tau_A$. Thus the condition of sufficient cooling is $\Delta t \geq a\tau_A$ and that condition can be found by a graphical method (see Figure 4.2). By drawing τ_A vs P and Δt vs P the pressure range satisfying $\Delta t \geq a\tau_A$, where a is the decay factor can be determined. For the case with high initial ion velocity, the same method can be used but the drift time will not be a linear function of the pressure.

4.3 Vacuum system

As pointed out above, the system needs a constant supply of buffer gas because the detector and the ion source need to be operated in a high vacuum and the buffer gas in the rf quadrupole ion guide leaks out into this vacuum system through the connecting ports. Therefore a high throughput vacuum system was used. The system was pumped by a 12 inch diffusion pump (CVC PVMS-1000A, 5300L/s), backed by two mechanical pumps (Alcatel type 2015 and 2021, 10.6 CFM and 14.6 CFM). The diffusion pump was connected directly to the vacuum chamber, which is a 300 mm cylinder. The pressure of the main chamber was monitored by a CVC GPH-320C Penning vacuum gauge, calibrated for the buffer gas. The pressure in the main chamber was lower than 10^{-2} Pa in all of the experiments and was 1 to 4×10^{-3} Pa for the ion temperature measurements.

4.4 The ion source

The cooling system was first tried with a gas discharge type ion source. This attempt was not successful because the buffer gas went into the ion source and became ionized. We could not produce pure ions and therefore either a pre-filter was needed or the source had to be run in a high vacuum.

Surface ionization type alkali ion sources were chosen to study the buffer gas cooling system because these sources have the following advantages:

1. The produced ions do not interact with the buffer gas because the ionization energy of an alkali atom is generally lower than that of a buffer gas atom.

2. The produced ions have adequate purity and therefore, do not require the pre-filter.

3. The source does not need differential pumping and its construction is relatively simple.

4. As pointed out in Chapter 2, collisional focusing requires that the mass of the ions should be greater than that of the buffer gas molecules and it is easy to find an alkali ion whose mass is larger than that of the buffer gas molecules (which are nitrogen for this thesis).

5. The mobility of the alkali ions in many different gases are well documented, and the published mobility data can be used to check the reliability of the simulations.

The detailed principles behind the surface ionization source can be found in several references [Val77]. The following is a quick overview of the theory.

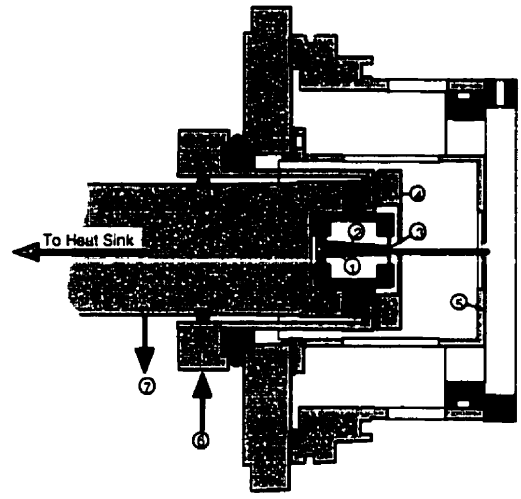

Figure 4.3: Cross-sectional diagram of the surface ionization ion sourc.

Atoms or molecules incident on hot metal surfaces leave the surface either as neutral particles or as positive or negative ions [Kin23, Ive23]. This process is called surface ionization. The ionization can be characterized by its degree of ionization α :

$$\alpha = \frac{n_i}{n_a} \tag{4.24}$$

where n_i and n_a are the numbers of ions and atoms leaving the surface, respectively. In the equilibrium state, the number of incident atoms is equal to the sum of the numbers of ions and atoms leaving the surface.

For positive ions, the value of α varies with the surface temperature T, the ionization potential E^i of the incident atoms or molecules, the work function φ of the ionizing surface and the electric field E which causes the ions emerging from the surface to leave the surface. For the simple case in which there is no electric field, the degree of ionization can be formulated by [Kin24]

$$\alpha = A \exp\left[\frac{Z_i(\varphi - E^i)}{kT}\right] \tag{4.25}$$

where $A = \frac{g_i}{g_a}$ is the statistical weight ratio of the ionic to the atomic state of the particles leaving the surface (in the case of alkali metals $g_i = 1$ and $g_a = 2$), Z_i is the charge of the ions and k is the Boltzmann constant. For the case with an electric field the argument of the exponent includes more terms. Equation 4.25 shows that the degree of ionization increases with the work function of the ionizing surface and that it decreases when the ionization energy rises. Lower temperatures give a higher degree of ionization, but the release rate of the atoms from the aluminosilicate is also dependent upon the temperature and if the temperature is too low, the atoms will not leave the ionizing surface.

In this study, platinum was chosen as the surface material, because it has a high work function (φ =5.32 eV) and cesium was chosen as the sample ion, because it has the lowest ionization energy (E^i =3.89 eV) as well as a higher mass than that of the buffer gas. A commercial molecular sieve (Varian VACSOBB) with its cations replaced (by ion exchange) with cesium cations, was used as an ion source. The detailed theory of cation exchange of aluminosilicates can be found in reference [Bre74].

A directly heated cylinder contains and heats the sample material and the platinum wire which provide the ionizing surface. This heating cylinder was made from Inconel 601HF which has a high electric resistivity, a high melting point and relatively good machining properties. Both a DC power supply and an AC power supply were tested to power the ion source. The heating power was 30-45W (about 0.5V, 60 - 90A). A diagram of the ion source is shown in Figure 4.3.

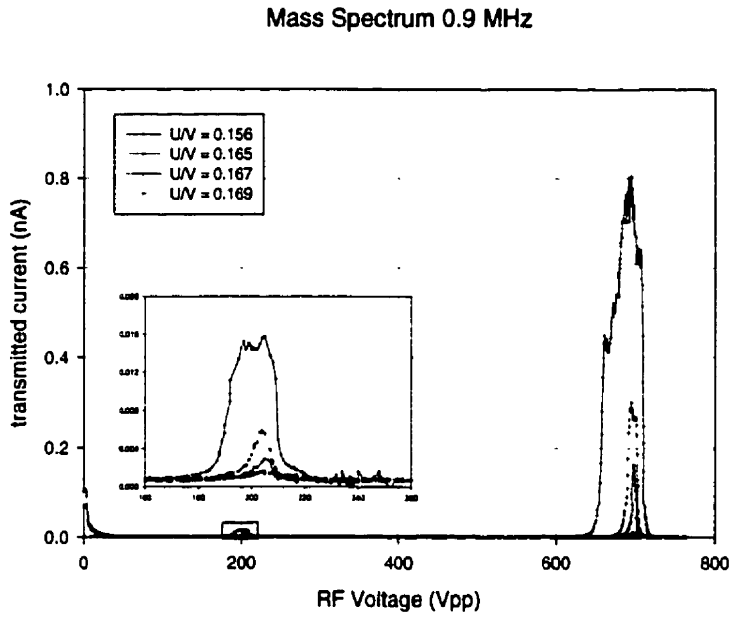

Figure 4.4: The mass spectrum of the ion source. The higher value of U/V corresponds to the higher resolutio.

4.4.1 The Beam Purity

To detect the possible exchange of ionization between the cesium ions and the buffer gas or with possible impurities in the buffer gas, the ion beam purity was determined with the quadrupole mass filter with and without buffer gas cooling. Figure 4.4 shows the measured mass spectrum without buffer gas cooling. The spectrum shows that the ion beam contains a trace of potassium. The spectrum of the cooled beam is similar except that it does not contain the potassium ion peak. It is suggested that the collisional cooling is less effective for the lower mass potassium, but a detailed experiment on this subject was not attempted in this research. Ions other than cesium were not detected and this confirms that there is no ionization exchange between the

cesium ion and the buffer gas or the impurities of the buffer gas.

4.4.2 The Current Stability

With the 30-45W of heating power (about 0.5V, 60 - 90A), the attainable ion current after the entrance lens (L_2) was a few nA. With one charge of cesium zeolite, the source produced cesium ions without a significant current change for more than one month at about 8 hours operation a day. For the transmission and the temperature measurement, the short time stability was important and during these experiments, the maximum current fluctuation was $\pm 5\%$ of the measured current.

4.5 The Collisional Cell

The collisional cell is enclosed by a 183 mm long, 70 mm diameter cylinder with two end caps: the entrance and exit lenses. It contains the quadrupole rod structure and it is used to maintain the buffer gas around the quadrupole structure. The quadrupole rod structure and its electric driving circuit are shown in Figure 4.5. The 183mm quadrupole rod consists of 36 identical pieces which are each separated by a 0.1 mm thick mira film. The pieces of each rod were connected by a resistive- network DC potential divider. The diameter of the rods is 15.9 mm and the closest distance between opposite rods is 13.8 mm. The electric driving method used here is similar to the driving condition of a conventional quadrupole mass filter. The quadrupole has different DC biases for its front and exit ends although it has the same rf voltage throughout. The whole quadrupole assembly was floated to provide the bias between the cooling system and the detector which is grounded.

To calculate the fringing and DC axial fields, an electric field calculation program (RELAX_3D) was developed that was based on a 3-D relaxation which uses the

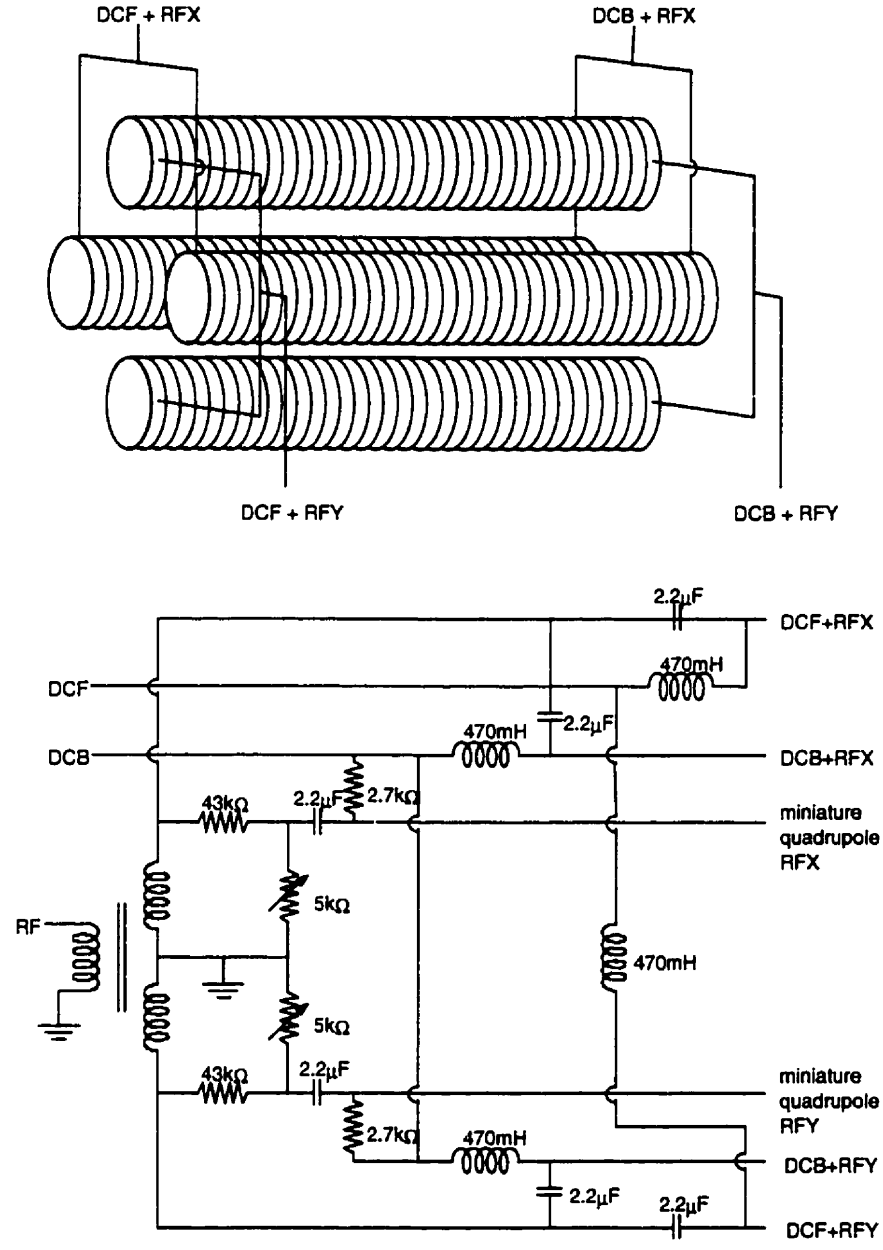

Figure 4.5: The axial field radio frequency quadrupole (AXF_RFQ) ion beam guide and its driving circuit.

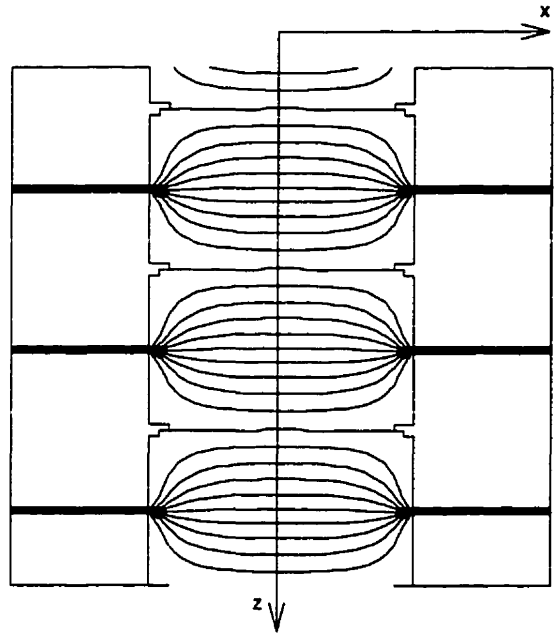

Figure 4.6: The contour plot of the DC potential in x-z plane.

techniques of over relaxation and variable grid steps. The 3-D relaxation result for the axial field quadrupole (AXF_RFQ) shows that the gradient inside the rod structure is relatively smooth. (see Figure 4.6)

Two end cap lenses enclose the cylindrical quadrupole housing. The front cap is a diaphragm with a 1 *mm* diameter hole. Two different interfaces, a skimmer type and a miniature quadrupole interface are used as exits, each for a different purpose. The skimmer type exit lens was adapted to minimize the fringing field effect and has a high transmission. A miniature quadrupole interface was developed to guide the cooled ion beam from the main quadrupole field at buffer gas pressure to the high vacuum while maintaining the full quadrupole field. The guided ion beam was extracted from the quadrupole field to a rotating Faraday plate for the measurement

of the beam profile.

In commercial API/MS systems, nitrogen is used as a curtain gas which covers the orifice to the vacuum chamber, through which the ions enter, and rejects the other gases to remove contamination from the sample. Therefore nitrogen enters the gas cooling system naturally and is used as the buffer gas in the API/MS system. Hence nitrogen was chosen as the buffer gas for this research. The nitrogen (99.998 % purity) buffer gas was fed through a needle valve and the pressure was monitored by a manometer (MKS BARATON model:626A, 1 Torr ($1.33\times10^2\,Pa$) full range).

4.6 Detector

Several techniques have been used to measure the distribution and temperature of the collections of ions. Those methods are summerized in Table 4.1. Three methods use a laser to measure the beam distribution and the spectral line width of ion clouds in a trap, one method uses chemical reaction rates and two other methods measure the phase space and spatial distributions of the extracted ion cloud or ion beam.

The laser methods can be applied to specific ions with an excitation energy corresponding to the laser's wave length and are not appropriate for the cesium ions used in this research. Tomography by photodissociation and chemical reaction rate measurement methods need a more detailed chemical background and are not directly related with the phase space distribution with which the temperature was defined.

On the other hand, the time of flight method is only applicable to Paul traps. The AXF_RFQ beam guide operates at much higher buffer gas pressure than the Paul trap or the Paul trap cooling system, and the ions experience more collisions. If the ion beam were to be extracted directly from the quadrupole beam guide, one would lose, due to gas collisions, the information of the original configuration in the

Method	Trap used	Measured quantity	Reference
Laser Induced Fluorescence (LIF)	Paul trap	average spatial distribution of ion cloud	[Kni79, Sch81]
Tomography by Photo-dissociation	Paul trap	average spatial distribution of ion cloud	[Hem92]
Doppler Shift of LIF	Paul trap	spectral line width due to Doppler effect	[Sie88, Zha95]
Chemical Reaction Rate	Paul trap	chemical reaction as a function of time	[Law76, Ved92] [Nou90]
Ion Cloud Extraction and Time of Flight	Paul trap	extracted and projected phase space distribution	[Lun92-1, Ved95] [Moh96]
Extracted Beam Profile	quadrupole beam guide	average spatial distribution of ion beam	this study

Table 4.1: The method of temperature measurement of trapped ions

ion guide. Therefore an extracted beam profile measurement system and method was developed to measure the beam size and temperature. To avoid buffer gas collisions during the extraction process, a miniature quadrupole ion beam guide was designed.

4.6.1 Miniature quadrupole beam guide

The miniature quadrupole holder serves as a vacuum separation and one end of it is inserted into the main quadrupole of the ion guide and the other end is in the high vacuum (see Figure 4.7). The miniature quadrupole was operated with a fraction of the rf amplitude of the main cooling guide so that the quadrupole field continues smoothly to the high vacuum side. Also, due to exit slots between the miniature quadrupole electrodes, the pressure decreases smoothly within the quadrupole. Thus the cooled ions can be guided into the high vacuum while still remaining in the full quadrupole field. Once they are in high vacuum, the ions can be extracted to the detector without suffering further buffer gas collisions. Of course, the ions experience the rf fringing and DC extraction fields and the detected beam profile is different from the beam profile in the quadrupole field. The evolution of the beam profile can be calculated and the original configuration can be determined, because ion optics in a high vacuum is straightforward. Figure 4.7 shows the miniature quadrupole beam guide.

Detector-Faraday cup

To determine the detector type, the following factors were considered.

1. The experiment is done in a relatively low vacuum and the detector should be operated in a relatively high vacuum.

2. The beam current ranges from a few hundred pico-amperes to a few nano-amperes.

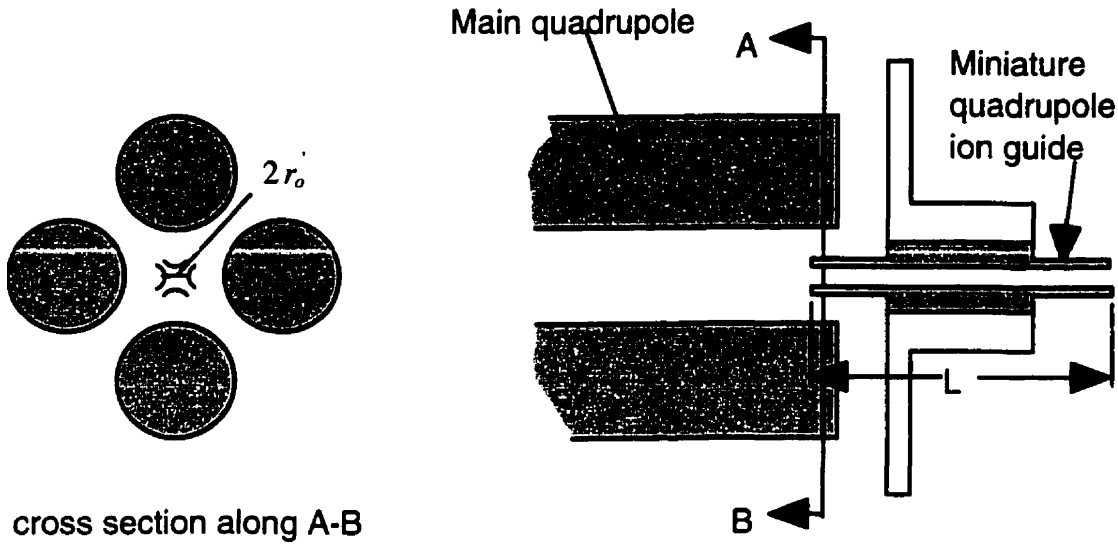

Figure 4.7: The miniature quadrupole ion beam guide ($r_o' = 1.75\ mm$, $L = 40\ mm$) interfaces the collisional cell and the high vacuum chamber. It extends the quadrupole field to the high vacuum chamber.

3. The required response time is a 1/100th of the cooling time (0.01 ms) for drift time and cooling time measurements.

A combination of a Faraday cup detector and a current amplifier, or pico-ammeter, satisfies the above considerations and was adapted to the experiment. Two types of detectors were used to measure the current and to determine the beam profile. A stationary Faraday cup was used to measure the ion current, and a rotating Faraday plate was used to measure the beam profile.

To measure the incoming ion current into the beam guide, the electrodes of the beam guide and the exit lens were also used as detectors. In the experiment, two different types of current meters, a KEITHLEY 614 electrometer and a KEITHLEY 485 pico-ammeter, were used to monitor the beam current. The 485 pico-ammeter was influenced by the rf induced current and therefore the transmitted current was measured with the 614 electrometer. The current injected into the beam guide was measured by disconnecting the quadrupole power supply and connecting the four rods together with the exit lens electrically and measuring the current from the rods to ground. In this configuration almost no current reached the detector.

4.6.2 Beam profiler

To measure the beam profile inside the miniature quadrupole, both a rotating detector (see Figure 4.8) and a computer program were developed. The ion detector assembly consists of a pair of semi-circular Faraday plates mounted on a rotating plastic flange. The semi-circular Faraday plates are separated from one another by 0.1 mm. The ion current on one Faraday plate was monitored with a pico-ammeter and the ion current on the other Faraday plate was amplified (by $10^7\ V/A$) by a current amplifier and was sent to the oscilloscope for measurement. The entire detector assembly is rotating (1-10 rpm) around an axis that is centered 14 mm off the central axis of the cooling system. The rotation speed was determined by measuring the time taken to complete one rotation, and the rotation period was constant up to a 1% error. The ion current at each of the two Faraday plates was measured as a function of the angular displacement of the rotating detector. The ratio of the two currents versus the angular displacement was recorded and the angular displacement was converted into a linear displacement relative to the beam's central axis.

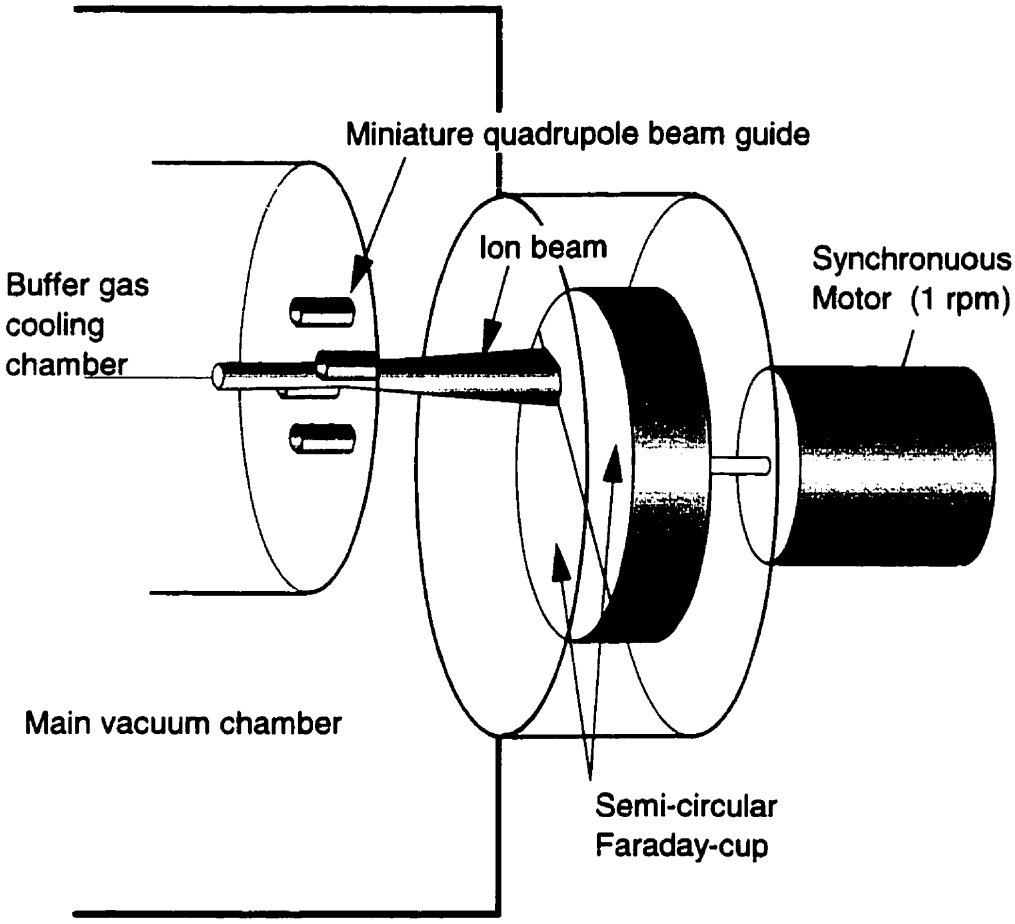

Figure 4.8: Detector assembly consisting of a miniature quadrupole ion beam guide and a rotating beam profiler

The cooled ion beam was extracted by means of an extracting electric field produced by the potential difference between the miniature quadrupole and the detector plates. The distance from the end of the miniature quadrupole to the detector was 9 mm. Data was collected with a Macintosh Quadra 630 computer interfaced to the Keithley 485 picoammeter through an IEEE 488-SCSI controller or by a LeCroy 9310M Oscilloscope connected to a Keithley 428 current amplifier.

Noise reduction - Determination of the filtering rise time

The detected ion current signal was noisy and at low currents, the noise was even larger than the signal. To correct this, two noise reduction methods were used. In one, the current was amplified and the high frequency noise was suppressed by the amplifier's built in rise time filter function. The beam diameter was of the order of 1 mm and the linear "cutting" speed of the detector at the position of the beam was 2.2 mm/s. The beam cutting time was about 500 ms for the whole beam cross-section and therefore the filtering rise time of the amplifier should be chosen to be considerably shorter than the beam cutting time. In the experiment, the rise time of the noise was between 3 and 10 ms, so the filtering action was set to a filter rise time of 10 ms. With the rise time filtering, the noise was reduced by 70 %. In the other method, the random noise was reduced by averaging the signals. For the beam profile measurement, 20 scans were averaged using the oscilloscope's built in function.

4.7 Simulation of the ion beam extraction from the quadrupole rods

During the extraction process, the ion beam experiences confining and diverging forces caused by the rf quadrupole and extracting fields. The beam profile measured at the detector is not a copy of the beam profile inside the full quadrupole field so

a computer simulation was developed to relate these two beam profiles. To measure the distribution of the ions inside the quadrupole, the ions were extracted from the quadrupole field and were projected onto a perpendicular plane where the rotating Faraday cup measured the beam's lateral distribution.

The simulation program calculates the ion beam envelop's evolution. The ion beam that is extracted is an average over continuously changing rf phases, but in the computer simulation, the beam is approximated by a set of discrete starting rf phases. The 20 equally spaced phases were chosen as starting rf phases. For each starting rf phase, the starting ellipse was found by applying the transformation matrices M(SHM $\rightarrow$ 90° rf phase) and M(rf phase 1 $\rightarrow$ rf phase 2) to the simple harmonic ellipse. The program calculates the evolutions of the starting ellipses by using the following procedure.

1. Find the ellipse representing the 1σ distribution in phase space for the simple harmonic pseudo-potential well for a specific temperature T_s, from Eqs. (3.27) and (3.28).

2. Find the rf distorted ellipse of the 90° rf phase with the transformation matrix $M(SHM \rightarrow 90° rf\ phase)$ (eqn.2.0) and find the rf distorted ellipses for the 20 other rf phase by applying the transformation matrix $M(rf\ phase1 \rightarrow rf\ phase2)$. These rf distorted ellipses are the starting ellipses for the next transformation. The choice of the initial rf phase (90 deg.) was explained in chapter 3.

3. For each time step, find out the transformation matrix (see chapter 3) for the current rf potential since the rf potential can be treated as constant for small time steps (staircase approximation).

4. For each step also find the transformation matrix for the radial component of

the extraction potential (refer to formula); the radial component was calculated by a near field approximation from the axial potential.

5. Applying the transformation matrices of steps 3 and 4 to the phase space ellipse, find the transformed ellipses (by the rf and radial components of extraction field).

6. Now calculate the axial displacement of the ellipses by the axial component of extraction field.

7. Find out maximum displacement of each ellipse, which is the beam envelop at the axial position calculated in step 6. (Figure 4.9 shows the evolution of the beam envelops).

8. Repeat the procedures of steps 3 to 7 until the ellipses reach the detector.

9. Construct the beam distribution at the detector for a given initial $\sigma's$ for T_s by adding the final spatial distributions of the 20 different phases.

10. Determine the temperature from the beam profile at the detector by comparing the experimental and the simulated distributions. If the constructed distribution is narrower or broader than the experimental data, we can find a constant (k) that must multiply $\sigma'_{\text{det}}s$ so that the constructed distribution agrees with the experimental distribution. From the relation $\sigma \propto \sqrt{T}$ (refer Eq. 3.27), the temperature can be calculated as $\sqrt{k}T_s$.

These steps have been summarized in Figure 4.10.

The program (RFQ_EXT) has been coded in an Excel spreadsheet. The time step was taken to be 1/20 of the period of an rf oscillation and 20 initial rf phases were used. The starting axial position was at a point where an axial energy of 2eV had already been gained from the extraction electric field. At that point, the quadrupole field was

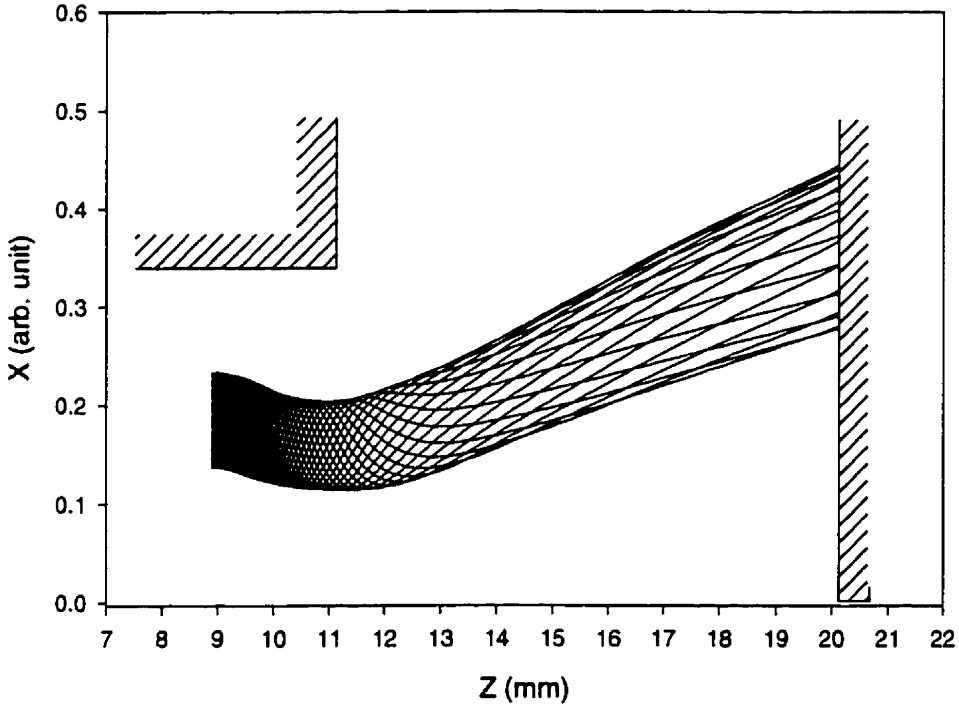

Figure 4.9: A typical result of the RFQ_EXT simulation. Each trajectory represents the evolution of the maximum position of the ellipse for each phase, starting within the full quadrupole field. The hatched objects represent one rod and the detector.

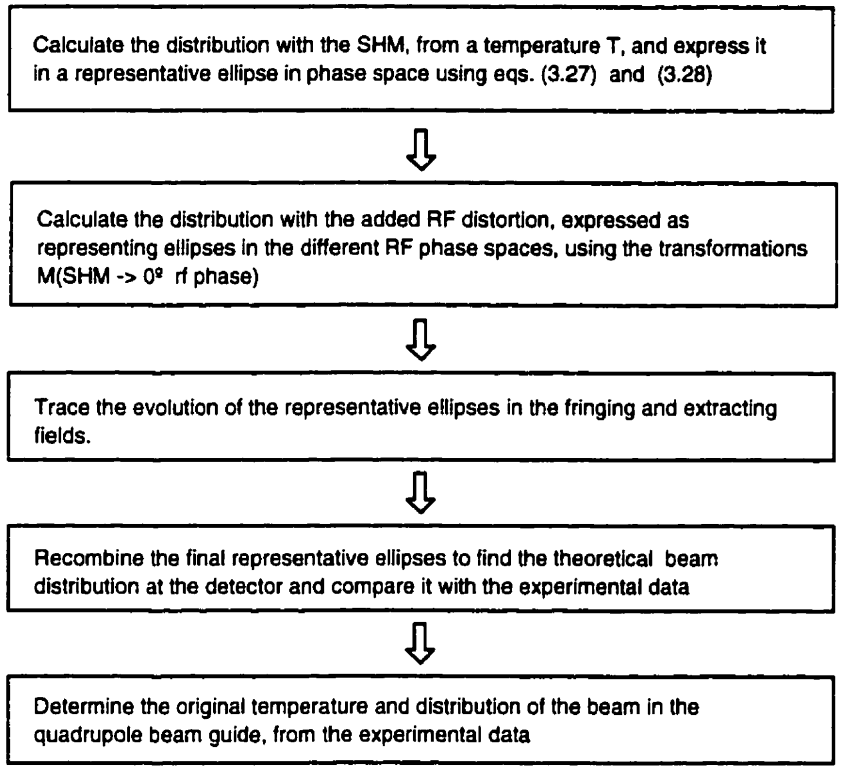

Figure 4.10: Outline of the determination of temperature.

not very attenuated. For one starting rf phase, the calculation took a few seconds and the whole calculation took a few minutes on a Pentium 133 MHz personal computer. The calculation speed is one example of the benefit of phase space dynamics. The rf fringing field and the DC extraction field used in this simulation were obtained by using a near-axis approximation (discussed below). A similar calculation using a Monte Carlo simulation with 10,000 particles takes about a day with a Pentium Pro 200 MHz PC system.

4.7.1 RF fringing field and DC extraction field implementation

rf fringing field

The rf fringing field was calculated using a 3-D relaxation program (3D_RELAX). This calculated fringing field was implemented in the RFQ_EXT program as a mathematical function. The function was derived with some assumptions: (1) the fringing field has no axial component, and (2) the quadrupole component is dominant and the other components are negligible. The quadrupole fringing field as a function of the axial displacement is shown in Figure 4.11 (a).

The extraction electric field

To extract the ions from the quadrupole beam guide, an electric field was applied by applying a potential difference between the miniature quadrupole guide and the detector. The electric field caused by this difference is referred to as the extraction field. The extraction field was implemented as having two orthogonal components, the radial and the axial components, in the RFQ_EXT simulation.

The radial component of the extraction electric field was derived from the potential along the quadrupole's axis by the near field approximation. If the electric field along the axis is $E(z)$, then there will be a radial component of the field near the axis given by the divergence equation, as described in Chapter 2:

$$E_r(r,z) \simeq -\frac{1}{2} r \frac{\partial E(z)}{\partial z}. \tag{4.26}$$

Therefore,

$$\frac{\partial^2 \phi}{\partial x^2} = -\frac{1}{2} \frac{\partial^2 \phi(x=0, y=0, z)}{\partial z^2}. \tag{4.27}$$

From this expression, we can derive the transformation matrices for the radial

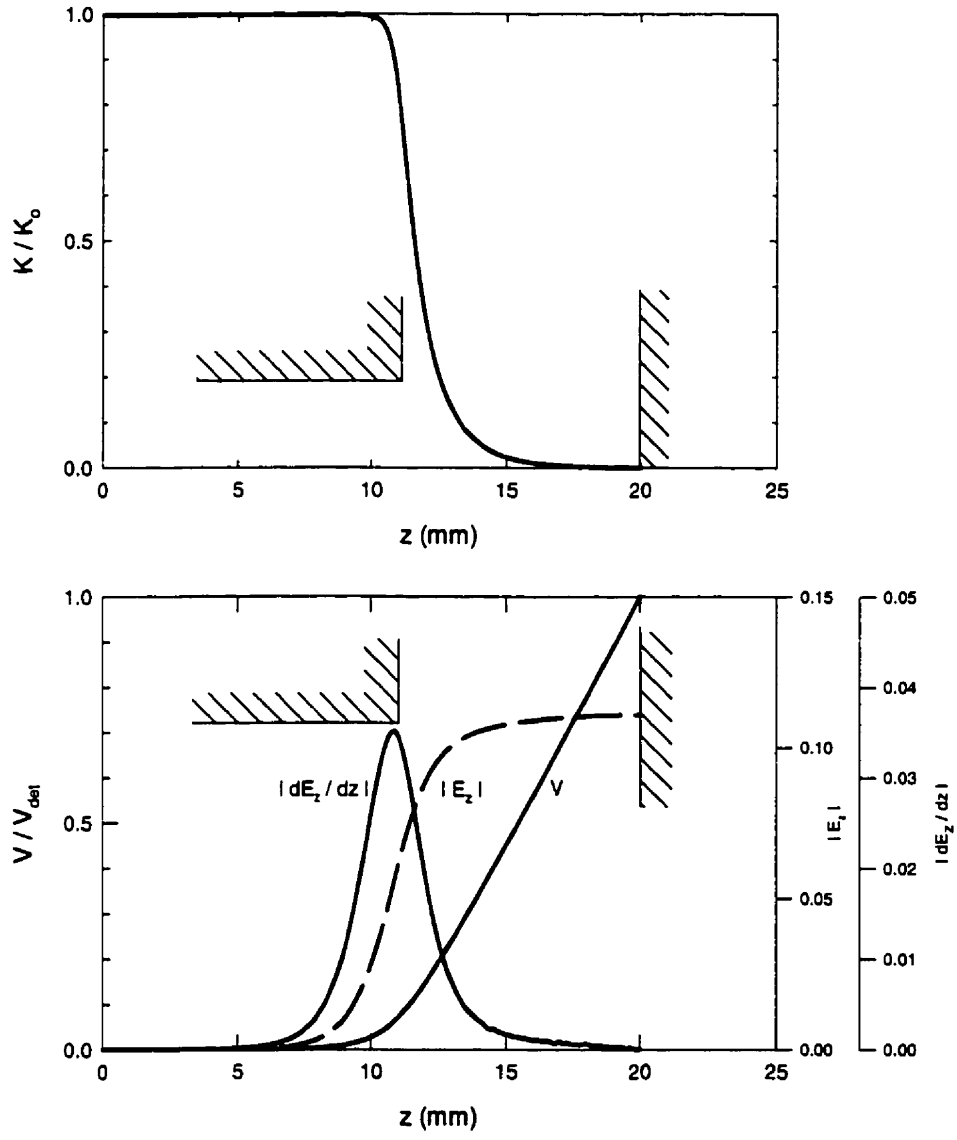

Figure 4.11: The electric fields implemented in the simulation of the ion beam extraction from the quadrupole rods (RFQ_EXT): (a) the rf fringing field and (b) the axial potential and its derivative. The hatched objects represent the position of the electrodes.

component of the extraction field just like we did for the quadrupole field (refer to Chapter 2). The axial and the radial components are shown in Figure 4.11 (b).

Of course, this approximation will be more accurate when the ion beam is small and all the ions are close to the axis. When the ion beam is wide and the ions have larger radial displacements, the simulation will introduce errors. These errors will be discussed in Chapter 6 (Experimental Results).

4.7.2 Ion beam envelope evolution in the extraction fields

In equilibrium, the distribution of the particle beam is an rf distorted Gaussian. When the ions are close to the end of the miniature quadrupole, they experience both the rf fringing and the DC extraction fields. In the RFQ_EXT simulation, the ion beam is represented by many rf distorted ellipses which are the representative equi-density lines for each specific rf phase. These ellipses evolve under the influence of the rf and extraction fields.

The starting ellipses are determined by applying the rf deformation matrix to an Gaussian distribution in the pseudo-potential.

4.8 Spatial Distribution of the ion beam

For the determination of temperature, the experimental and the simulated beam distributions at the detector were compared. The RFQ_EXT simulated beam distribution was constructed by averaging (superimposing with same weight) the 20 distributions for different rf phases. Here the constructed beam distributions are presented.

The radial distribution of the ions at a specific axial position can be constructed by superimposing the normalized distributions of the 20 phases. The rf phases in x

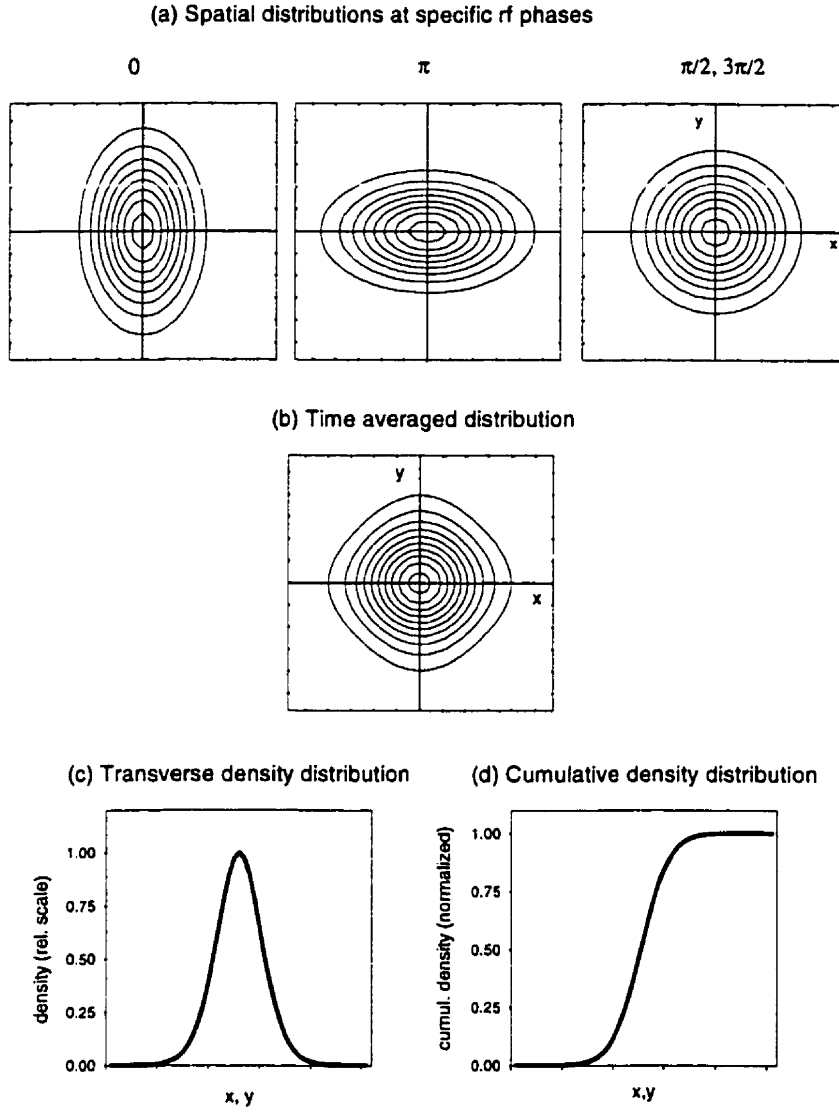

Figure 4.12: (a) The spatial distribution of the ion beam for a few specific rf phases, (b) the time averaged distribution , and (c) the x or y axial distribution in differential form and (d) in integral form

and y are different by 180° and the distribution at a specific rf phase is not axially symmetric but it is elongated along the x or along the y axis. The time averaged distribution is also not axially symmetric but has a 4-fold symmetry. Figure 4.12 shows the beam distribution for a few specific rf phases as well as the time averaged distribution constructed from the 20 equally distributed rf phases.

Chapter 5

Simulations

This chapter is devoted to the description of the various simulations that were used to predict the optimal experimental conditions, to study the cooling process and the cooled beam, and to analyze the cooled beam data. In this work, there are two distinct regimes: the ions can be either in a buffer gas or in a high vacuum. Two modeling programs were developed to find the optimal pressure for the ion beam guide and to analyze the beam profile. The first one simulates the ion motion in the quadrupole field at a buffer gas pressure, and the other one simulates ion motion in high vacuum with the rf fringing and dc fields.

The cooling process is not a directly observable process and computer simulations can be a useful tool to study such a process. There are several ways to simulate the buffer gas cooling process and the simplest of these methods is the calculation of the ion trajectories using the drag force model introduced in the previous chapter.

5.1 Trajectory calculation using a drag force model

As was seen in Chapter 4, while the drag force calculations based on ion mobilities do not give a complete picture of the effect of the buffer gas collisions, it can be used for analytical studies of certain phenomena. An important result of such an analytical study is the determination of the optimal buffer gas pressure. These conditions were checked by numerical calculations and are presented in Chapter 6.

The equations of motion with the drag force for the mass filter, can be written as

$$\begin{bmatrix} \ddot{x} \\ \ddot{y} \end{bmatrix} + \frac{b}{m} \begin{bmatrix} \dot{x} \\ \dot{y} \end{bmatrix} + \frac{e}{mr_0^2} (U - V\cos\Omega t) \begin{bmatrix} x \\ -y \end{bmatrix} = 0, \tag{5.1}$$

$$\ddot{z} + \frac{b}{m}\,\dot{z} - \frac{eE_{ax}}{m} = 0. \tag{5.2}$$

These are the same equations of motion as those for the quadrupole mass filter without the buffer gas except that the equations for the x and y directions have an additional drag term and the equation for the axial z direction has a constant force term and a drag term. As was seen in chapter 4, the drag force constant b is related to the ion mobility K by

$$b = \frac{e}{K}. \tag{4.13}$$

The equation of motion with the drag force was solved numerically by using the fourth-order Runge-Kutta method. From the trajectory solutions, the decay constants were derived and compared with the analytical results of the decay constants in Chapter 4, and the results are presented in Chapter 6.

5.2 The Monte Carlo simulation

The Monte Carlo (MC) simulation accounts for the collisions by using statistical probabilities. In the MC simulation, the following assumptions were used:

1. Ion-ion interactions are much rarer than ion-neutral gas interaction and can be neglected.

2. The collisions of the ions with the neutral gas molecules are considered to be elastic.

Several ion-neutral collision potential models were used in the Monte Carlo simulation.

5.2.1 The ion-neutral interaction potential models used in the Monte Carlo simulation

The simpliest model is the classical hard sphere model with constant radius. This model can predict some basic characteristics of the collisions, but it can not give accurate quantitative predictions. The true scattering cross-section and the scattering angles of the collisions are different from those predicted by the hard sphere model, and several modified hard sphere models have been implemented to account for this. The true interaction potential is soft rather than hard, and therefore the scattering angles are not equally distributed in the center of mass frame, as it is for hard sphere collisions. In previously documented efforts to solve this problem, the impact parameters [Lon93] and scattering angles [Jul95] have been manipulated without explanation.

Table 5.1 summarizes the ion neutral collision potential models that have been used.

Model	**Cross section**	**Prediction**	**calculation speed**	**Ref.**
classical hard sphere	constant	worst	simple, fast	[Ved83]
hardsphere variablesize #1	$\sim \frac{1}{v}$ constant collisional probability	bad	simple, medium speed	[Lon93] [Jul95]
hard sphere variablesize #2	$\sim C\left(\frac{E}{N}\right) \times \frac{1}{v}$	best in hard sphere model	simple, medium speed	this study
realistic potential	determined by minimun scattering angle	agrees well with the experimental results	complex, slow	this study

Table 5.1: The collisional interaction potential used in the Monte Carlo simulation

As pointed out above, the classical hard sphere (HS) interaction model is the simplest but its results do not agree with experimental results such as the variation of the mobility with velocity at high electric fields. A simple correction to the classical HS model is the use of variable-sized particles. The first variable size HS model (HS1 model) was based on the Langevin collision theory for inert gases, which says that the collision cross-section is inversely proportional to the velocity. According to this model, the collisional frequency per unit time is a constant [Lon93]. Some evidence was reported stating that the collisional frequency depended on the particles velocity [Goe92], but still, the model agrees well with mobility for inert gas. For non inert gases, the HS1 model deviates from the mobility, and another variable size HS model (HS2 model) was developed and compared with a more descriptive collision model, the realistic potential model (RP model), in this thesis. For the HS2 model, the collision frequency is not directly proportional to the inverse of the velocity. The collisional frequency function for that model is calculated from the mobility data. The HS2 model approaches the HS1 model when the buffer gas is inert. Thus the HS2 model is a generalization of the HS1 model and from now on, the term "HS model" will be used to describe the HS2 model.

The hard sphere interaction model has often been used to simulate the motion of the ions in buffer gas, in the quadrupole field trap. These simulations may show characteristic behaviors such as the decrease in the average kinetic energy of ions and their general movement toward the quadrupole field center. However, the hard sphere model has an inherent handicap in predicting the scattering angle, the distribution of the cooled ions and the mean ion energy. This is because the real ion-neutral potential is not hard and the HS model causes more forward scattering than the true potential does. Therefore several solutions have been implemented by manipulating the probabilities of the scattering angles or of the impact parameters [Lon93, Jul95].

Most ion simulations still use the HS collision model. This is because often the

interaction potential is not known. Also the scattering angle calculations and their implementation are complicated for scatterings with known interaction potentials. While the results derived with this model are less accurate than those calculated with the RP model, when the interaction potential is not known, the HS model can be a useful approximation.

Realistic Potential model

The simulations in the present work used the "(12,6,4) ion-neutral" molecular interaction potential:

$$V(r) = \frac{C_{12}}{r^{12}} - \frac{C_6}{r^6} - \frac{C_4}{r^4} \tag{5.3}$$

where the C's are constants. The inverse fourth power term accounts for the attraction between the charge of the ion and the dipole it induces in the polarizable neutral. The coefficient C_4 is known rather accurately, since it is given by the simple expression

$$C_4 = \frac{1}{2}q^2\alpha \tag{5.4}$$

where q is the ionic charge and α is the polarizability of the neutral entity. The inverse sixth power term accounts for the charge induced quadrupole attraction plus the London dispersion attraction [Vie75].

The coefficient C_6 can often be calculated approximately but it is seldom known as accurately as C_4. The inverse twelfth power term is an empirical representation of the short-range repulsion.

The constants were determined using the mobility data [Ell78] and Tables of Transport collision Integrals for (n, 6, 4) Ion-Neutral Potentials [Vie75]. The constants are $C_{12} = 1.0117 \times 10^5 eV\mathring{A}^{12}$, $C_6 = 58.304 eV\mathring{A}^6$ and $C_4 = 16.662 eV\mathring{A}^4$ for $Cs^+ - N_2$.

The scattering angle in the center of mass coordinate system is calculated as a function of b and E from the classical equation of motion

$$\theta(b,E) = \pi - 2b\int_{r_0}^{\infty}\left[1 - \frac{b^2}{r^2} - \frac{V(r)}{E}\right]^{-1/2}\frac{dr}{r^2}, \tag{5.5}$$

where θ is the deflection angle of the ion after a collision of energy E and impact parameter b, and the distance of closest approach r_0 is the outermost root of

$$1 - \frac{b^2}{r_0^2} - \frac{V(r_0)}{E} = 0. \tag{5.6}$$

In the program, the scattering angle was calculated by numerical methods and the results were stored in an array. The actual interaction range goes to infinity, so that one has to determine an appropriate cut-off range. In the program, the cut off value $b_{\max}$ was chosen by determining a smallest angle of deflection $\theta_{\min}$. Two interaction potential minima, $\theta(b) = \theta_{\min}$ appear and the larger corresponding b is the meaningful $b_{\max}$. The scattering angle as a function of the impact parameter and energy was calculated for an adequate range of experimental conditions and individual scattering angles were interpolated using the specific b and E of the collision. Figure 5.1 shows a typical scattering calculation for a specific relative energy for RP and HS models. The figure shows big differences in scattering angle between the two models.

5.2.2 Implementation of the collisions

The collision probability

The collisions were implemented by using the following method.

The probability of collision during a time step $P(dt)$ is

$$P(dt) = 1 - e^{-\frac{vdt}{\lambda}} \simeq \frac{vdt}{\lambda} \tag{5.7}$$

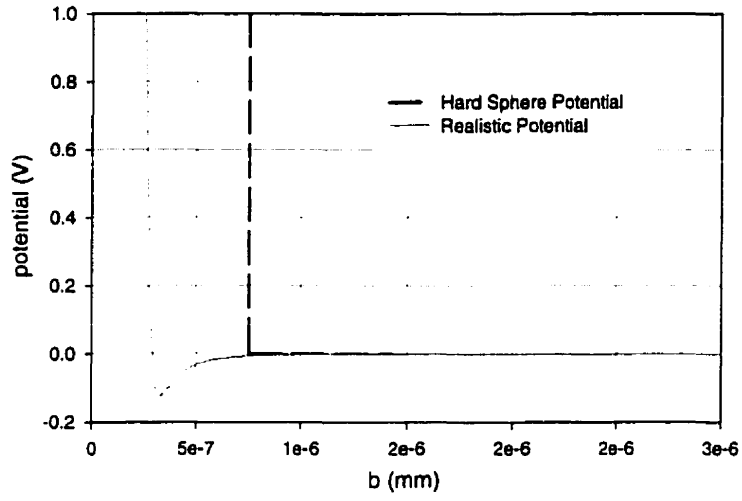

(a) interaction potentials

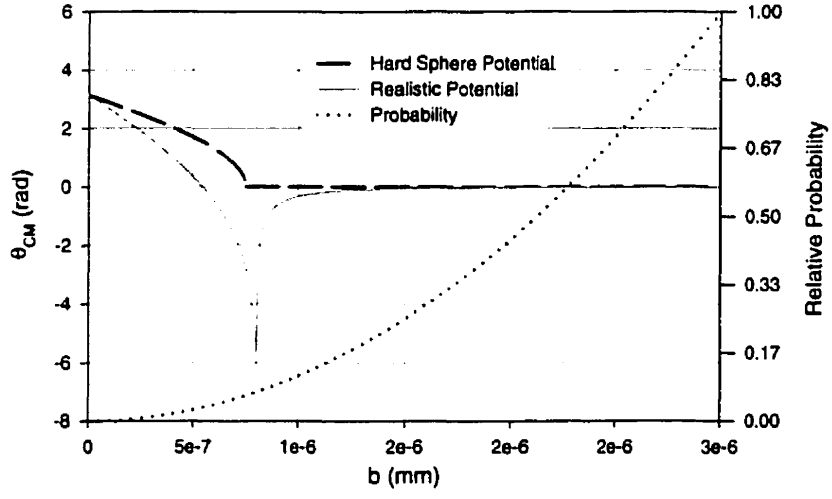

(b) scattering angle

Figure 5.1: The interaction potentials and the scattering angles as functions of the impact parameter.

where v is the velocity of the ion and λ is mean free path, which may be expressed as

$$\lambda = 1/n\sigma \tag{5.8}$$

where n is number density of the neutral gas molecules and σ is the collision cross-section, which is defined by

$$\sigma = \pi b_{\max}^2. \tag{5.9}$$

A random number $0 \leq R \leq 1$ was generated. If R was less than or equal to $P(dt)$ then the collision was deemed to have occurred.

Determination of the impact parameter

When a collision occurs, the scattering angle is determined by random number generation. First the probability of an impact parameter r is proportional to r :

$$P(b = r)dr = rdr. \tag{5.10}$$

The impact parameter is determined by taking two random numbers R_1 and R_2. If $R_1^2 + R_2^2 > 1^2$, then we start over, until $R1^2 + R2^2 \leq 1^2$. The impact parameter is then

$$b = \sqrt{R_1^2 + R_2^2} b_{\max}. \tag{5.11}$$

The change in kinetic energy

From the impact parameter and the initial energy of the ion, the scattering angle can be calculated by Eq. 5.5. For the elastic collision, the kinetic energy (E') after the collision in the lab frame is given by [Mar70]

$$E' = \left(\frac{M_1^2 + M_2^2}{M^2} + \frac{2M_1 M_2}{M^2} \cos\theta_{CM} \right) E \tag{5.12}$$

where M_1 is the mass of the ion, M_2 is the mass of the neutral gas molecule and $M = M_1 + M_2$.

Tracing the ion path

To trace the ion path, we need the velocities after the collisions. We have already calculated the speeds by looking at the kinetic energy and the scattering angles and now we need another parameter, the azimutal angle, to fully specify the direction in three dimensional space. The azimutal angle ϕ can be taken to be $2\pi R_\phi$, where R_ϕ is a random number between zero and one.

In the actual calculation the particles are followed with reference to a fixed frame (the lab frame). The scattering angle θ, with respect to the quadrupole axis z, is determined after each collision. The cosine of this angle, after the ith collision, is given by

$$\cos\ \theta_i = \cos\theta_{i-1}\cos\psi_i + \sin\theta_{i-1}\sin\psi_i\cos\phi_i \tag{5.13}$$

where ϕ, θ, ψ are the directional angles relative to the x, y, z axes respectively. The directional cosines with respect to the other Cartesian coordinates (transverse directions) are determined similarly.

The neutral gas velocity implementation

The velocity of the colliding neutral gas molecule was chosen by using the Maxwell-Boltzmann distribution of speeds in the laboratory reference frame .

Reliability check

The reliability of the Monte Carlo simulation program was tested by comparing the calculated mobilities with the experimental mobility data. The reported mobilities were measured to within a few percent error for most monatomic ions in a gas. If some of our implementations are wrong, then the calculated mobilities will deviate from the measured data. Figure 5.2 shows the calculated and experimental mobilities. The mobility of the simulation is 6 to 17% lower than the experimental one. This

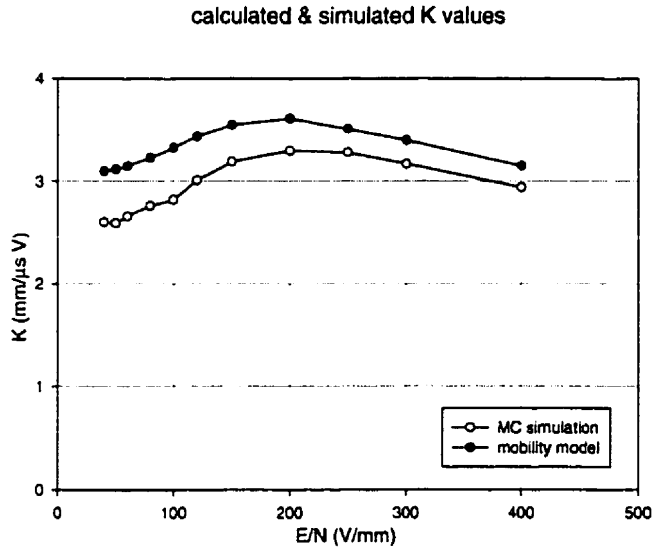

Figure 5.2: The calculated mobilities with the realistic potential model and the experimentally determined data.

error seems to come from an error in the ion-neutral gas interaction potential used in the simulation. This agreement test is more meaningful than such a test performed on the hard sphere model, because the hard sphere model uses a manipulated variable cross-section to get an agreement with the experimental mobility.

The increase in the value of q for which the motion is stable, referred to here as the stable q expansion, at high buffer gas pressures can also be used to test the reliability. The calculated stable q value expansion and temperature are compared with the experimental result in Chapter 6. These calculated stable q value expansions agree well with the experimental data (see Figure 6.22).

The electric field implementation

All of the potential arrays were calculated by the REX_3D program, a successive over-relaxation with variable grid step size, and the electric field was calculated from the potential array by linear interpolation. The axial field in the quadrupole rod is not completely parallel to the axis and has radial components (see Fig. 4.6), but in the simulation, the axial field was implemented as a constant parallel field.

For the axially symmetric trap (Paul trap), the electric field has been studied by using the multipole expansion [Lun91, Lon93, Pet95]. The cylindrically symmetric field in 3-D can be treated as a two dimensional problem and we are only interested in the field near the axis and therefore the multipole expansion coefficients can be calculated by fitting the axial potential only. Of course, the multipole expansion in the middle of the quadrupole mass filter is dominated by the quadrupole component if the ratio of the radius of the rods to the opposite rod distance is optimized. When the ions enter and exit a quadrupole mass filter or an ion guide, they experience fringing fields and therefore the multipole components of the fringing region are important. The main advantages of the multipole expansion are the ease of its implementation and the short computation time. Finding the multipole components of the 3-D fringing field caused by the quadrupole beam guide is complicated and in this study, a complete potential map was used to describe the electric field in this region.

As pointed out in Chapter 4, a miniature quadrupole interfacing the two different pressures regions was used to transport the ions into the vacuum. The pressure varies along the axis of this quadrupole. Additionally, there is no axial field, but the ions experience the space charge effect in the radial and axial directions. The radial expansion will reduce the confining effect of the space charge on the ions and the axial component of the space charge effect will push the ions along the quadrupole axis. In the Monte Carlo simulation the axial push of the space charge was simulated by a

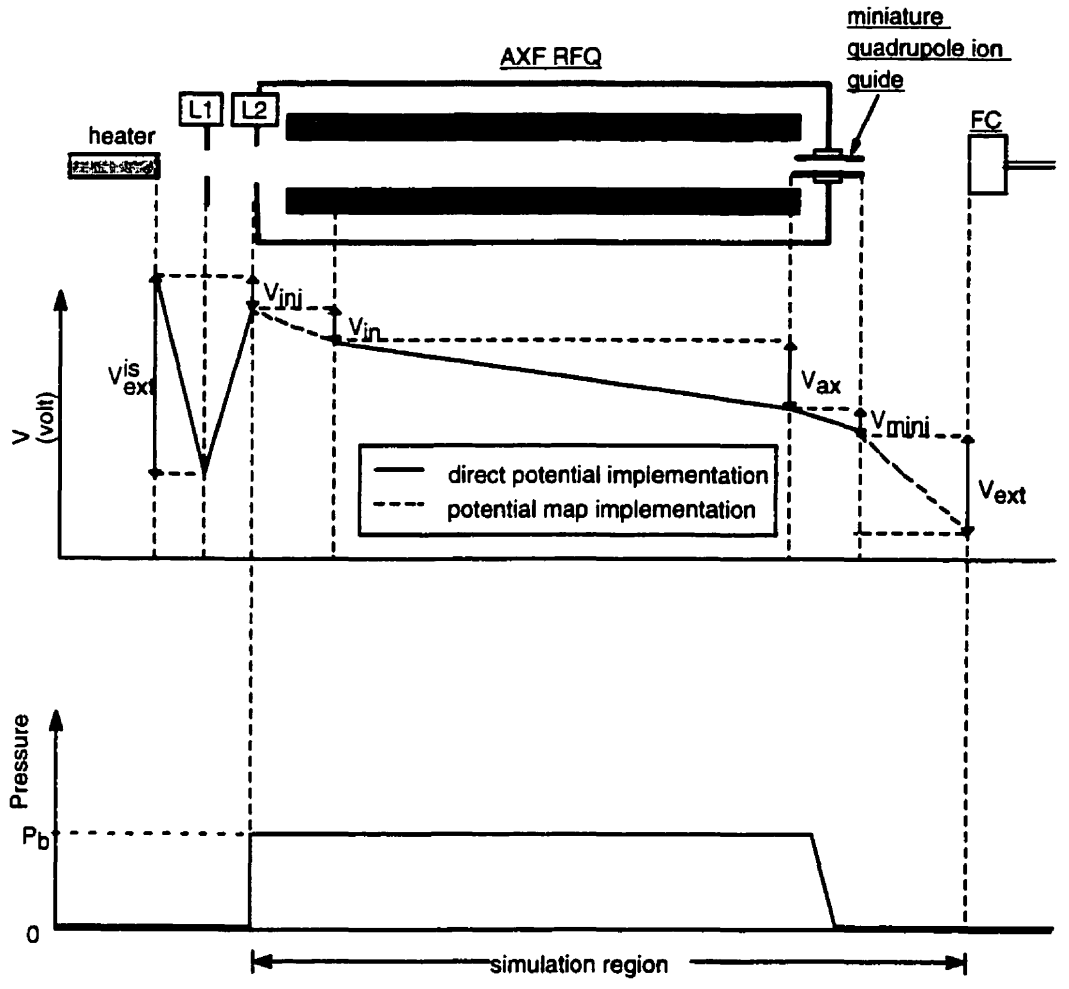

Figure 5.3: The pressure and electric potential implementation in the Monte Carlo simulation.

small axial electric field, the strength of which was set to duplicate the experimental drift time measurements.

Pressure implementation

In the simulation, the pressure of the buffer gas cooling cell was implemented as being a constant except inside of the miniature quadrupole. The ion entrance is 1 mm. This is smaller than the mean free path of the buffer gas and so the pressure variations in the entrance region are negligible. The miniature quadrupole exit opening of $2r_0 = 3.5\ mm$ is comparable in size to the mean free path and the pressure was assumed to fall linearly along the closed part of the quadrupole (see Figure 5.3).

Chapter 6

Results and Discussion

6.1 Simulation of the cooling process

The cooling process was studied by both a mobility calculation and a Monte Carlo simulation. The trajectories calculated from mobility considerations give a rough estimate of the optimal cooling conditions and the Monte Carlo simulation shows the statistical properties of the cooling process and can also be used to predict the optimal cooling conditions.

6.1.1 Trajectory calculations using mobility

The mobility calculation gives rough information about the optimal cooling parameters, such as the decay time constants and the optimal pressure. The damping time constants have been calculated by the analytical method discussed in chapter 5. The damping constants from such an analysis were then checked by numerical trajectory calculations.

Representative graphs of the trajectories calculated for various buffer gas pressure are shown in Figure 6.1. This figure shows that the macro-motion changes a lot for

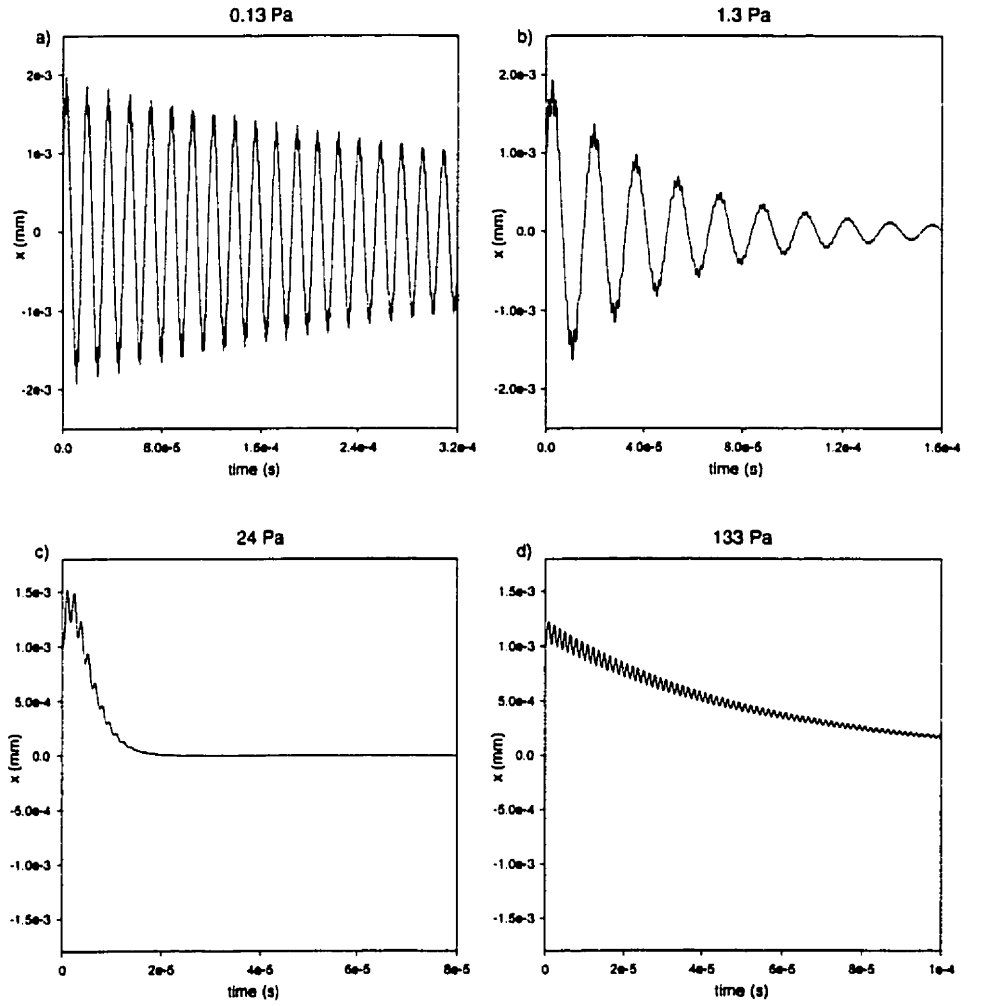

Figure 6.1: The calculated trajectories of cesium ions in nitrogen buffer gas using mobility. The operation condition was f = 0.7 MHz V=300 V.

different buffer gas pressures while the micro-motion changes only slightly. At low buffer gas pressures the macro-motion amplitude decays slowly and this decay rate increases with pressure up to a critical pressure after which it decreases with further increase in pressure.

The amplitude decay time constant was deduced from these calculated trajectories and is shown Figure 6.2. The decay time constant agrees well with the analytical results derived in Chapter 5 (for underdamping pressures). This figure shows that the critical damping occurs at a pressure of about 10 Pa for cesium ions in the nitrogen buffer gas. The figure also shows that for lower driving frequencies with the same amplitude, the critical damping occurs at higher pressure and the critical damping time constant is shorter. This trend was derived analytically in Chapter 5.

Generally the optimal condition for ion cooling is when the pressure is lowest and the cooling time is shortest. A low pressure is preferred because of pumping requirements and a short cooling time because it minimizes the possible loss of the ions. However, it is seen from the above that these conditions are conflicting and some compromise must be arrived at. Generally this is using the minimum buffer gas pressure that will do the job. For a constant length of the cooling system, this can be found from Figure 6.2 by comparing the amplitude decay time, the axial energy decay time with the drift time (or cooling time). Of course, in the real situation, the cooling rate varies for each ion by the stochastic effects of the collisions and the optimal cooling condition found by the mobility calculation is only an approximation.

6.1.2 Effect of buffer gas collisions in phase space

The cooling process itself is not directly observable in this experiment and so the process was studied by computer simulation. A demonstration of this cooling process was carried out using a Monte Carlo simulation with 25 sample particles, first in

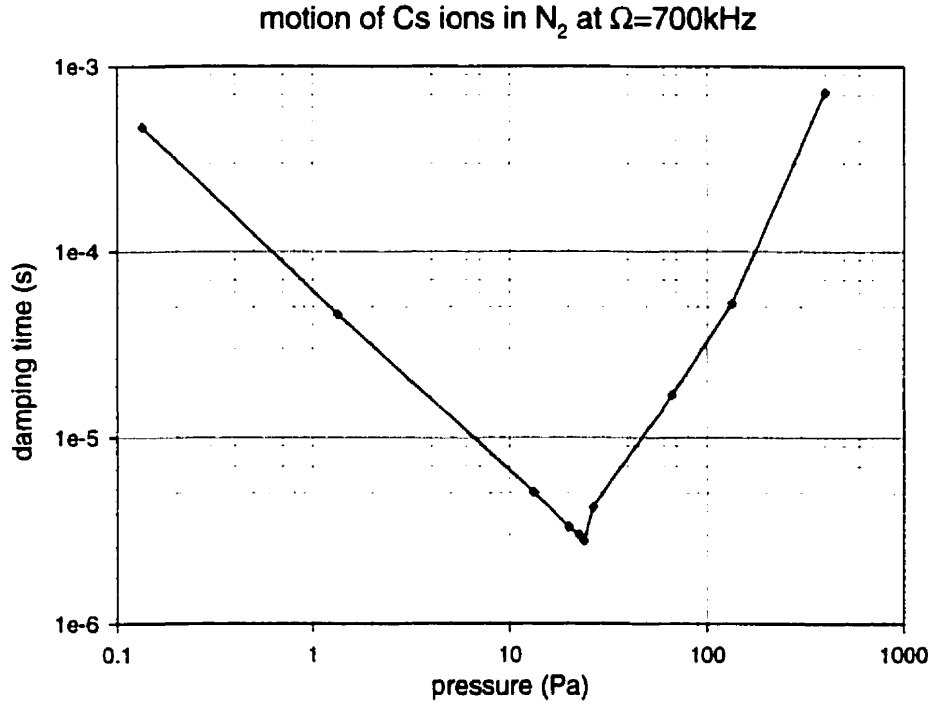

Figure 6.2: The amplitude decay time constant of the macro-motion as a function of the pressure.

a vacuum and then in 8 Pa nitrogen buffer gas, deliberately placed in their action diagrams to straddle the acceptance limit of the ion guide. Figure 6.3 shows the simulation results for one rf cycle along with the acceptance ellipses. The acceptance ellipses for different rf phases were calculated for the operating values: $q = 0.47$ and $\Omega/2\pi = 0.7$ MHz.

For the ideal vacuum, the particle configuration changes in a regular way, the density remaining constant. Also, the particles remain either inside or outside of the acceptance ellipse for all rf phases. The particles that started outside of the acceptance were removed near the most spatially stretched rf phase (180°) within a few rf cycles.

For the 8 Pa buffer gas pressure, the regularity of the particle configuration was removed, the particle density changed, and the particles moved in and out of the acceptance ellipses with changing phases.

At 8 Pa the collisional frequency was about 14 collisions/rf- cycle. The overall effect of these collisions is a reduction of the kinetic energy and confinement of the particles to the center of the trap (the axis of the ion guide), making them more stable. The collisions lead to energy exchanges between the ions and the neutral gas. When the ion energy is higher than the neutral's, the energy loss of the ion by collision will be the main process. The ion energy loss does not lead necessarily to a more stable state. Sometimes the lower energy can result in an unstable state for a specific rf phase.

6.1.3 The cooling process

A sample result of the Monte Carlo simulation of the full cooling process in the ion guide, using input ions that simulated those from the ion source, is shown Figures 6.4 and 6.5. In the figures, the ions' spatial and phase space distributions are presented

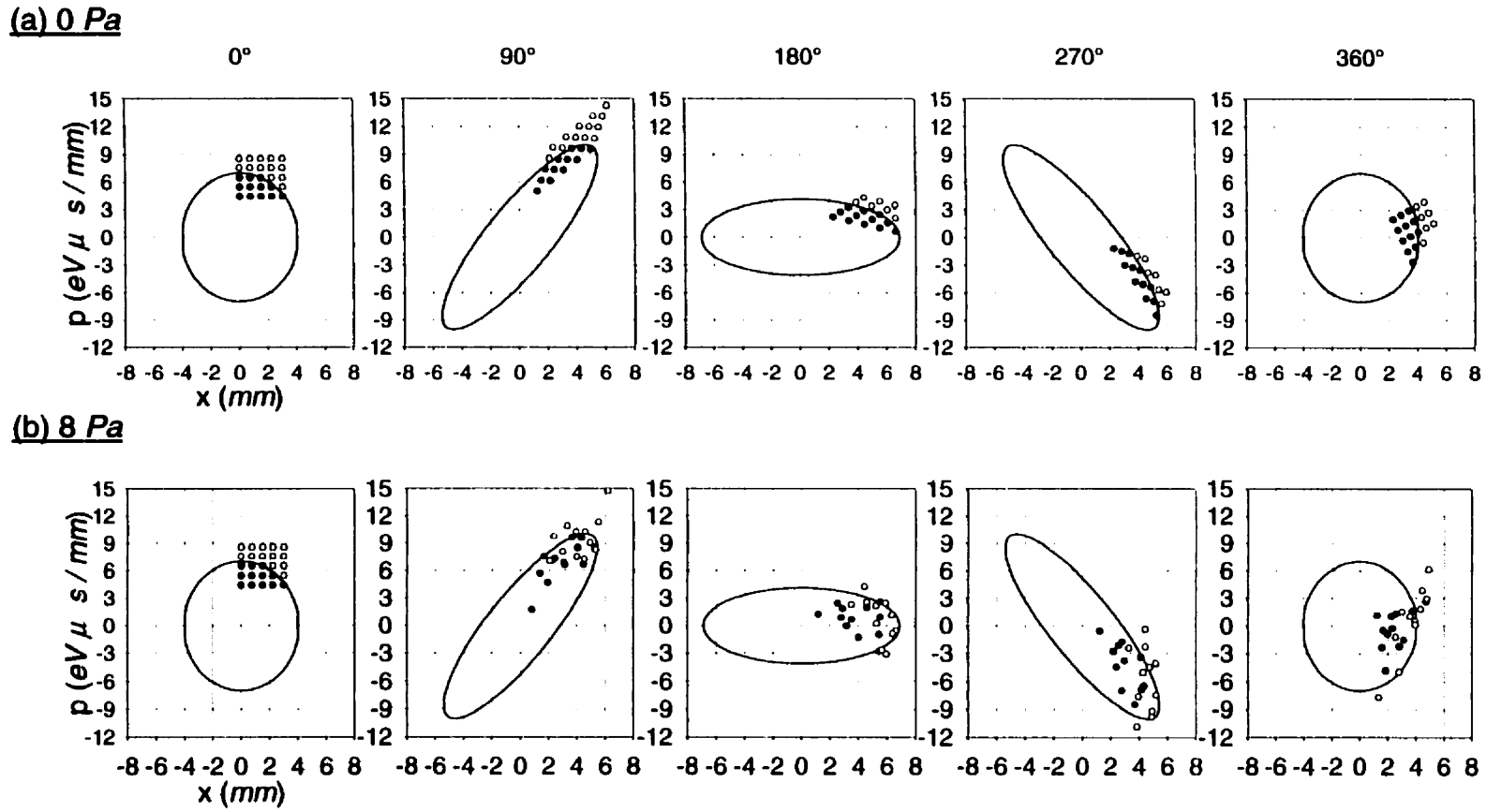

Fig 6.3: The effect of buffer gas collisions in phase space. (a) at vacuum the density is constant and the particles that start outside of the acceptance ellipse are removed in a few rf cycles and (b) at nitrogen buffer gas pressure, the density is not constant and particles move in and out of the acceptance ellipses. The drawing were generated using the Monte Carlo simulation.

for various axial positions. The simulation was done for 4000 cesium ions in nitrogen buffer gas. In the Monte Carlo simulation, each ion experiences collisions based on a statistical probability. The initial ion beam diameter was 1 mm and the momentum spread in the radial direction was approximated from the thermal energy of ions at the heater temperature (0.1 eV). The injection energy was 60 eV. The beam guide was operated at 0.7 MHz, 300 V rf amplitude at 8 Pa nitrogen buffer gas pressure.

From the ion spatial and phase space evolutions it is apparent that the cooling process can be divided into three stages.

Initial cooling stage (Figure 6.4 : 0-50 mm)

In this stage the ions are injected into the cooling system with a high axial energy. Therefore the axial velocity of the ions is much higher than the radial velocity and by collision, part of their axial energy is transferred to the radial direction. Thus, the transverse direction phase space area occupied by the ions is expanding and the radial distribution disperses with time (and axial displacement). The radial distance of ions can become larger than the physical limit of the beam guide and the ions that hit the rods will be lost. Only the most energetic ions (in the radial direction) are lost and this will reduce the total kinetic energy of the beam. This process is called evaporative cooling. In this stage, there are three main processes: the increase of the transverse energy by transfer of the axial energy, the collisional cooling in the transverse and axial directions and the evaporating cooling.

Second cooling stage (at about 50-80 mm)

The axial velocity is now close to the radial velocity and since the energetic ions were mostly lost in the first stage there is virtually no further ion loss. The ions lose and gain kinetic energy by collision with the buffer gas and by rf heating, but overall the ions lose more energy than they gain until they reach thermal equilibrium. The spatial and phase space volumes both shrink. In this stage, the net effect is a cooling in both the transverse and axial directions.

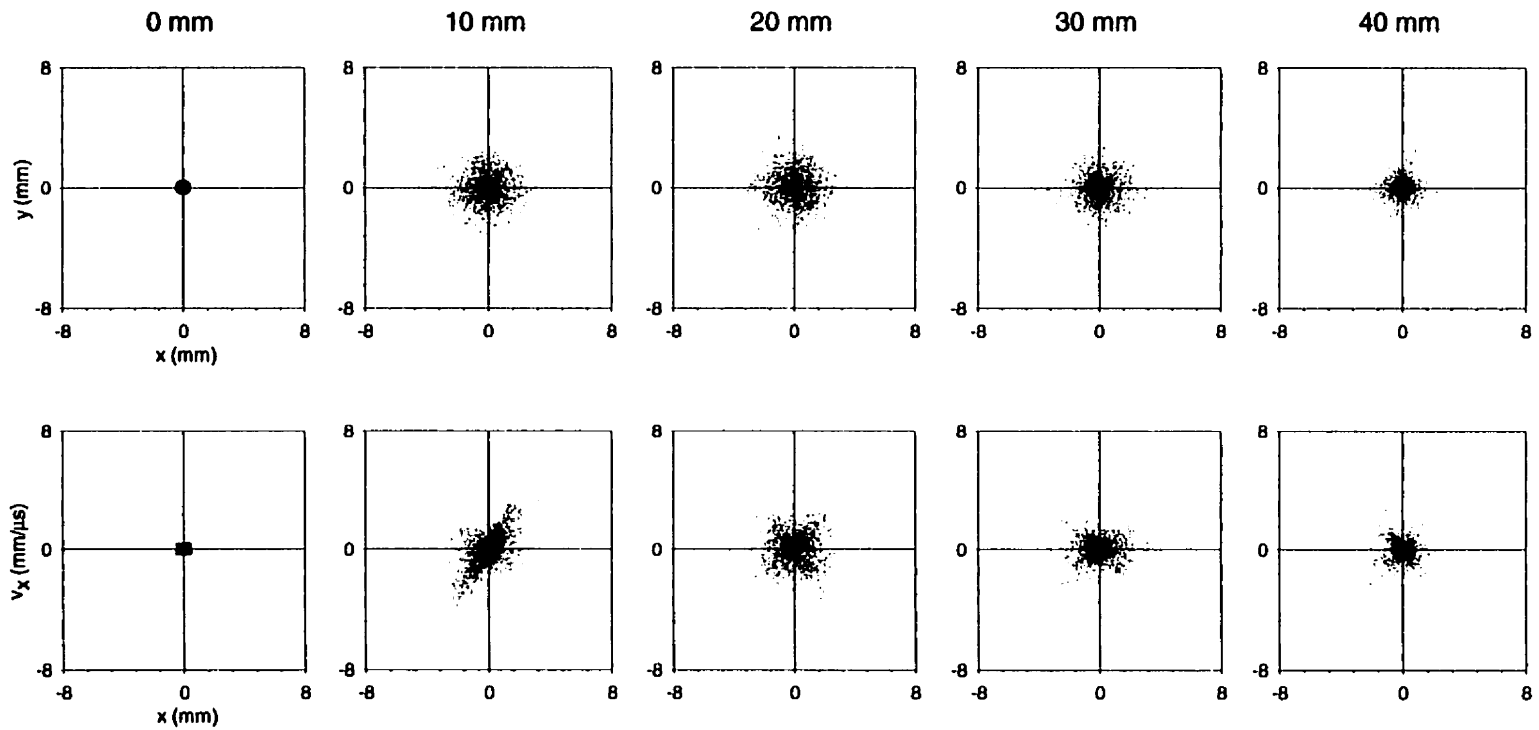

Figure 6.4: The evolution of the ion beam in the AFX_RFQ (first half).

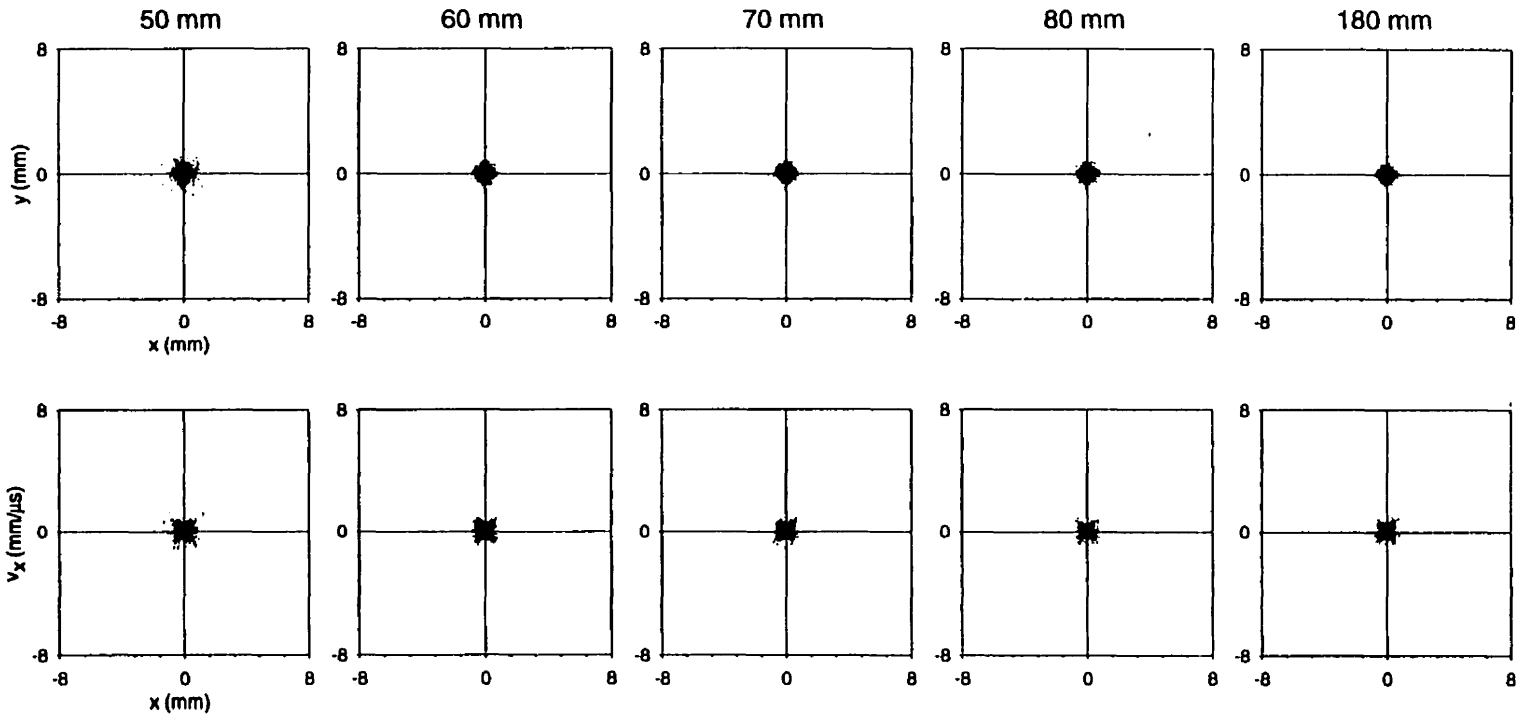

Figure 6.5: The evolution of the ion beam in the AXF_RFQ (second half).

Cooling stages	Velocity	Beam density and size	Main process
initial cooling	$v_z \gg v_x, v_y$	density decrease beam broadening	axial momentum to transverse momentum, evaporative cooling
second cooling	$v_z \geq v_x, v_y$	density decrease beam narrowing	collisional cooling > rf heating
thermal equilibrium	$v_z \cong v_x, v_y$	density constant beam size constant	collisional cooling = rf heating

Table 6.1: The cooling process

Thermal equilibrium stage (at about 80-180 *mm*)

In this stage the spatial and phase space volumes remain constant. The ion temperature need not be the same as that of the buffer gas, for the reasons presented in Chapter 2.

These stages of the cooling process are summarized in Table 6.1

Simulations using mobility do not show the initial cooling and thermal equilibrium processes. Therefore mobility simulations have higher transmission than the experimental results and the ion beam continuously shrinks in both space and phase space. Other type of simulations with quasi-mobility calculations, such as Monte Carlo simulations with collisional effect implementations by collisional damping [Jul95] will give results similar to those of the mobility simulation.

6.1.4 Interaction potential effect in the MC simulation

To study the effect of the ion-neutral interaction potential on the cooling process, RP (realistic potential) and hard sphere (HS) models in the Monte Carlo simulation were

used to calculate the transverse trajectory and the axial energy. Figure 6.6 shows the trajectories calculated by the two models. The RP model has a longer interaction range and has about 9 times more collisions than the HS model. In the RP model, the collisions change the directions of the ions greatly and the RP model trajectories have more abrupt deviations than they do in the HS model.

Thus the HS model is more similar to the mobility drag model than is the RP model. This effect is also shown in the axial energy calculations, as is shown in Figure 6.7. With the RP model, the axial energy decreases more rapidly than with the HS model. The evolution of the cross-section also shows a slower energy decrease with the HS model than with the RP model. The beam evolution in phase space and in spatial space of the MC simulation with the HS model is similar to that with the RP model except it exhibits a slower decay time.

6.2 Beam profiles and temperatures in the equilibrium state

Temperatures that described the equilibrium state of the ions in the ion guide were determined from both the Monte Carlo simulation results and the experimental beam profiles as observed at the detector. The method of extracting the temperature from the experimental results has already been described in Chapter 4. The method for extracting temperatures from the Monte Carlo results is similar except that here it is possible to extract the temperatures more directly from the results since data is obtainable for any point in the system, rather than just at the detector, and information from the momentum distribution is also available, rather than just for the displacement. The results obtained from the simulations will be presented first.

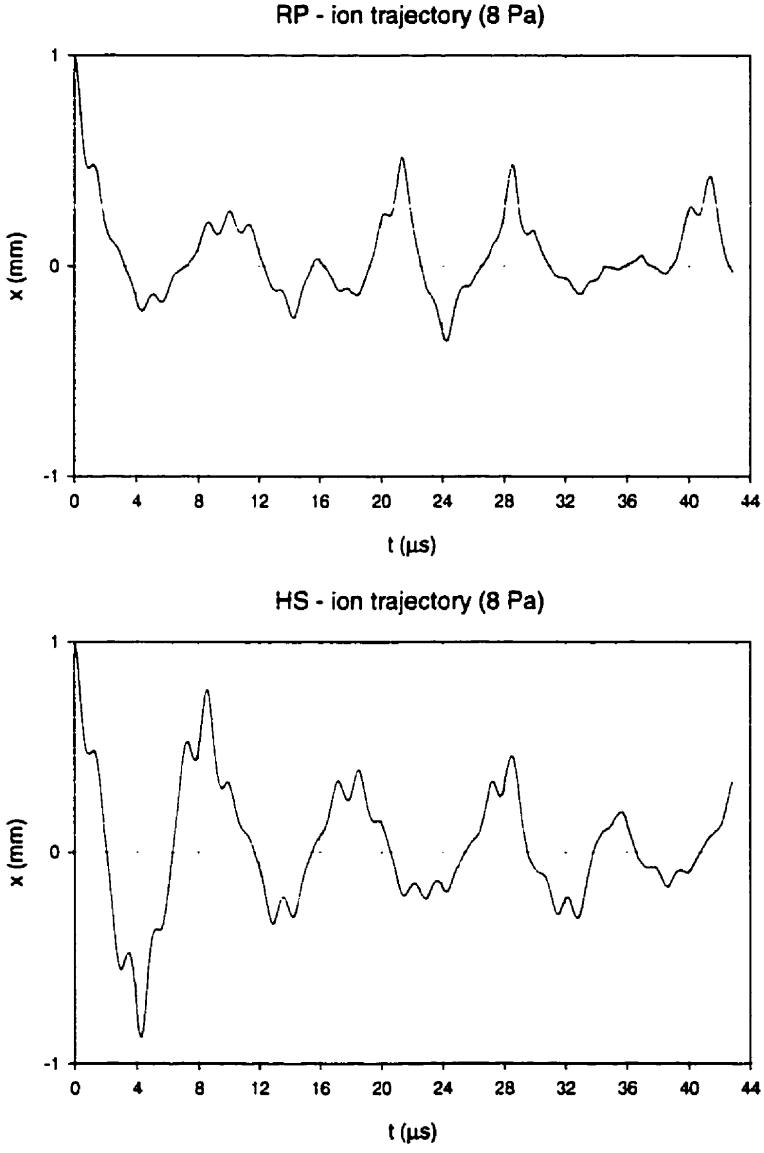

Figure 6.6: Trajectories calculated by the MC simulations (a) with the real potential model and (b) with the hard sphere model.

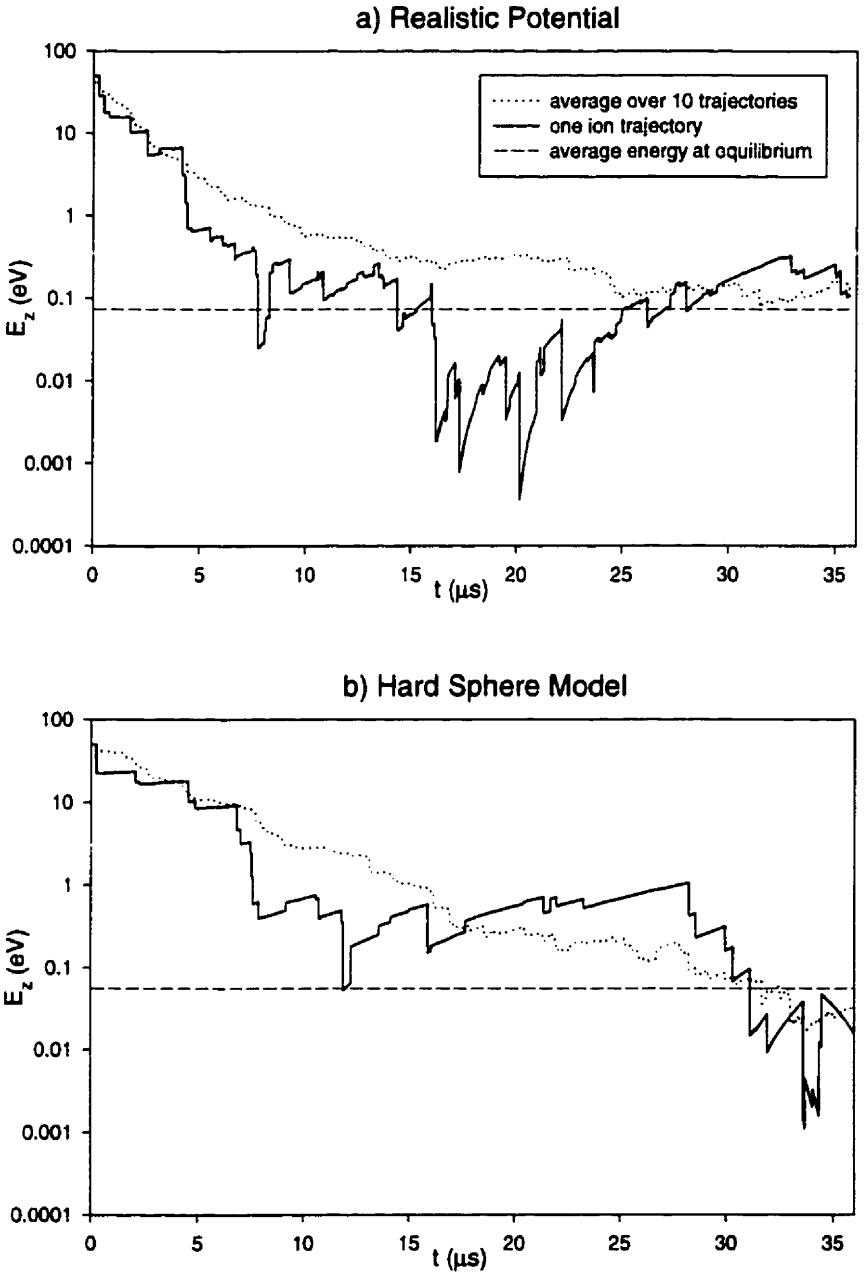

Figure 6.7: The axial energy vs cooling time for the MC simulation (a) with the RP model and (b) with the HS model.

6.2.1 Temperature of the Simulated ion beam

Temperatures were extracted from the calculated ion distributions in the AXF_RFQ ion beam guide after thermalization, in the miniature quadrupole guide and at the detector. To show the sensitivity of the method, Figure 6.8 shows the least-squares fit to the results of a calculation in the miniature quadrupole and the results using temperatures which deviate by ± 15% from the value used for the fit . The simulated distribution contains 4000 cesium ions in 8 Pa of nitrogen under the operating conditions $\Omega/2\pi = 0.7\,MHz$ and 300 V rf amplitude. The figure shows that a distribution of 4000 ions is sufficiently smooth and follows the temperature fitted curve very well.

Figure 6.9 shows temperatures calculated from the Monte Carlo simulation for cesium ions at the same operating conditions as for Figure 6.8 but for all three of the regions of the system. The temperatures as observed at the detector were extracted for a range of extraction voltages, from 25 V to 225 V to check the consistency of the results.

Overall the temperature in the main quadrupole was higher than that in the miniature quadrupole and, as expected, both were insensitive to the extraction voltage. The scatter in their values for various extraction voltages is therefore a test of the sensitivity of the method. The difference in temperatures in the main and the miniature guides suggests that the axial electric field in the main guide affects the temperature by adding some kinetic energy (field energy) to the ions.

In the extraction region between the miniature guide and the detector the MC simulation used a 3-D potential array to simulate the realistic electric field of the extraction region and the temperature at the detector was determined by using RFQ_EXT with the near field approximation outlined in Chapter 4. The most noticeable feature of the derived temperatures is a gradual increase with extraction voltage. It is likely that this is due to ion-molecular interactions in the region near the exit of the

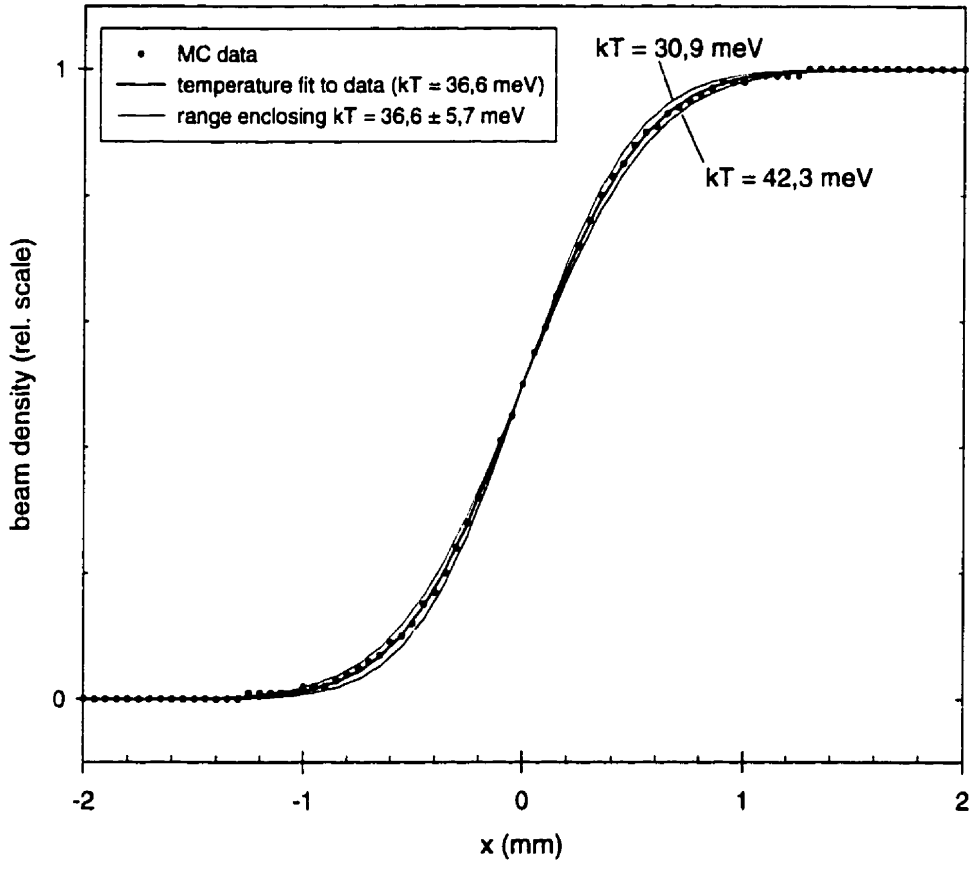

Figure 6.8: A MC simulated distribution in the miniature quadrupole and temperature fitted curves by least square fitting program (Temp-Fit) with two extra curves at different temperatures to give an idea of the sensitivity of the measurement. The operating conditions are 0.7 MHz rf frequency and q=0.47. The figure shows that the beam size is about 2 mm in diameter.

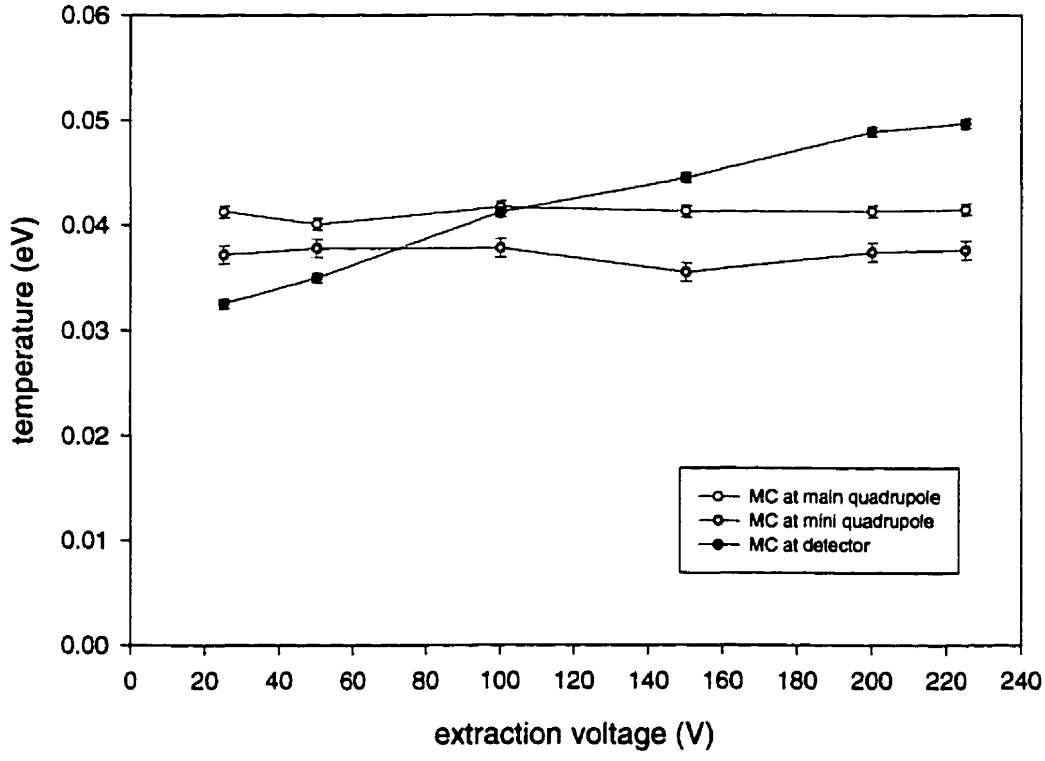

Figure 6.9: The temperature of the ion beam (from the MC simulation). The temperature from the distribution at the detector was calculated from the sigmas at the detector using RFQ_EXT.

miniature guide where the energy scatter would be proportional to the accelerating field.

If RFQ_EXT is an accurate method, then the temperature it would extract from the distribution at the detector should be similar to that in the miniature quadrupole, particularly at low extraction voltages. Figure 6.9 shows that at low extraction voltage the temperatures determined from the distributions at the detector is, in fact, lower by about 10% than the temperature in the miniature quadrupole. This indicates that the error of RFQ_EXT is of this order.

6.2.2 Measured temperature of the cooled beam

The experiments were performed with the same operating conditions as for the above simulation. The beam profile was measured using an ion output current of up to 1 nA and the lower limit was determined by comparing the noise to the signal. The noise was of the order of the signal at the low current limit and the beam profile was obtained from the average of 20 scans of the signal. Typical experimental beam profiles with the theoretical distributions at T that best fits them, for different currents, are shown Figure 6.10.

The temperature as a function of the transmitted current is shown in Figure 6.11. The temperature at zero current was calculated by the extrapolation of the T vs I data. The zero current temperature can be interpreted as the temperature of the ion beam in the low current limit. In the Monte Carlo simulation, the space charge effect was not included and the results obtained should be compared with this zero current limit temperature of the experimental result.

The temperatures obtained by the extrapolations in Figure 6.11 are shown in Figure 6.12 in comparison with the MC simulation as functions of the extraction potential. The temperatures from the experiment and from the MC simulation both

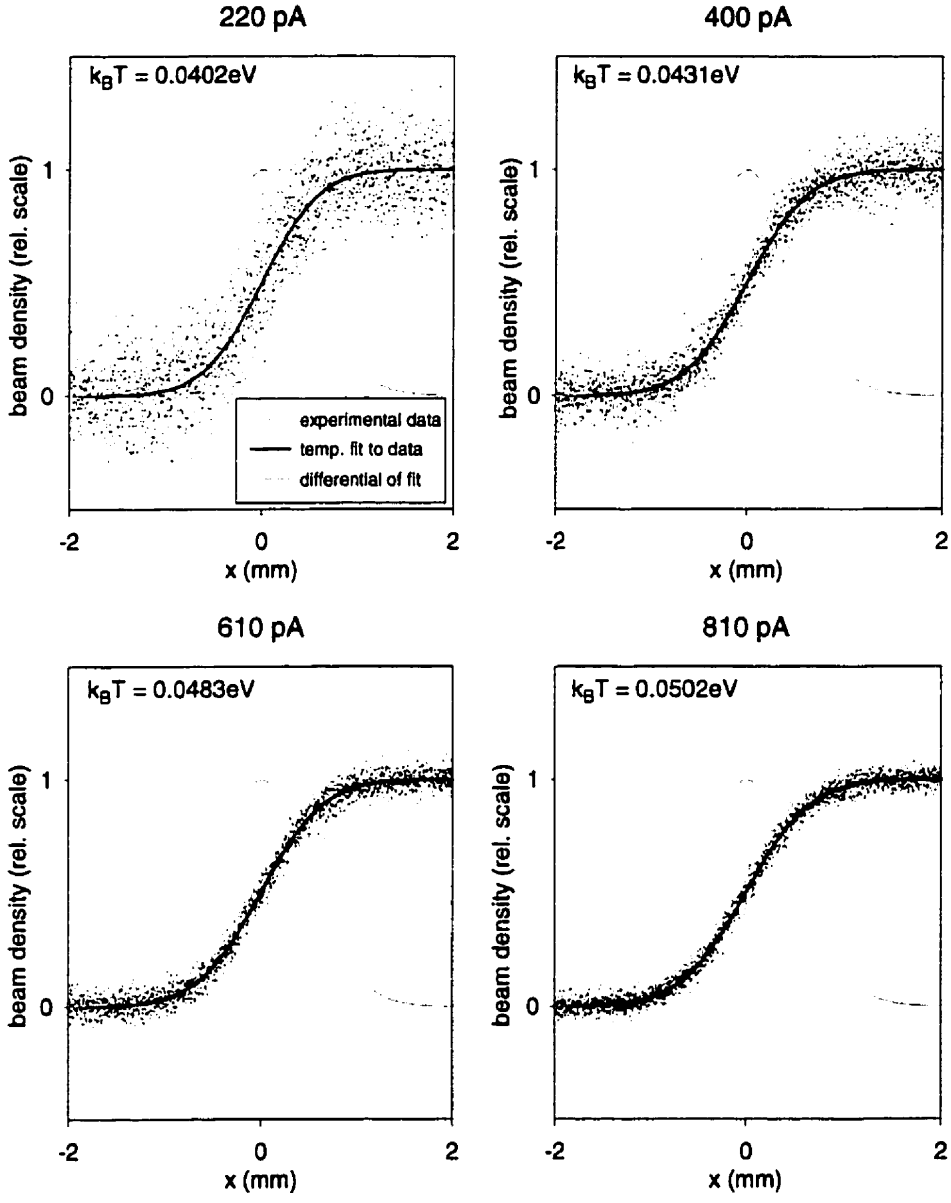

Figure 6.10: Typical experimental data at the detector and their corresponding temperature fit for cesium ions at 700 kHz, 300V rf amplitude, 25 V extraction potential and 8 Pa nitrogen pressure.

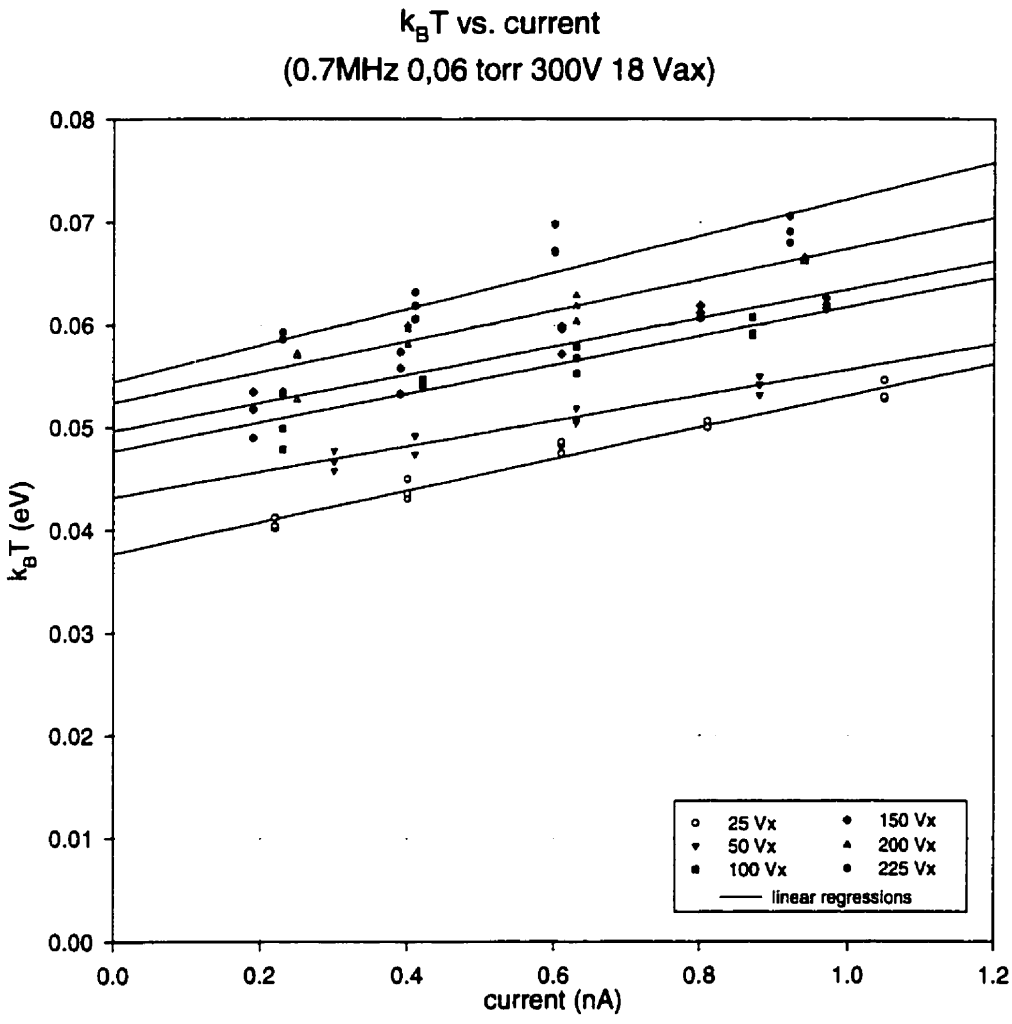

Figure 6.11: kT as a function of I for various extraction potential. The functions were assumed to be linear and were extrapolated to zero current.

increase with the extraction potential, with similar slopes. By comparing the results of the simulation for the detector values and the miniature guide values, this result again suggests that RFQ_EXT underestimates the temperature by about 10%. However, more important, the experimental values and the simulation values for the detector temperatures agree quite well in their slopes but the experimental values are about 20% higher than the simulation values.

6.2.3 Rescaling the temperature

It is concluded from the above that RFQ_EXT underestimates the temperature by about 10%. This is not surprising considering that it is only a linear optics approximation to a process that would be expected to have higher-order aberrations, particularly in the region near the exit of the miniature ion guide. To correct for this error, the temperatures determined using RFQ_EXT were rescaled upward by 10%. At the same time, the temperature rise due to the extraction field was removed, since, whatever its source, it was not in the ion beam when it exited the miniature guide. The corrected temperatures after rescaling are shown in Figure 6.13.

These rescaled temperatures are now independent of the extraction potential. For the cesium ion beam in the beam guide with operating conditions: 700 kHz, 300 V and 8 Pa buffer gas pressure, the temperature of the experimental distribution is 0.0423 ± 0.0026 eV and that of the MC simulation is 0.0372 ± 0.0009 eV. The MC simulation and the experimental results therefore agree to within 14 % and from that result it can be deduced that the agreement on the beam diameter is about 7 %. The experimental and MC simulation beam widths (1σ) are shown in Figure 6.14.

Considering the approximations involved in both the extraction of the temperature from the experimental results and the approximations involved in the Monte-Carlo simulation, this agreement is regarded as quite good.

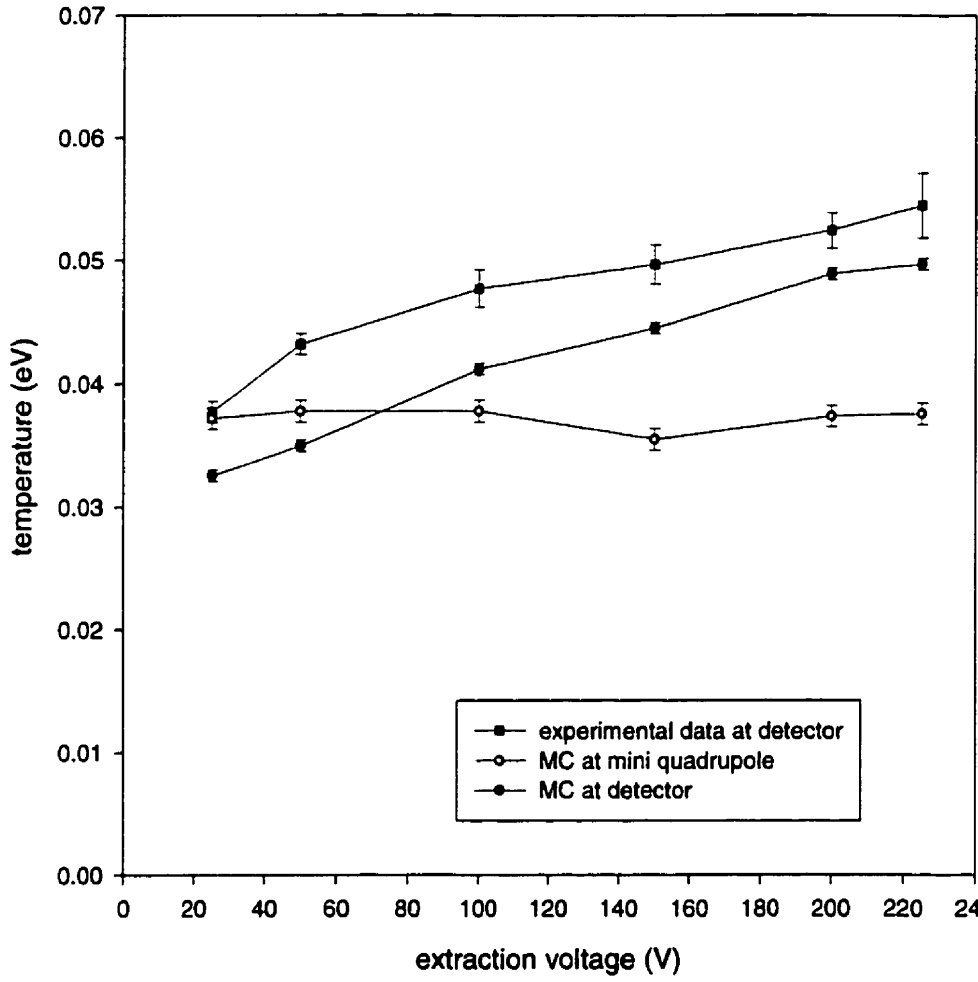

Figure 6.12: Comparison of the temperatures from the experiment and from the MC simulation.

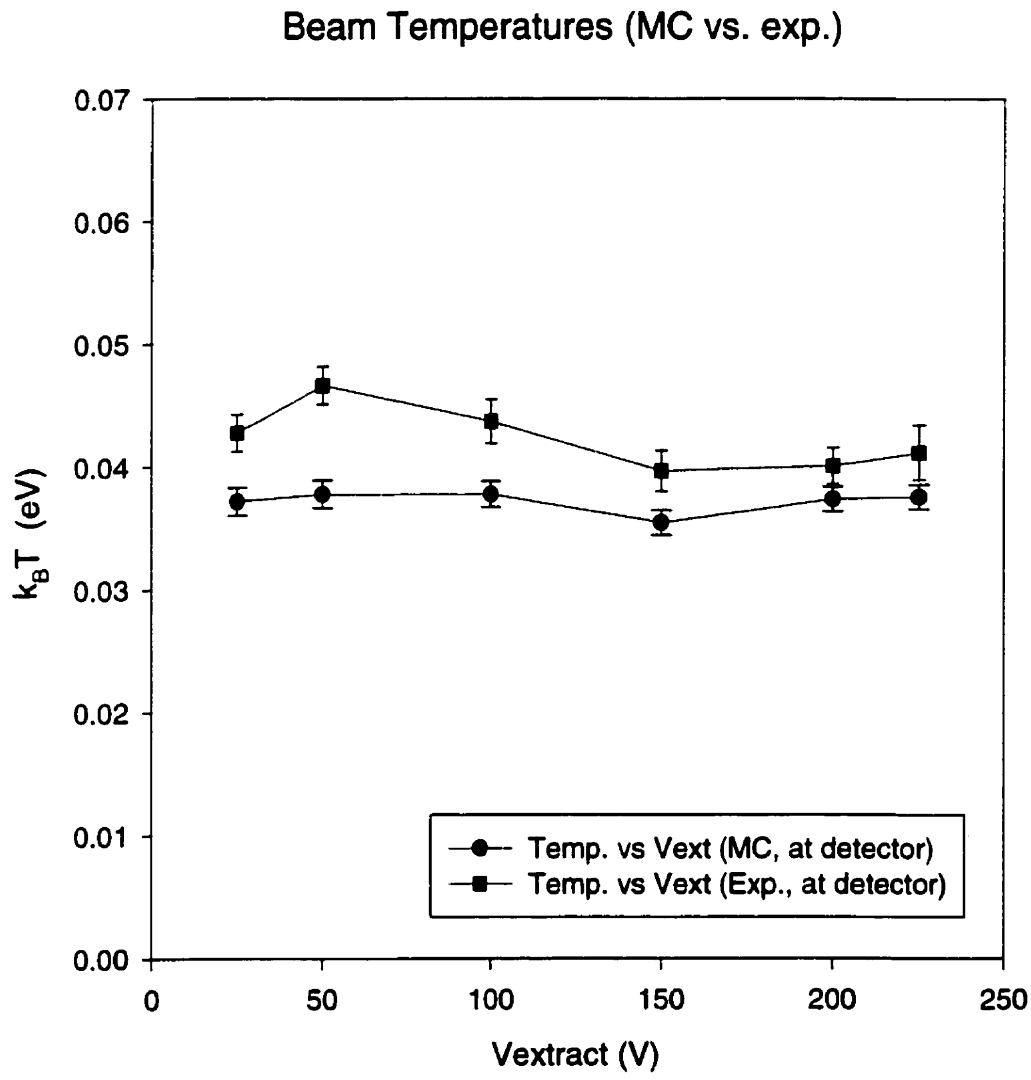

Figure 6.13: The corrected temperature from the MC simulation and the experiment.

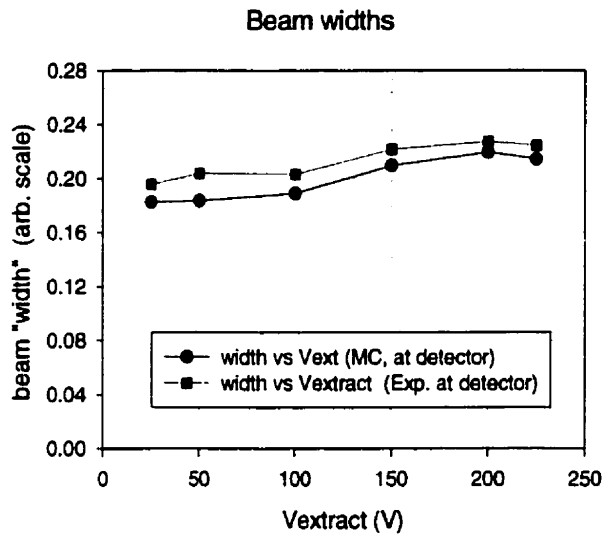

Figure 6.14: The beam size of experimental and MC simulation data.

6.2.4 Dependence of the temperature on the current

The rise of the experimental temperatures with the beam current can be explained as a space charge effect. The space charge field expands the ion beam. This results in the ions experiencing on the average, higher rf fields and thus more rf heating.

The experimentally determined temperature for the zero current was 0.0423±0.0026 eV at 0.7 MHz 300V rf amplitude and the current gradient of the temperature was $+0.0153 \pm 0.0026\, eV/nA$.

6.2.5 The effect of the axial field

In the Monte Carlo simulation, two different axial fields, one in the main quadrupole and one in the miniature quadrupole, were implemented. Figure 6.15 shows the temperature dependence on the axial field. The effect of the axial fields can be seen

by the difference in temperature between the main and in the miniature quadrupoles. There is a 15 % difference between the temperatures in main (1 V/cm) and those in the miniature quadrupole (estimated to be 0.3 V/cm from the transmission time measurements). As pointed out above, the greater axial field increases the axial kinetic energy and this increased axial kinetic energy is converted into transverse energy by collisions.

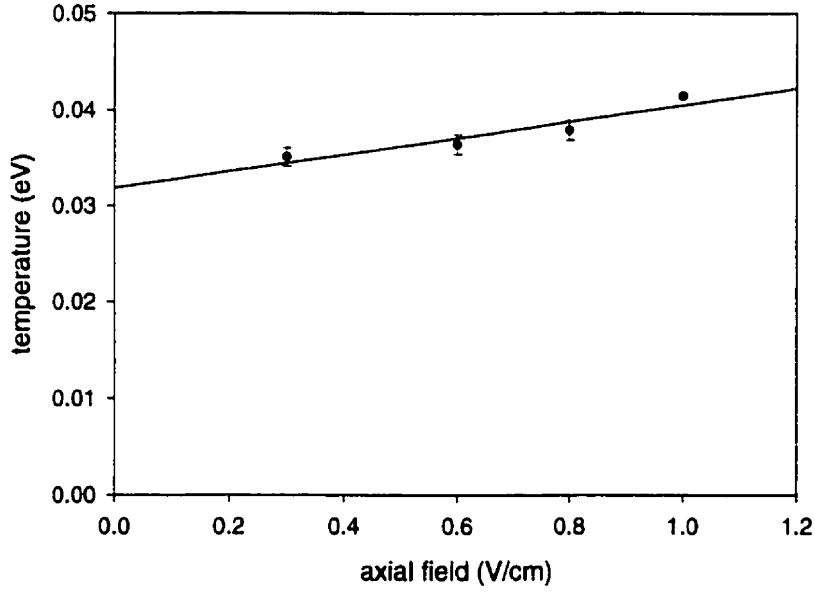

Figure 6.15: The beam temperature dependence on the axial field. The result of the MC simulation for the AXF_RFQ operating at .7 MHz, q=0.47 and 8 Pa nitrogen buffer gas pressure.

6.2.6 q value dependence of the temperature

The q value dependence of the temperature was studied using the Monte Carlo simulation as well as experimental results, with q values ranging from 0.098 to 0.81. The simulation results are shown in Figure 6.16. They show that overall, the temperature increases with q value.

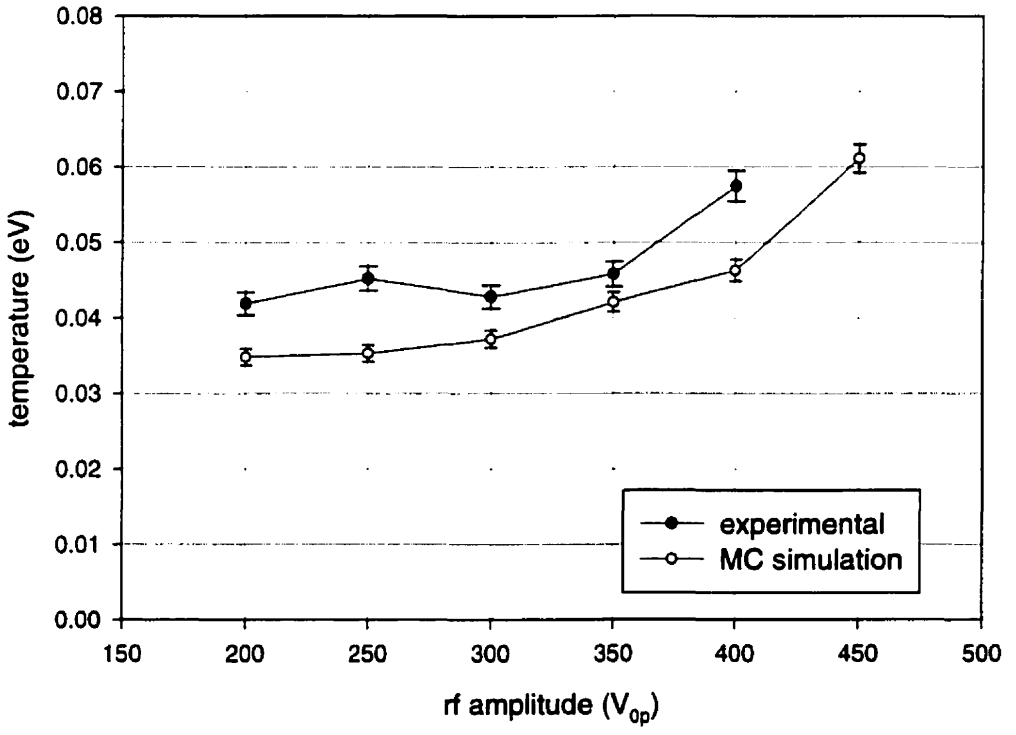

Figure 6.16: The rf amplitude (q value) dependence of temperature.

At high q values, the rf motion is more energetic and therefore causes more rf

heating. The rms velocity dependence on the q value in Chapter 3 (Figure 2.) has the same trend and supports this explanation.

6.2.7 Discussion of the temperature measurements

The temperatures for the simulated and the experimental data agree generally to within 14 % of each other or better (in some cases the agreement is to within 5%). As pointed out above, considering the approximations involved in both the experimental analysis and the Monte-Carlo simulation, this agreement is regarded as quite good. In fact, the disagreement is of about the same order as the disagreement with known ion mobility values that were used as a test of the Monte-Carlo simulation and reported in Chapter 5. This would indicate that the full disagreement could be attributed to the approximations used in the Monte-Carlo simulations.

As stated earlier, the measurements reported here are the first for the temperature of ions in an rf quadrupole ion guide. Consequently, there are no other measurements with which they can be compared. However, they can be compared with temperature measurements of ion collections in Paul traps. A good summary of such measurements can be found in ref. [Lun92].

The average kinetic energy of ions in a Paul trap was first measured without applied cooling. The main equilibrium mechanism is then evaporative cooling and an empirical relation between the trap's pseudo-potential well depth $\overline{D}$ and the temperature or kinetic energy of the ion cloud was established [Sch81]:

$$\langle E_{kin} \rangle = (0.11 \pm 0.01) e\overline{D}. \tag{6.1}$$

This empirical relation is meaningful because the evaporative cooling is closely related to the trap potential. The relationship between average kinetic energy and the pseudo-potential well depth of the trap was used in the reporting of an average kinetic energy

measurement of the cooled ion cloud [Sch81]:

$$\langle E_{kin} \rangle = \frac{e\overline{D}}{30}. \tag{6.2}$$

Relating an intensive quantity (a temperature or an average of kinetic energy) to an extensive quantity (trapping potential) is meaningless itself but the relation can be reproducible for a specific system and in most cases the trap sizes are similar and similar relations were reported [Zha95].

The measurements of ion temperatures in a Paul trap that are most appropriate to the work of this thesis are those of Lunney [Lun92], who used a time-of-flight technique to deduce the ion temperature within the trap, defining temperature in the same fashion as in the present work, he achieved temperatures for low trap loadings which were very similar to those obtained here (i.e. about twice buffer gas temperature). However, the sensitivity of his method was not as great as in the present work and the results have a higher reported error.

The phase-sensitive Laser-Induced Fluorescence (LIF) method can give more accurate temperatures than the Time-Of-Flight (T-O-F) method, because the spectrum line width can be measured accurately. Zhao used this method to measure the temperature of hafnium ions in a Paul trap in hydrogen buffer gas at room temperature and reported a value of $kT = 0.038\ eV$ at operating conditions of 400 kHz and $a_z = 0$, $q_z = 0.374$, and of 400 kHz and $a_z = 0.048$, $q_z = 0.374$ [Zha95]. He assumed that at the zero rf phase, the motion is pure thermal motion. Therefore his temperature definition is slightly different from the one in this thesis (See Figure 3.8).

6.3 Transmission

Transmission experiments were carried out with two types of main quadrupole exits: one a skimmer type lens and the other the miniature quadrupole which was central

Axial Field	0V/cm	0.5V/cm	1.0V/cm
Heater	112.1	121.6	131
Lens1	-87.9	-78.4	-69
Lens2	48.9	58.4	67.8
RFQ Front	30	39.5	48.9
RFQ End	30	30	30
Skimmer	5	5	5

Table 6.2: The bias potentials used in the transmission measurement experiment with the skimmer type exit

to the work described above. The skimmer type lens has less gas flow conductivity than the miniature quadrupole beam guide, and with this lens the experiment can be performed at up to 130 Pa with the vacuum system used in this study. On the other hand the miniature quadrupole ion beam guide interface has a higher transmission and was used in the experiment at an optimal buffer gas pressure, for different rf potentials and injection energies.

The transmission was measured with the skimmer type exit at pressures ranging from 3 Pa to 130 Pa. The skimmer type exit was adapted for the measurement of transmission at high buffer gas pressures, because it has a smaller exit fringing field region and thus has a higher transmission than the conventional diaphragm type lens exits.

The exit with the skimmer type lens is shown in Figure 6.17. The entrance lens diameter was 1mm and the exit skimmer type lens opening was 1.4 mm and the inside angle of the skimmer was 45 degrees. The bias potentials used in this experiment are shown in Table 6.2. The rf frequency was chosen to be relatively low (i.e. 250 kHz) to obtain sufficiently high q values without experiencing an electric breakdown. The

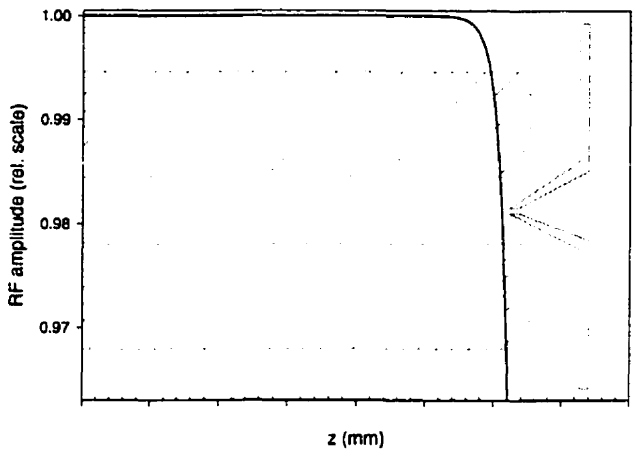

Figure 6.17: The skimmer type lens and the rf field attenuation near the lens.

ion injection energy to the buffer gas filled cell was 63 eV. The injected ion current decreased when the injection energy decreased and this injection energy was chosen so as to obtain a sufficient current with a high signal to noise ratio. The incoming ion current was determined by measuring the current in all of the conducting parts of the system exposed to the ions: the cylinder, the end plate, and the miniature quadrupole. The transmitted ion current was detected by a Faraday cup placed after the skimmer type exit lens.

6.3.1 Pressure dependence of the transmission

The transmissions for this system, for Cs^+ ions in the nitrogen buffer gas, are shown in Figure 6.18. This figure shows the transmission of the ions through the system, exiting through a hole of the skimmer type exit lens, as a function of the rf amplitude applied

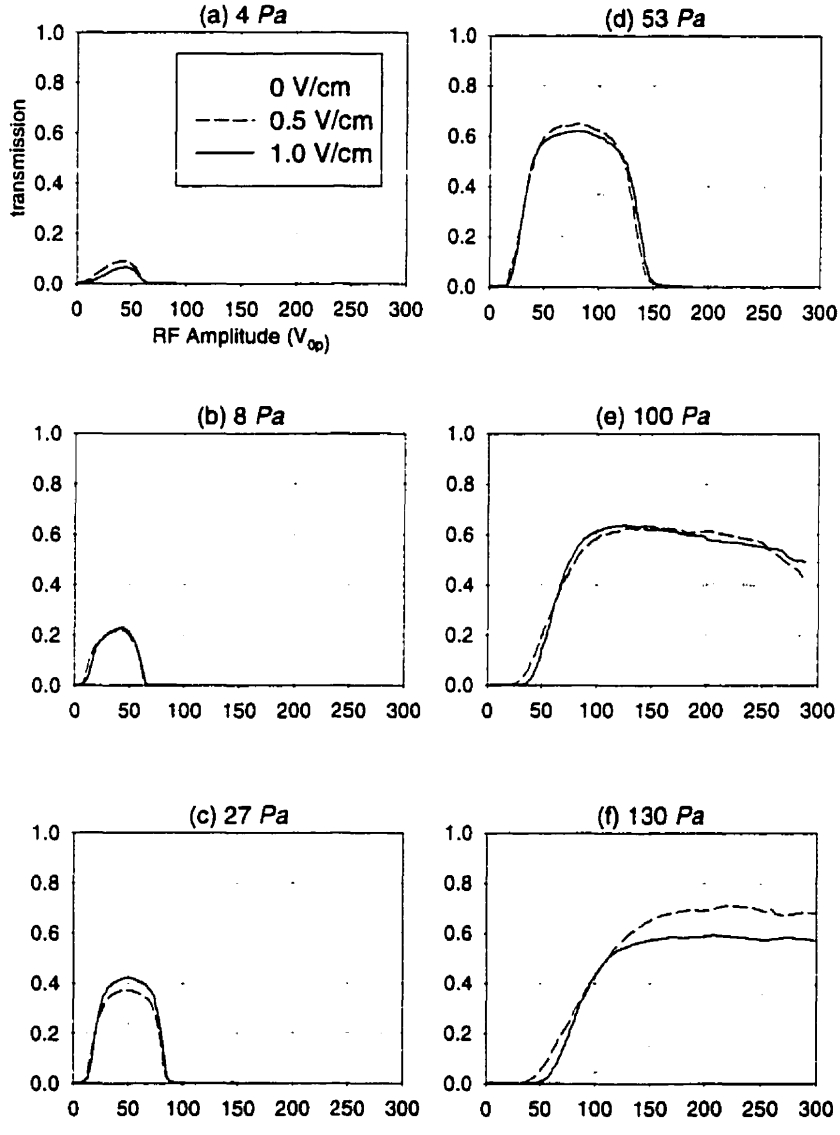

Figure 6.18: The experimental ion transmission for different nitrogen buffer gas pressures with $f = 250\ kHz$.

to the rod structure, for various pressures of the buffer gas. All the transmissions have been normalized to the incoming current: 300-400 pA.

6.3.2 q value dependence of the transmission

It is seen that, for all pressures, the transmission first increases to a maximum value as the rf amplitude increases, and then falls as the rf amplitude is further increased. This increase can be easily understood as due to the increased effectiveness of the rf quadrupole field in confining the ions when its strength is increased to a certain value. Beyond a certain field strength, the ion motion in the rf quadrupole field becomes unstable and the transmission falls.

The transmission dependence on the rf voltage can also be understood by considering the acceptance of the beam guide. These acceptance ellipses were calculated by the following method.

1. An ellipse representing the simple harmonic motion in phase space was obtained using a well depth of arbitrary maximum amplitude.

2. The rf distorted ellipse for the 90° rf phase was obtained by using the transformation matrix M(SHM $\rightarrow$ 90° rf) as explained in Chapter 3.

3. The other ellipses for the different rf phases were obtained by applying the transformation matrix M(rf phase 1 $\rightarrow$ phase 2).

4. The maximum axial magnitude should be smaller than the trap's dimension r_0. The rf phase which has the largest spatial spread was rescaled so that its spatial spread was equal to the trap dimension.

5. The ellipses for the different rf phases were then rescaled accordingly.

q	0.1	0.2	0.3	0.4	0.5	0.6	0.7	0.8
ε	9.231	16.654	22.427	26.526	28.953	29.490	27.696	22.388
$\overline{D}$	0.793	3.173	7.138	12.690	19.828	28.553	38.864	50.761
β	0.0709	0.1425	0.2161	0.2926	0.3737	0.4622	0.5630	0.6885

Table 6.3: The trap parameters sa a function of q

The related parameters were tabulated in Table 6.3

The calculated ellipses are shown Figure 6.19.

A similar calculation was reported by Todd [Tod80], but in that report the well model was misunderstood (See Chapter 2). Therefore, the acceptance ellipses for the well model were wrong. The same misunderstanding was propagated in publications on phase space dynamics up to a recent publication [Mar89].

The acceptance as a function of q is shown in Figure 6.20. The acceptance increases as q increases and reaches a maximum at $q = 0.6$ after which it decreases. For the buffer gas cooling beam guide, there is a threshold rf potential (i.e. a threshold q value) at which the confining force is sufficient to overcome the defocusing effect by diffusion and space charge effect.

However it is easily seen that, as the pressure of the nitrogen is raised, the overall effectiveness of the collisional focusing increases up to a pressure of 130 Pa. Furthermore the rf amplitude at which the maximum transmission is reached is also raised. This corresponds to the well known expansion of the stability region discussed in Chapter 3.

6.3.3 The axial field effect on the ion transmission

The transmission is higher with the axial field than without it, especially for low q values and high buffer gas pressures. This can be understood as follows. At high

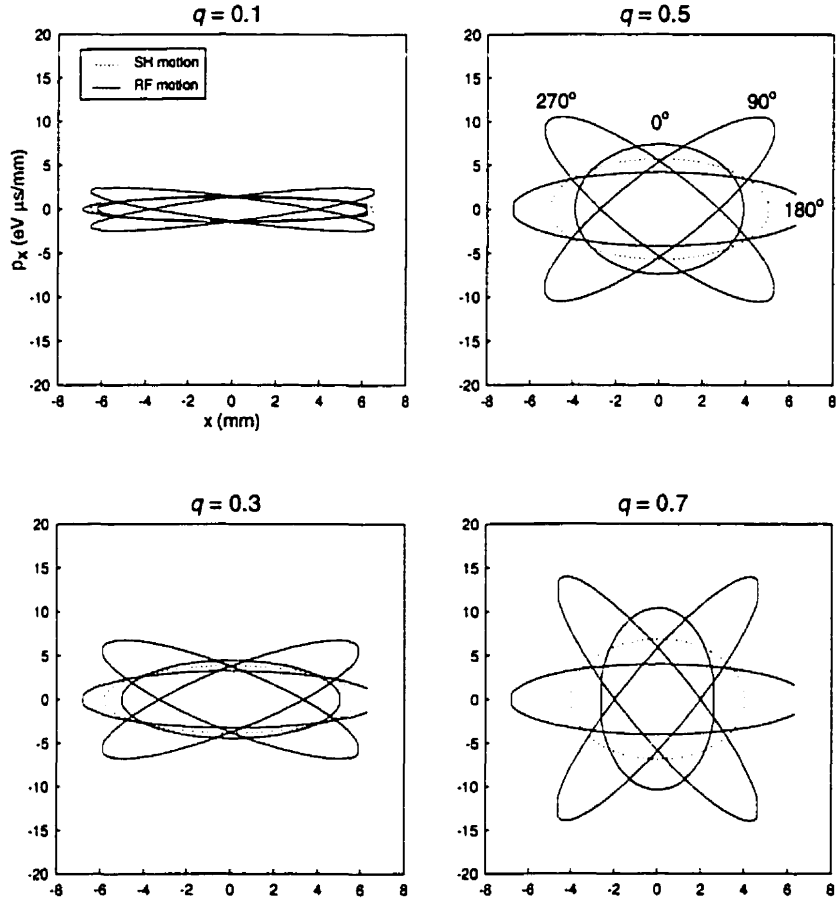

Figure 6.19: The acceptance ellipse of the AXF_RFQ for various values of q. The area is proportional to the acceptance.

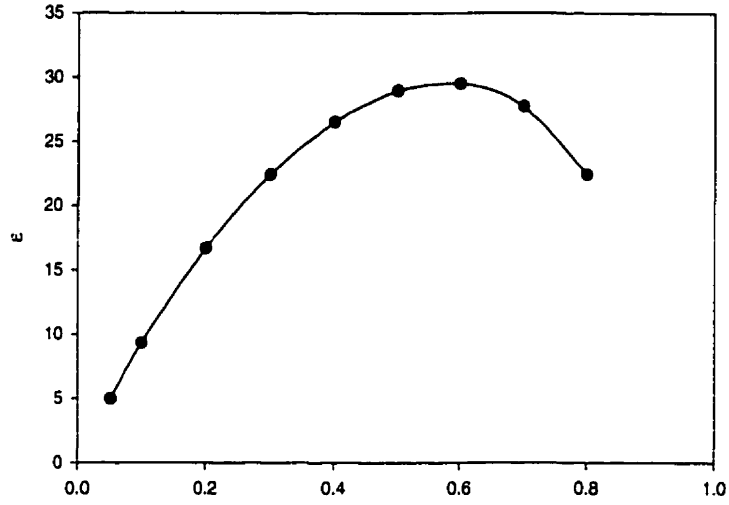

Figure 6.20: Acceptance as a function of q.

buffer gas pressures, the ions experience a focusing effect due to the rf field and a defocusing effect caused by the diffusion and space charge effects. At lower q values the confining effect is weaker due to the shallowness of the pseudo-potential well. Also the diffusion and space charge effects become more important at higher buffer gas pressures because the ion's axial velocity is low and thus the linear density is high. The thermal equilibrium is reached earlier, but the beam stretches wider in the radial direction and reaches the rod structure, thus experiencing evaporative cooling. The axial field reduces the space charge and diffusion effects by accelerating the ions along the quadrupole axis and this reduces the drift time of the beam in the quadrupole guide so that the ions experience less evaporative cooling, therefore resulting in an increase in transmission.

The transmission grows as the pressure increases, to up to 40 % (without axial field) and stays at that value until about 130 Pa. The transmission with the axial

field was more than 50 % higher than that without the axial field.

6.3.4 Optimal pressure by mobility calculation

The damping time constant calculation using mobility shows that the collisional effect is sufficient to confine ions to the size of the exit hole at a buffer gas pressure of above 3 Pa (see Fig. 6.1). However, space charge effects make the drift time even shorter and we need a higher pressure than what the calculations predict to get a sufficient collisional focusing effect. The stochastic properties of the collisions also cause a need for higher pressures than we predicted by the mobility calculation because some ions experience fewer collisions than the average. The transmission results of Figure 6.18 for 4 Pa also show that the transmission without the axial field is higher than that with the axial field. This can be interpreted as an indication that the cooling time is insufficient when the axial field is on at 4 Pa. By comparing Figure 6.18 (a) and (b), it can be deduced that the sufficient buffer gas pressure needed to cool the ions with an axial field (0.5 V/cm to 1 V/cm), is between 4 Pa and 8 Pa for a $300 - 400$ pA ion beam. When the ion current is high, the space charge pushes the ions in the radial direction and along the quadrupole axis and thus shortens the drift time. Considering the space charge effect, the pressure needed for sufficient cooling should be a bit higher than the one found by using the mobility calculation.

6.3.5 The stable q value expansion

The experimental stable q value expansion as a function of the buffer gas pressure is shown in Figure 6.21 with that of the MC simulation. The MC simulation result agrees well with the experimental result. This agreement also suggests that the Monte Carlo simulation is accurate.

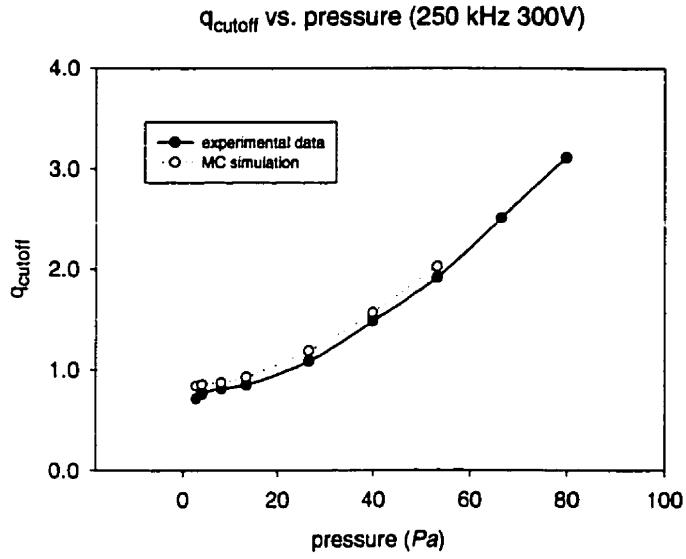

Figure 6.21: The stable maximum q value as function of pressure.

6.3.6 Dependence of transmission on the injection energy (with miniature quadrupole exit)

The injection energy of the ions into the collisional cell was changed by varying the heater and lens potentials. The bias potentials used in this experiment are shown in Table 6.4. The miniature quadrupole beam guide was described in Chapter 4. The quadrupole was operated at 0.7 MHz rf frequency within 8 Pa the nitrogen buffer gas and the incoming current was 1.4 nA.

The injection energy dependence of the transmission is shown Figure 6.22. The transmission increases for low injection energy except 30 eV injection energy. When the ions experience their first collisions, they lose most of their energy to the buffer gas and part of their axial energy is transferred to the radial component of their kinetic energy. If the radial kinetic energy is large, then the ions can scatter to beyond

Axial Field	1.7 V/cm
Heater	$53 + V_{inj}$
Lens1	$(53 + V_{inj}) - 200$
Lens2	53
RFQ Front	35
RFQ End	5
Miniature quadrupole	5

Table 6.4: The bias potentials used in the transmission measurement experiment with the miniature quadrupole exit

the acceptance region in phase space and will then hit an electrode or escape the quadrupole field. Therefore, lower injection energies can cause higher transmission than that for higher injection energies. In the experiment, the fringing field effect also increases the transverse component displacement and consequently reduces the transmission. The low transmission with 30 eV injection energy can be explained by that at low injection energy, the ions experience longer fringing field effect and the ions' initial phase space configuration may be unfavorable for the transmission.

At specific rf phases, the kinetic energy of a stable ion can be much higher than the pseudo-potential and therefore the ions with a radial component of their kinetic energy that is greater than the pseudo-potential need not be unstable.

6.4 Kinetic energy of the exiting ions

An attempt was made to observe the kinetic energy spread of the ions exiting the miniature quadrupole by using a retarding potential energy analyzer. This energy analyzer consisted of a Faraday plate and retarding potential bias generator. The detected current was measured while the retarding potential was being increased and

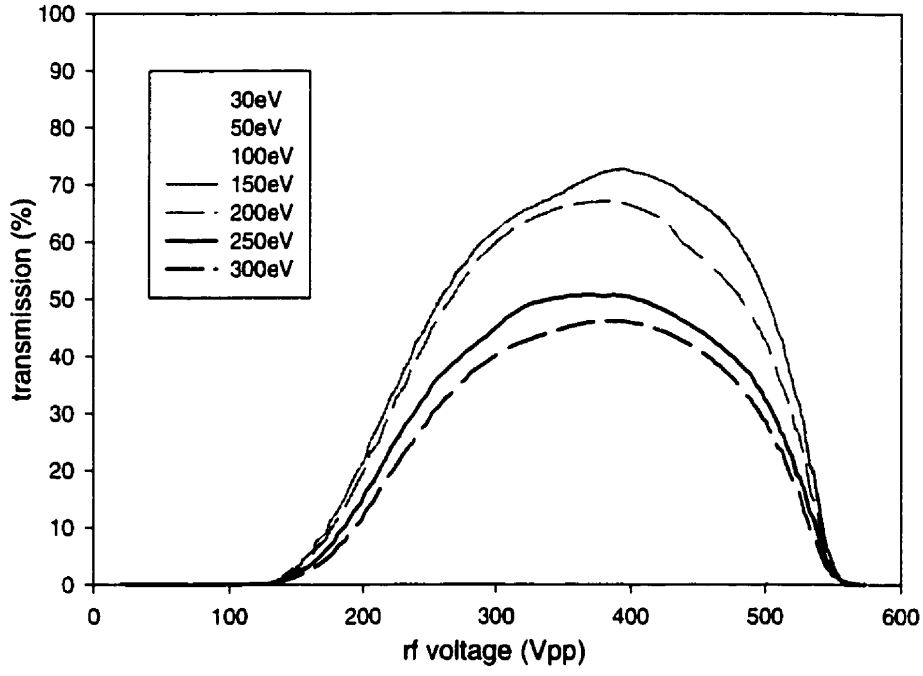

Figure 6.22: The transmission as a function of the rf amplitude for various injection energies ($f = 0.7\ MHz$, 8 Pa nitrogen buffer gas).

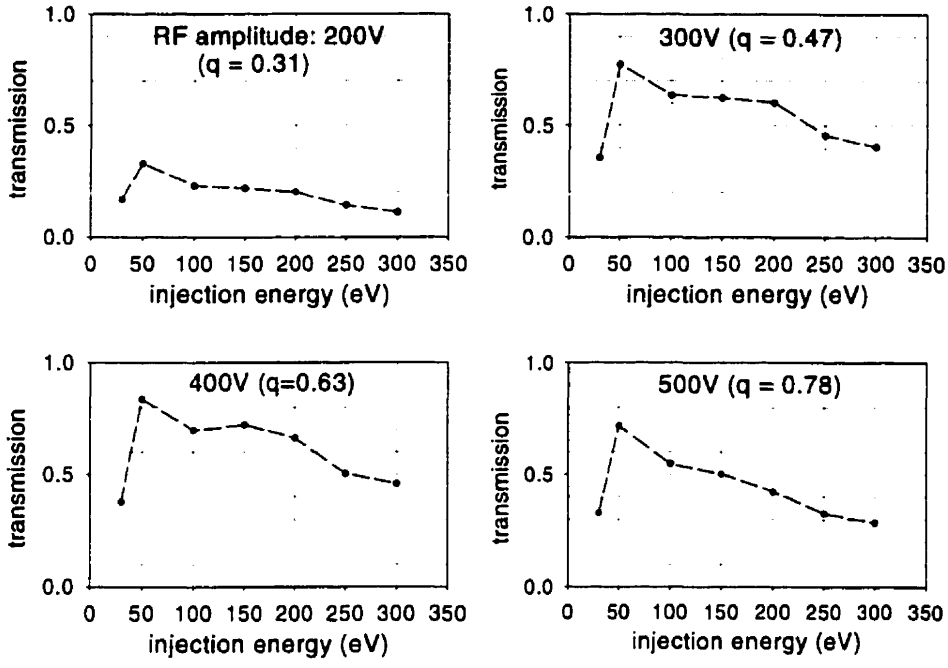

Figure 6.23: Transmission as a function of the injection energy for various q values.

the current as a function of the retarding potential was obtained (See Figure 6.24). The observed energy spread was $0.14 - 0.16\ eV$ (FWHM) and the mean energy was $0.11\ eV$.

These energies are much greater than that which can be deduced from the temperature measurements. This indicates that what was observed was the energy resolution of the analyzer and this experiment only proved that the kinetic energy spread of the ions leaving the miniature ion guide was less than $0.1\ eV$.

This is reasonable since the an energy resolution of $0.1\ eV$ is, in fact, very good for the geometry that had to be employed here.

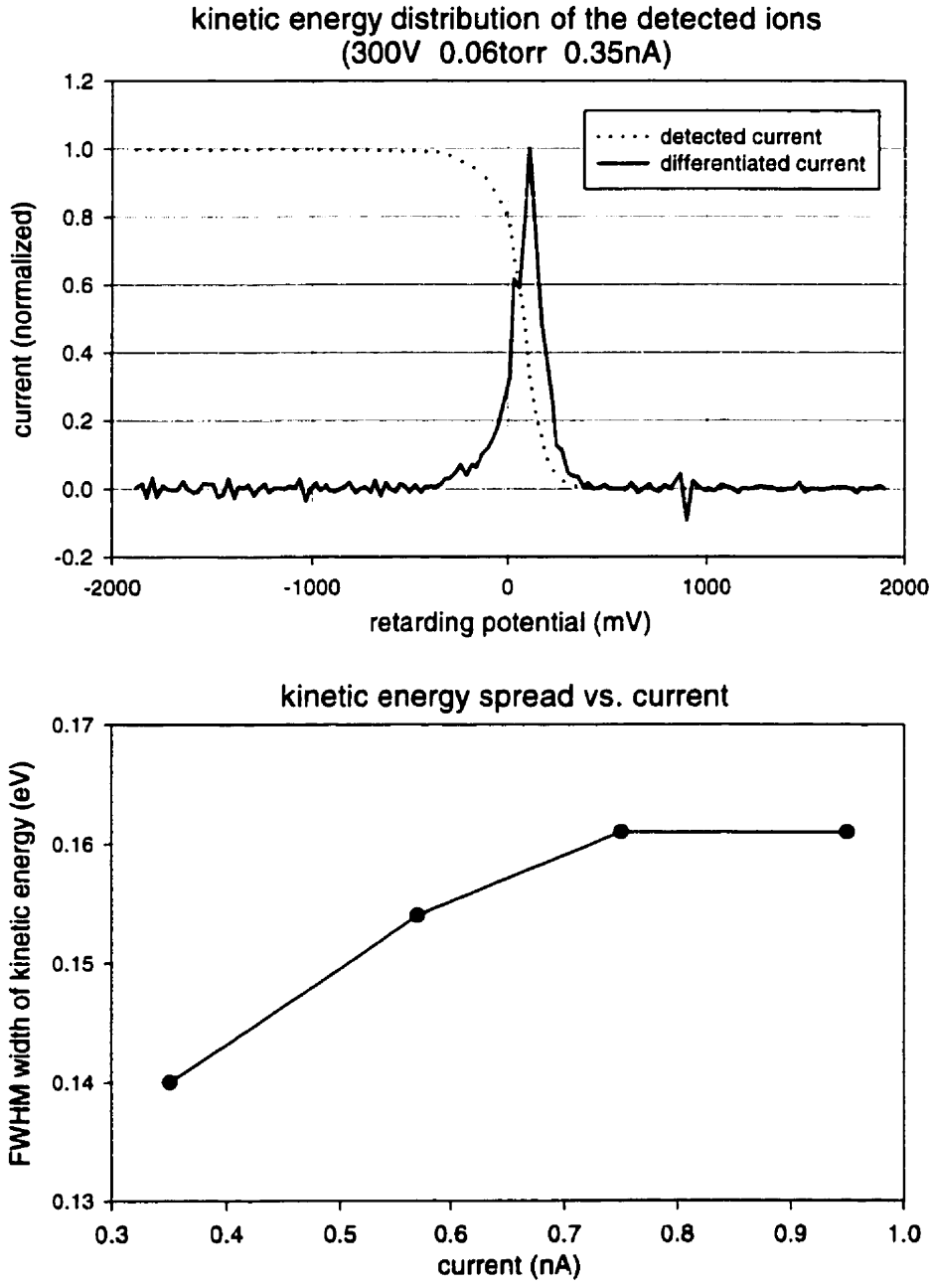

Figure 6.24: The Ion current vs retarding potential and the the energy spread (FWHM).

6.5 Drift time (cooling time)

It is important to know the cooling time in order to apply the buffer gas cooling techniques to any short lived ion, such as a that of a radionuclide or one that is very reactive to the background buffer gas. It has already been observed that in API/MS systems, the bio-molecular ion delivery time to the mass analyzer with the buffer gas cooling quadrupole beam guide is longer than the time without the buffer gas cooling system. However, the significance of this delay has not yet been established.

The axial field is the most important factor contributing to the drift time and the cooling time was measured for various axial fields at optimal pressure. To measure the cooling time, the entrance lens was pulsed and worked as an ion gate. When the pulse potential is high the ions cannot enter the collisional cell, but when the potential is low they can. In the experiment, the injection energy and axial field strength were varied. The current collected on the detector was amplified by an amplifier (KEITHLEY 428 current amplifier) and the random noise was suppressed by averaging the signals over many scans with a digital scope (LeCroy 9310M). The rise time of the current amplifier was set to 3 μs. The injection energy was 50 eV and the front bias difference(V_{L2} - V_{front}^{rfq}) was of 9 V. The experiment was carried out with the miniature quadrupole at the exit.

Figure 6.25 shows the drift times for the different axial fields and various transmitted currents. The drift times for the 1 V/cm and 0.5 V/cm axial fields were .8 ms and 1.2 ms respectively, and without the axial field, this time was about 5 ms and was shortened by an increase in current. The results for the different axial fields agree well with the mobility predictions.

When there is no axial field, the ions reach the exit by the space charge effect and the drift time becomes five to six times longer than that with the axial field. Overall, the drift time gets shorter with higher current, but this trend is suppressed when the

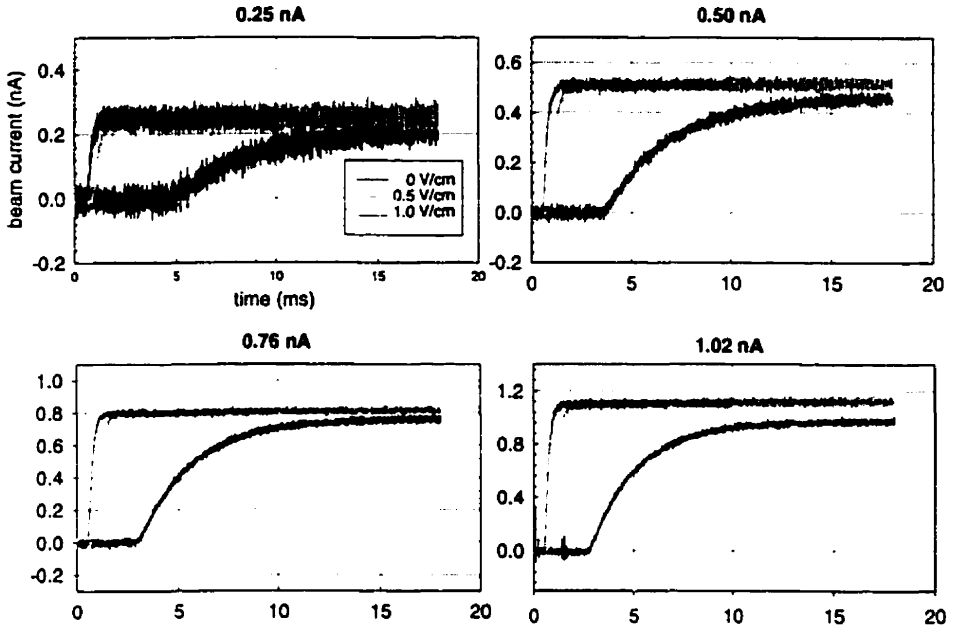

Figure 6.25: The drift time (cooling time) of the ions in the AXF_RFQ for various currents and axial fields.

axial field is on. The drift time for the 1 V/cm axial field is 6 times shorter than the one with no axial field in the range of currents studied in this experiment (0.25-1.02 nA). The drift time with no axial field depends a lot on the current and it will be significantly longer for low currents, because the drift time includes the time taken to build up the ion distribution inside the quadrupole field and to make a field gradient by space charge effect. The drift time for the 1 V/cm field was not exactly half of that for the 0.5 V/cm axial field because the miniature quadrupole has no axial field and the ions were moved through it slowly by space charge and diffusion effects. From the drift times for the 1 V/cm and 0.5 V/cm fields, the drift time in the miniature

quadrupole can be determined and it is about 30 % of the drift time in the main quadrupole (AXF_RFQ) for the 1.0 V/cm field. Considering that the effective length (pressure $\times$ length) of the miniature quadrupole is about 1/10th of that of the main quadrupole, the effective axial field caused by the space charge and diffusion effect is order of 0.3 V/cm, This is how the field required for the MC simulation of the motion in the miniature quadrupole were obtained.

Drift time in simulation

The drift time can be deduced from the Monte Carlo simulation by taking a histogram of the arrival time of the ions at the detector. There is no axial field in the miniature quadrupole and the space charge and diffusion effects play a dominant role in the axial movement of the ions. As mentioned above, the space charge and diffusion effects were simulated by using an artificial axial electric field of 0.3 V/cm, which is about 30 % of the axial electric field in the main quadrupole.

The drift times found with the simulation are shown in Figure 6.26 with the experimental results. The agreement of the experimental results with the simulation shows that the axial field implemented in the miniature quadrupole is appropriate.

6.6 The emittance of the exiting ion beam

To interface the cooled ion beam to other instruments, the emittance is an important factor to consider for the overall transmission or sensitivity of the system. Here, the emittance discussed is the normalized emittance, which is the area of the ion collection in a transverse action diagram. The ordinary emittance, usually expressed in units of length and angle (for example, $mm - mrad$) can then be calculated for any given extracted beam energy by dividing this normalized emittance by the central beam momentum.

The emittance of the beam in thermal equilibrium can be expressed in terms of

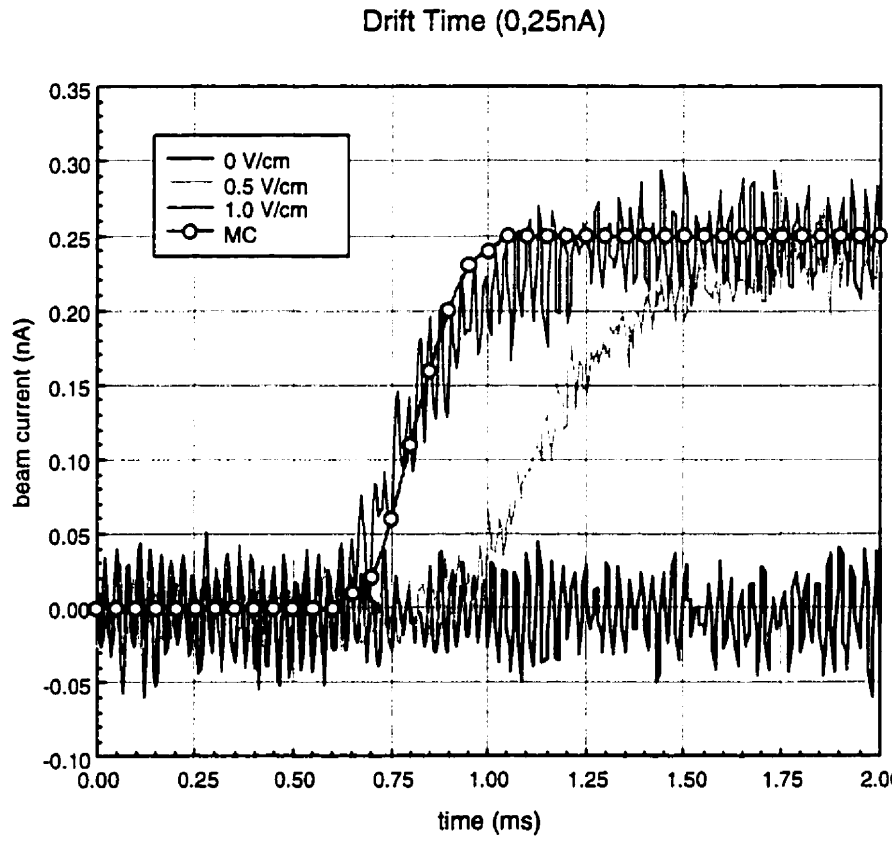

Figure 6.26: Drift time found using the MC simulation is compared with the experimental data.

its temperature. In thermal equilibrium, the ion distribution is, in principle, infinite. If we consider the practical emittance to be the phase space volume that includes 3 sigmas, then the emittance is the phase space volume corresponding to 99 % of ions. The phase space emittance ellipse for the ions in the trap is the same as that of simple harmonic motion and therefore the emittance is

$$\epsilon_i = \pi(3\sigma_i \cdot 3\sigma_{p_i}) \ \ (i = x, y)\,, \tag{6.3}$$

and using the relationship between the width (sigmas) and the temperature for harmonic potential in Chapter 2,

$$\begin{aligned} \epsilon_i &= \pi \cdot 3\sigma_i \cdot 3\sigma_{p_i} = 9\pi \cdot \frac{1}{\omega_i}\sqrt{\frac{kT}{m}}\sqrt{mkT} = 9\pi \cdot \frac{kT}{\omega} \\ &= \frac{18\sqrt{2}\pi kT}{q\Omega}\,. \end{aligned} \tag{6.4}$$

For a measured temperature $kT = 0.04\ eV$ and for the operating conditions $\Omega/2\pi = (0.7)\ MHz$ and $q = 0.47$, the transverse emittance is $0.5\pi - eV - \mu s$. For a $50\,keV$ beam of cesium ions, this corresponds to a beam emittance of about $1.4\ \pi\text{-}mm-mrad$, which is about a factor of 20 improvement over a typical ion beam at this energy.

Chapter 7

Conclusion

This thesis presented a study of the cooling process and of the thermal equilibrium state of the ion beams in a buffer gas cooling axial field quadrupole beam guide.

A temperature definition based on the Gibb distribution with rf distortion was established and compared to other temperature definitions. According to that temperature distribution model, in the quadrupole beam guide, the time averaged spatial distribution of the beam is not cylindrically symmetric, but rather, it has a four fold symmetry and its radial distribution is almost Gaussian. This temperature definition and its associated ion distribution was used to analyze the experimental data and to determine the experimental beam temperatures.

A Monte Carlo (MC) simulation was developed that used a realistic interaction potential model and the simulation results were used to study the cooling process and were compared with the experiment. This simulation is one of the most complete of its kind ever attempted up to now. It uses a realistic ion-neutral gas interaction potential model and also accounts for the thermal motion of the neutral gas. Also a MC simulation using the hard sphere collision model was compared with the simulation with the realistic potential model and the comparison shows discrepancies in the

trajectories and the cooling rates. This suggests that the hard sphere collisional model does not provide an accurate simulation of the collisional cooling processes and of the properties of the cooled beam. The experimental and simulation results were compared with each other. The results agree well in many aspects such as the stable q value expansion, the optimal pressure, the cooled beam profiles and temperature and the cooling time, confirming the validity of both the simulation and the experiment.

From the MC simulation, the cooling process of the initially energetic external ion beam was explained through three cooling stages: evaporative cooling, collisional cooling and thermal equilibrium stages. From the simulated beam evolution, we found that the ion loss was mainly due to evaporative cooling and this process comes from the transfer of the initial axial energy to the radial direction. This loss can be minimized by reducing the injection energy.

From an analytical study using the mobility calculation, a graphical method was suggested for finding a good pressure range for buffer gas cooling and we used these results in the experimental system. A beam profile measurement system was developed and was used to determine the experimental beam temperature in the quadrupole field. The measurement system consisted of the miniature quadrupole beam guide, a detector and an analysis program.

The temperature of the ion beam in the quadrupole field was determined from the experimental data and the MC simulation results. The simulated beam temperature was $0.0372 \pm 0.0009\ eV$ in ion beam guide with a q value of 0.47 and a frequency of $\Omega/2\pi = 700\,kHz$. For the same operating conditions, the measured beam temperature at the zero current limit was $0.0424 \pm 0.0026\,eV$ and the increase in temperature for an increase in the ion current was $0.0145 \pm 0.0012\ eV/nA$. The difference between the temperatures for the simulated and experimental data were in a 5 to 15 percent range. This agreement shows that the experimental results and the simulation are both good. The difference between the results can be attributed to the errors in both

the experiment and the simulation. In the simulation, some of the error was due to the error in the implemented interaction potential as can be seen from the error in the mobility calculation. The errors in electric fields (assumed axial field in the miniature quadrupole and rf fringing field) can also be the possible sources of error. In the experiment, the mechanical errors in the construction of the electrodes as well as the electronic measurements can also be possible sources of error.

The axial field quadrupole cooling system was tested for various nitrogen buffer gas pressures and rf operating conditions (frequency and amplitude). The transmission was tested for a buffer gas pressure of up to 133 Pa. The transmission was continuously increasing with increase in buffer gas pressure. The best achieved ion transmission was of 80 percent of the incoming ion beam and this occurred at the operating conditions: 700 kHz rf frequency, 300 V rf amplitude and 8 Pa buffer gas pressure. The cooling effect was observable for pressures above 3 Pa. At 8 Pa buffer gas pressure, the drift time was less than 1 ms with the $1\,V/cm$ axial field, and without the axial field, the cooling time was about 7 ms for 1.0 nA ion current and 12 ms for 0.25 nA, and it increased with decrease in the ion current. Thus the axial field was an important factor for the lowering of the drift time, especially for low currents. The kinetic energy of the exiting ion beam was measured by using a retarding potential energy analyzer. The kinetic energy spread was 0.2 eV. The results were largely influenced by the resolution of the analyzer, but even though the energy spread is much larger then the thermal energy at the measured temperature, it does not conflict with the temperature measurements because the low resolution gives an artificial large spread. The exiting cooled ion beam's emittance was calculated with the phase space distribution model at the measured temperature and it was $0.5\ \pi\ eV - \mu s$.

A further elaboration of this work might be the study of the effect of the buffer gas temperature since it is expected that the ion temperature should decrease in

proportion to the buffer gas temperature. Thus even lower beam temperatures than those achieved in this work would be possible.

Overall, the experimental and simulated results can be summarized as follows:

1. An AXF_RFQ type cooling system can cool ion beams to temperatures that are about only twice that of the buffer gas used to cool them. Furthermore, this can be accomplished with losses of less than 20 %. This shows great promise for many applications in beam technology

2. The MC program developed is a good tool to study the buffer gas cooling process and to study the cooled beam properties, as demonstrated by the agreement of its predictions with experiment.

3. The temperature measurements achieved in this thesis were some of the most accurate for this kind of experiment.

REFERENCES

Ame57 J. S. Ames and F. D. Murnaghan, *Theoretical Mechanics*, Dover, New York (1957).

Bas90 C. Basic, R. A. Yost, J. R. Eyler, Proc. 38th conf. Mass Spectrom. Allied Topics. Tucson, AZ (1990) 858.

Bec89 St. Becker, G. Bollen, F. Kern, H. J. Kluge, R. B. Moore, G. Savard, L. Schweikhard, H. Stolzenberg, and the ISOLDE Collaboration, CERN EP89-126 (1989).

Blu89 R. Blümel, C. Kappler, W. Quint, and H. Walther, "Chaos and order of laser-cooled ions in a Paul trap", Phys. Rev. A40 (1989) 808.

Blu93 J. W. Emmert, M. Moore, and R. Blümel, "Prediction of a deterministic melting transition of two-ion crystals in a Paul trap", Phys. Rev. A48 (1993) 1757.

Blu95 R. Blümel, "Cooling-induced melting of ion crystals in a Paul trap", Phys. Rev. A51 (1995) 620.

Bon74 R. F. Bonner, *A study of the quadrupole ion storage source*, Ph.D. Thesis, Univ. of Kent, Canterbury, Kent, England, 1974.

Bra95 C. C. Bradley, C. A. Sackett, J. J. Tollett, and R. G. Hulet, "Evidence of Bose-Einstein condensation in an atomic gas with attractive interactions", Phys. Rev. Lett. 75 (1995) 1687.

Bre74 Donald W. Breck, *Zeorite Molecular Sieves-Structure, Chemistry, and Use*, Wiley, NewYork (1974) Chapter 7.

Bro86 L. S. Brown, and G. Gabrielse, "Geonium theory: Physics of a single electron or ion in a Penning trap", Rev. Mod. Phys. 58 (1986) 233.

Chu69 D. A. Church and H. G. Dehmelt, "Radiative cooling of an electrodynamically contained protron gas", J. Appl. Phys, 40 (1969) 3421.

Cor89 E. A. Cornell et al., "Single-ion cyclotron resonance measurement of $M(Co^+)/M(N_2^+)$", Phys. Rev. Lett. 63 (1989) 1674.

Cou52 E. D. Courant, M. S. Livingston and H. S. Snyder, "The strong-focusing synchrontron-A new high energy accelerator", Phys. Rev., 88(1952) 1190.

Cra93 J. E. Crawford, F. Buchinger, L. Davey, Y. Ji, J. F. P. Lee, J. Pinard, J. L. Vialle and W. Z. Zhao, "Laser desorption sources and time-of-flight injection for RFQ traps", Hyperfine Interactions 81 (1993) 143.

Dav95 K. B. Davis et al., "Bose-Einstein condensation in a gas of sodium atoms", Phys. Rev. Lett. 75 (1995) 3969.

Daw76 P. H. Dawson(editor), *Quadrupole Mass Spectrometry and Its Applications*, Elsevier, Amsterdam (1976).

Daw76-1 [Daw76] p213 Fig. 8.20.

Daw77 P. H. Dawson, "The effect of collisions on ion motion in quadrupole fields", J. Mass Spectrom. Ion Phys., 24 (1977) 447.

Day54 I. E. Dayton, F. C. Shoemaker and R. F. Mozley, "The measurement of two-dimensional fields. PartII: Study of a quadrupole magnet", Rev. Sci. Instrum. 25 (1954) 485.

Deh67 H. G. Dehmelt, Advan. At. Mol. Phys., 3 (1967) 53.

Deh88 H. Dehmelt, "A single atomic particle forever floating at rest in free space: New value for electron radius", Physica Scripta T22, (1988) 102.

Den71 D. R. Denison, "Operating parameters of a quadrupole in a grounded cylindrical housing", J. Vac. Sci. Technol., 8 (1971) 266.

Die87 F. Diedrich, E. Peik, J. M. Chen, W. Quint and H. Walther, "Observation of a phase transition of stored laser-cooled ions", Phys. Rev. Lett. 59 (1987) 2931.

Dou92 D. J. Douglas and J. B. French, "Collisional focusing effects in radio frequency quadrupoles", J. Am. Soc. Mass Spectrom 3 (1992) 398.

Dyc78 R. S. Van Dyck, Jr., P.B. Schwinberg and H.G. Dehmelt, 'Electron magnetic moment from Geonium spectra', in B. Kursunoglu, A. Permutter, and L.F. Scott (eds.), *New Frontiers in High-Energy Physics*, Plenum Publishing, N.Y. pp. 159-181.

Dyc85 R. S. Jr. Van Dyck, F. L. Moore, D. L. Farnham, and P. B. Schwinberg, Int. J. Mass Spectrom. Ion Processes 66 (1985) 327.

Ell78 H. W. Ellis, E. W. McDaniel, D. L. Albritton, L. A. Viehland, S. L. Lin, and E.A. Mason, *Atomic Data and Nuclear Data Tables 22-Transport Properties of Gaseous Ions Over a Wide Energy Range. Part II*, (1978) 201.

Gil88 S. L. Gilbert, J. J. Bollinger, and D. J. Wineland, "Shell-Structure Phase of Magnetically confined Strongly Coupled Plasmas", Phys. Rev. Lett. 60, (1988) 2022.

Goe92 D. E. Goeringer, W. B. Whitten, J. M. Ramsey, S. A. McLuckey, G. L. Glish, "Theory of high-resolution mass spectrometry achieved via resonance ejection in the quadrupole ion trap", Anal. Chem., 64 (1992) 1434.

Gul86 S. L. Gulick, *Ion Injection into Radio Frequency Quadrupole Field Devices*, Master Thesis, McGill University (1986).

Hem92 P. H. Hemberger, N. S. Nogar, J. D. Williams, R. G. Cooks and J. E. P. Syka, "Laser photodissociation probe for ion tomography studies in a quadrupole ion-trap mass spectrometer", Chem. Phys. Lett. 191, (1992) 405.

Hof88 J. Hoffnagle, R.G. DeVoe, L. Reyna, and R.G. Brewer, "Order-chaos transition of two trapped ions", Phys. Rev. Lett. 61, (1988) 255.

Hua63 Kerson Huang, *Statistical Mechanics*, Wiley, New York (1963) 77.

Ive23 N. Ives, "Positive rays in alkali metal vapor thermionic tubes", Phys. Rev., 21 (1923) 385.

Jol95 Jolliffe, L. Charles, "Mass spectrometer with radial ejection", US patent 5576540, Filed Aug. 11,1995.

Jul95 R. K. Julian, M. Nappi, C. Weil, and R. G. Cooks, "Multiparticle simulation of ion motion in the ion trap mass spectrometer: Resonance and direct current pulse excitation", J. am. Soc. Mass spectrom 6 (1995) 57

Kim95 Taeman Kim, Peter Varfalvy and R. B. Moore, "Ion transmission in RFQ rods with high buffer gas pressure", 41st International Conference on Analytical Science and Spectroscopy (1995)

Kin23 K. N. Kingdon and J. Langmuir, "Thermionic phenomena due to alkili vapors. Part I. Experimental and Part II. Theoritical", Phys. Rev., 21 (1923) 380-381.

Kin24 K. N. Kingdon and J. Langmuir, Proc. Roy. Soc., 107A (1924) 61.

Klu92 H.-J. Kluge and G. Bollen, "Ion traps—recent applications and developments", Nucl. Instr. and Meth. B70 (1992) 473

Kni79 R. D. Knight and M. H. Prior, "Laser scanning measurement of the density distribution of confined $^6Li^+$ ions", J. Appl. Phys. 50, (1979) 3044.

Law76 G. Lawson, R. F. Bonner, R. E. Mather, J. F. J. Todd, R. E. March, "Quadrupole ion store (Quistor) Part 1.—Ion-molecule reactions in methane, water and ammonia", J. Chem. Soc., Fraday Trans. 72 (1976) 545.

Lic69 Allan J. Lichtenberg, *Phase-Space Dynamics of Particles*, Wiley, New York (1969)

Lon93 Frank A. Londry, Roland L. Alfred and Raymond E. Mach, "Computer simulation of single-ion trajectories in Paul-type ion traps", J. am. Soc. Mass spectrom, 4 (1993) 687

Lun91 M. D. Lunney and R. B. Moore, "The computation of electric fields for Numerical integration of charged particle motion", IEEE Transactions on Magnetics, Vol. 27, No.5 Sept, (1991) 4174.

Lun92 M. D. N. Lunney, F. Buchinger and R. B. Moore, "The temperature of buffergas cooled ions in a Paul trap", Journal of Modern Optics, 39 (1992) 349.

Lun92-1 M. D. N. Lunney, *The Phase Space Volume of Ion Clouds in Paul Traps*, PhD Thesis, McGill University (1992).

Mar89 R. E. March and R. J. Hughes, *Quadrupole Storage Mass Spectrometry*, Wiley, New York (1989).

March89-1 [Mar89] section 2.VII. and cited references related to the well model calcuration.

Mar70 J. B. Marion, *Classical Dynamics of particles and systems*, Academic Press, 1970.

Moh96 A. M. Ghalambor Dezfuli, *Injection, Cooling, and Extraction of Ions from a Very Large Paul Trap*, PhD Thesis, McGill University (1996).

Maj68 F. G. Major and H. G. Dehmelt, "Exchange-collision technique for the rf Spectroscopy of stored ions", Phys. Rev. 170 (1968) 91.

Nou90 B. D. Nourse and H. I. Kenttämaa, "Effective ion temperature in a quadrupole ion trap", J. Phys. Chem. 94 (1990) 5809.

Pau53 W. Paul and H. Steinwedel, Z. Naturforsch, A8 (1953) 448.

Pet95 P. Varfalvy, *Precision Ion Optics of Axizymmetric Electric System*, M. Sc. Thesis, McGill University (1995).

Pos53 See R. F. Post, Univ. Calif. Radiat. Lab. Rep. U.C.R.L. 2209, 1953.

Rai92 M. G. Raizen, J. M. Gilligan, J. C. Bergquist, W. M. Itano, and D. J. Wineland, "Ionic crystals in a linear Paul trap", Phys. Rev. A45 (1992) 6493.

Rou92 G. Rouleau, *A tandem Paul-Penning trap mass measurement system for radionucleides*, Ph.D. Thesis, McGill University, (1992).

Sau88 Th. Sauter, et al., "On the photo-dynamics of single ions in a trap", Z. Phys. D10 (1988) 153.

Sch81 H. Schaaf, U. Schmeling, and G. Werth, Appl. Phys. 25 (1981) 249.

Sch79 R. Schneider and G. Werth, "Ion storage technique for very long living states: The Decay Rate of the $5D_{3/2}$ State of Ba II", Z. Phys. A 293 (1979) 103.

Sch90 M. Schubert, I. Seimers, and R. Blatt, "Kineetic energy and spatial width of ion cloud in Paul traps", Appl. Phys. B51 (1990) 414.

Sie88 I. Siemers, R. Blatt, T. Sauter and W. Neuhauser, "The kinetic energy of ion clouds in Paul traps", Physica Scripta, T22 (1988) 240.

Smi10 C. Smith, *Conic Sections*, Macmillan, London (1910).

Sta84 G. C. Stafford, Jr., P. E. Kelley, J. E. P. SYKA, W. E. Reynolds, and J. F. J. Todd, "Recent improvement in and analytical applications of advanced ion trap technology", Int. J. Mass Spectrom. Ion Phys. 60 (1984) 85.

Sto90 H. Stolzenberg et al., "Accurate mass determination of short-lived isotopes by a tandem Penning-trap mass spectrometer", Phys. Rev. Lett. 65, (1990) 3104.

Tod80 J. F. J. Todd, D. A. Freer and R.M. Waldren, Int. J. Mass Spectrom. Ion Phys. 36 (1980) 185.

Tod80-1 J. F. J. Todd, R. M. Waldern and R. F. Bonner, "The quadrupole ion store (Quistor) part VIII. The theoritical estimation of ion kinetic energies: a comparative survey of the field", Int. J. Mass Spectrom. Ion Phys. 34 (1980) 17.

Tod80-2 J. F. J. Todd, R. M. Waldern, D. A. Freer and R. B. Turner, "The quadrupole ion store (Quistor) part X. Space charge and ion stability. B. On the theoretical distribution and density of stored charge in rf quadrupoles", Int. J. Mass Spectrom. Ion Phys. 35 (1980) 107.

Ved95 M. Vedel, M. Knoop, D. Lunney, I. Rebatel, and F. Vedel, "Determination of trapped-ion kinetic energy by the time-of flight method for free ejected ions", Phys. Rev. A51, (1995) 2294.

Ved83 F. Vedel, J. André, M. Vedel, and G. Brincourt, "Computed energy and spatial statistical properties of stored ions cooled by a buffer gas", Phys. Rev. A27, (1983) 2321.

Ved84 F. Vedel and J. André, "Influence of space charge on the computed statistical properties of stored ions cooled by a buffer gas in a quadrupole rf trap", Phys. Rev. A29, (1984) 2098.

Ved92 F. Vedel and M. Vedel, "Investigations on the kinetic energy of trapped ions by consideration of ion/molecule collisions", Journal of Modern Optics, 39 (1992) 431.

Val77 L. Vályi, *Atom and Ion Sources*, Wiley, Budapest (1977).

Ved83 F. Vedel, J. André, M. Vedel, and G. Brincourt, "Computed energy and spatial statistical properties of stored ions cooled by a buffer gas", Physical review A27 (1983) 2321.

Vie75 L. A. Viehland, E. A. Mason, W. F. Morrison and M. R. Flannery, *Atomic Data and Nuclear Data Tables 16-Tables of Transport Collision Integrals for (n,6,4) Ion-Neutral Potentials*, (1975) 495.

Whe74 N. Rey Whetten, "Macroscopic particle motion in quadrupole fields", J. Vac. Sci. Technol., Vol. 11, No. 2 (1974) 515

Wue59 R. F. Wuerker, H. Shelton and R. V. Langmuir, "Electrodynamic containment of charged particles", J. Appl. Phys., 30 (1959) 342.

Win87 D. J. Wineland, J. C. Bergquist, W. M. Itano, J. J. Bollinger and C.H. Manney, "Atomic-ion coulomb clusters in an ion trap", Phys. Rev. Lett. 59, (1987) 2935.

Wal94 H. Walther, Adv. At. Mol. Phys. 31, (1994) 137.

Zha95 W. Zhao, *Laser Spectroscopic Studies of Hafnium Ions Confined in a Paul Trap*, Ph.D. Thesis, McGill University (1995).